In situ Monitoring of the Synthesis and Treatment of Various Nanoparticles in a Plasma System

Dissertation
zur Erlangung des Doktorgrades
der Mathematisch-Naturwissenschaftlichen Fakultät
der Christian-Albrechts-Universität zu Kiel

vorgelegt von
Oguz Han Asnaz

Kiel, 2023

In situ Monitoring of the Synthesis and Treatment of Various Nanoparticles in a Plasma System

In-situ Kontrolle der Synthese und Behandlung verschiedener Nanopartikel in einem Plasmasystem

Prüfungsausschuss

Vorsitzender: Prof. Dr. Wolfgang J. Duschl
Institut für Theoretische Physik und Astrophysik
Christian-Albrechts-Universität zu Kiel

Gutachter: Prof. Dr. Jan Benedikt
Institut für Experimentelle und Angewandte Physik
Christian-Albrechts-Universität zu Kiel

Prof. Dr. Franz Faupel
Institut für Materialwissenschaft
Christian-Albrechts-Universität zu Kiel

Mitglied: Prof. Dr. Holger Kersten
Institut für Experimentelle und Angewandte Physik
Christian-Albrechts-Universität zu Kiel

Tag der mündlichen Prüfung:
20. November 2023

Kiel, 2023

Eidesstattliche Erklärung

Hiermit versichere ich an Eides statt, dass die vorliegende Dissertation – abgesehen von der Beratung durch meinen Betreuer und der Verwendung der angegebenen Hilfsmittel – nach Inhalt und Form meine eigene Arbeit ist. Sie hat weder ganz noch teilweise an einer anderen Stelle im Rahmen eines Prüfungsverfahrens vorgelegen. Sie ist weder veröffentlicht noch zur Veröffentlichung eingereicht worden. Die Arbeit ist unter Einhaltung der Regeln guter wissenschaftlicher Praxis der Deutschen Forschungsgemeinschaft entstanden. Mir wurde kein akademischer Grad entzogen.

Kiel, den

_____

Abstract

Nanoparticles offer a range of desirable properties compared to their bulk material counterparts. Their nanoscale dimensions result in extreme surface-to-volume ratios as well as quantum confinement effects, which make them prime targets for applications in various fields such as catalysis, biomedicine, opto-electronics, or neuromorphic computing.

This work is concerned with the synthesis and treatment of carbon and silicon nanoparticles, as well as silver-silicon core-shell nanoparticles using plasma discharges with a special focus on their in situ diagnostics. Continuous in situ monitoring via Fourier-transform infrared spectroscopy (FTIR) and localised surface plasmon resonance during the plasma treatment allows for fine-grained control of the nanoparticle properties such as size, chemical composition, or surface functionalisation, which are key for various applications. The results are confirmed by extracting particle samples for ex situ transmission electron microscopy.

As a stepping stone, carbon particles with diameters of about 500 nm are produced and confined in the Suleika Nano experiment, which is a prototypical setup in the field of dusty plasmas for the study of the interactions between dense dust clouds and a plasma. The mass change of particles noted by previous experiments is traced back via FTIR analysis to impurities of ambient air leading to the incorporation of oxygen into the particle.

After this initial experiment, the synthesis and treatment of the particles is separated into two systems, giving independent control over their conditions. For the experiments on silicon semiconductor nanoparticles, an external capacitively coupled plasma source is used to generate small particles in the range of nanometres. They are then injected into a secondary inductively coupled plasma discharge in E-mode for confinement and further hydrogen treatment. Isotopic studies via FTIR using deuterium show addition of deuterium in the bulk of the particles while existing hydrogen bonds are replaced on the surface instead.

Finally, in collaboration with the Chair for Multicomponent Materials of Prof. Faupel at the Faculty of Engineering, silver nanoparticles are produced in an external Haberland-type gas aggregation source and injected into the secondary plasma to create silver-silica core-shell nanoparticles. While island growth is observed initially, longer treatment durations yield a homogeneous silica coating with a thickness of 6 nm. This experiment acts as a proof of principle for the possibility of multi-step nanofabrication of specifically tailored nanoparticles for various applications.

Zusammenfassung

Der Übergang von Bulkmaterialien zu Nanopartikeln eröffnet eine Vielzahl an neuen Eigenschaften. Durch ihre Größe im Nanometerbereich besitzen diese ein extremes Verhältnis von Oberfläche zu Volumen und zeigen Quanteneinschlusseffekte, die in vielerlei Anwendungen zum Einsatz kommen, wie zum Beispiel der Katalyse, Biomedizin, Optoelektronik oder bei neuromorphen Systemen.

Diese Arbeit beschäftigt sich mit der Erzeugung und Behandlung von Kohlenstoff-, Silizium- und Silber-Silika-Kern-Schalen-Nanopartikeln in einer Plasmaentladung mit besonderem Fokus auf die in-situ Diagnostik. Durchgehende in-situ Kontrolle durch Fourier-transformierte Infrarotspektroskopie (FTIR) und Oberflächenplasmonenresonanz (LSPR) während der Plasmabehandlung erlaubt eine exzellente Kontrolle der Partikelparameter wie ihrer Größe, ihrer chemischen Zusammensetzung oder ihrer Oberflächenfunktionalisierung, die von zentraler Bedeutung für die verschiedenen Anwendungen sind. Die Ergebnisse aus diesen Untersuchungen werden durch Extraktion von Proben und ex-situ Transmissionselektronenmikroskopie fundiert.

Als ersten Schritt werden Kohlenstoffpartikel mit etwa 500 nm Durchmesser im Suleika Nano Experiment produziert und eingefangen. Dieses ist ein prototypischer Aufbau im Feld der staubigen Plasmen und dient der Untersuchung der Interaktionen von dichten Staubwolken mit einem Plasma. Eine Massenveränderung, die von vorherigen Experimenten berichtet wurde, wird mittels FTIR-Analyse auf Unreinheiten aus der Umgebungsluft zurückgeführt, die zur Aufnahme von Sauerstoff in das Partikelmaterial führen.

Nach diesen anfänglichen Experimenten wird die Synthese und Behandlung der Partikel in zwei separate Systeme aufgeteilt, welches die unabhängige Kontrolle der Systemparameter ermöglicht. Für die Experimente an Silizium-Halbleiter-Nanopartikeln wird eine externe, kapazitiv gekoppelte Plasmaquelle genutzt. Die Partikel werden anschließend in eine sekundäre, induktiv gekoppelte Plasmaentladung im E-Modus gespiesen und dort für die weitere Behandlung eingefangen. Eine Isotopenuntersuchung mittels FTIR zeigt, dass Deuterium sich im Bulkmaterial an vorhandene Wasserstoffgruppen anfügt, während es diese Gruppen auf der Partikeloberfläche stattdessen ersetzt.

In Kollaboration mit dem Lehrstuhl für Materialverbunde der Technischen Fakultät von Prof. Faupel werden abschließend Silbernanopartikel in einer externen Gasaggregationsclusterquelle vom Typ Haberland produziert und in die sekundäre Plasmaentladung gespiesen, um dort Silber-Silika-Kern-Schalen-Nanopartikel zu produzieren. Während zunächst Inselwachstum beobachtet wird, führen längere Behandlungsdauern zu einer homogenen Beschichtung der Partikel mit einer 6-nm-dicken Silikaschale. Dieses Experiment dient als Grundsatzbeweis der Möglichkeit von mehrschrittiger Nanofabrikation von speziell angepassten Nanopartikeln für die verschiedenen Anwendungsfelder.

Résumé

Les nanoparticules se distinguent des matériaux bulk par une série de nouvelles propriétés. Leurs dimensions nanométriques sont la source de rapports surface-volume extrêmes et d'effets de confinement quantique. Ils ont donc des nombreuses applications dans divers domaines tels que la catalyse, la biomédecine, l'optoélectronique et les systèmes neuromorphiques.

Cette thèse concerne la synthèse et le traitement de nanoparticules de carbone, de silicium et de type cœur-coquille d'argent-silice à l'aide de décharges de plasma, avec un accent particulier sur leur diagnostic in situ. Le monitorage continu in situ via la spectroscopie infrarouge à transformée de Fourier (FTIR) et la résonance plasmonique localisée de surface (LSPR) pendant le traitement au plasma permet un contrôle précis des propriétés des nanoparticules telles que leur taille, leur composition chimique ou leur fonctionnalisation de surface, qui sont essentielles pour leurs diverses applications. Les résultats sont confirmés par l'extraction d'échantillons pour la microscopie électronique en transmission ex situ.

Pour commencer, des particules de carbone d'un diamètre d'environ 500 nm ont été produites et confinées dans l'expérience Suleika Nano, une installation prototypique dans le domaine des plasmas poussiéreux pour l'étude des interactions entre des nuages de poussière denses dans un plasma. Le changement de masse des particules constaté par des expériences antérieures est attribué, grâce à l'analyse FTIR, aux impuretés de l'air ambiant qui entraînent l'incorporation d'oxygène dans les particules.

Après cette expérience initiale, la synthèse et le traitement des particules sont séparés en deux systèmes, permettant un contrôle indépendant de leurs conditions. Pour les expériences sur les nanoparticules de semi-conducteurs en silicium, une source externe de plasma à couplage capacitif est utilisée pour générer de petites particules de l'ordre du nanomètre. Elles sont ensuite injectées dans une décharge secondaire de plasma à couplage inductif en mode E pour être confinées et traitées à l'hydrogène. Des études isotopiques par FTIR utilisant du deutérium montrent l'ajout de deutérium dans le matériau bulk des particules tandis que les liaisons hydrogène existantes à la surface sont remplacées.

Enfin, en collaboration avec la chaire des matériaux multicomposants du prof. Faupel à la faculté d'ingénierie, des nanoparticules d'argent sont produites dans une source à agrégation gazeuse externe de type Haberland et injectées dans le plasma secondaire afin de créer des nanoparticules cœur-coquille d'argent-silice. Alors qu'une croissance en îlots est observée initialement, des durées de traitement plus longues permettent d'obtenir un revêtement de silice homogène d'une épaisseur de 6 nm. Cette expérience constitue une démonstration de faisabilité de la nanofabrication en plusieurs étapes de nanoparticules spécifiquement adaptées à diverses applications.

Contents

Acronyms

a-C:H amorphous hydrogenated carbon *(pp. 19, 24, 53, 54, 80, 83, 85, 86, 109, 111)*

a-Si:H amorphous hydrogenated silicon *(pp. 18, 19, 51, 87, 91, 109, 111)*

BSE backscattered electrons *(p. 38)*

CCP capacitively coupled plasma *(pp. 9–11, 50, 65, 67, 79, 95, 109)*

CTEM conventional transmission electron microscopy *(p. 38)*

DC direct current *(pp. 28, 64, 66, 67, 71)*

DLC diamondlike carbon *(pp. 54, 55)*

EDX energy-dispersive X-ray spectroscopy *(pp. 38, 39, 94, 98, 100–103)*

EELS electron energy loss spectroscopy *(p. 54)*

EPEX electrostatic particle extractor *(pp. 59, 60, 80)*

FRES forward recoil elastic scattering *(p. 54)*

FT-NMR Fourier-transform nuclear magnetic resonance *(p. 32)*

FTIR Fourier-transform infrared spectroscopy *(pp. 2, 21, 26, 29–32, 47–50, 68, 70, 80, 84, 87, 97, 103, 109, 110, 115, 116)*

GAS gas aggregation source *(pp. 21, 28, 29, 47, 71, 72, 79, 94, 96, 99, 109, 110)*

HAADF high-angle annular dark-field *(pp. 39, 100, 101)*

HMDSO hexamethyldisiloxane *(p. 47)*

HOMO highest occupied molecular orbital *(p. 22)*

IBA ion beam analysis *(p. 54)*

ICP inductively coupled plasma *(pp. 9–11, 64, 72, 110, 111)*

LO longitudinal optical *(pp. 57, 58)*

LSPR localised surface plasmon resonance *(pp. 2, 35, 37, 49, 94–97, 101, 103, 104, 109, 110)*

LUMO lowest unoccupied molecular orbital *(p. 22)*

MCT mercury cadmium telluride *(pp. 49, 50)*

MFC mass flow controller *(pp. 63, 65, 69, 71)*

MIR mid-infrared *(p. 48)*

NMR nuclear magnetic resonance spectroscopy *(pp. 32, 54)*

OML orbital motion limited *(pp. 11–13, 20, 84, 96)*

PECVD plasma enhanced chemical vapour deposition *(p. 26)*

PEEK polyether ether ketone *(p. 59)*

PTDF particle temperature density function *(p. 20)*

RF radio frequency *(pp. 9–11, 47, 62–64)*

SAED selected area electron diffraction *(p. 39)*

SE secondary electrons *(p. 38)*

SEM scanning electron microscopy *(pp. 38, 61, 80, 81, 101)*

STEM scanning transmission electron microscopy *(pp. 38, 100, 101)*

TEM transmission electron microscopy *(pp. 38, 94, 95, 98, 99, 101–103)*

TO transversal optical *(pp. 57, 58)*

UV-Vis ultraviolet-visible *(pp. 48–50, 95–98, 103)*

1 Introduction

When reducing the size of objects from the macroscopic scale to the nanoscale, a whole range of new properties emerges. A look at crystalline silicon nanoparticles shows, that for a particle with a diameter of 1 µm less than 1 % of atoms are located on its surface. Scaling it down to a size of 2 nm, the particle now consists of only 280 atoms, 120 of which are located on its surface [1, 2]. With these extreme surface-to-volume ratios, surface effects such as reactions with other surfactants [3], non-linear optical properties [4], and catalytic reactions [5] are strongly amplified.

Plasma synthesis of nanoparticles from precursor gasses has distinct advantages over the various other possible pathways. Compared to gas-phase chemical routes which require very high temperatures, the plasma can make use of inherent heating processes such as selective heating through ion recombination. Especially for nanoparticles this can create instantaneous particle temperatures up to 1000 °C above the gas temperature without the need for an additional heating setup [6]. Liquid-phase chemistry is often limited by the choice of solvents, which cannot reach temperatures high enough to create crystalline nanoparticles [7]. Finally, there are top-down approaches such as wet chemical etching of silicon wafers to obtain crystalline silicon nanoparticles. While these create particles with well-defined size and properties, the plasma approach offers better significantly scalability towards higher throughput [8].

Another strength of the plasma synthesis of nanoparticles is the possibility of using the plasma for further treatment steps. Low temperature plasmas provide a large flux of hot electrons as well as excited or ionised species and photons which enable a variety of possible plasmachemical reactions. Plasma treatments of nanoparticles can operate within seconds compared to liquid-phase treatment options which typically require reaction times of tens of minutes [1]. With these quick reaction times, in-flight treatments are a potent option for flow-through synthesis systems to create functionalised surfaces in the few seconds where the particles pass through the treatment plasma [9]. It is even possible to create coatings for core-shell nanoparticles [10–12], but the thickness of these shells is limited significantly by the residence time in the treatment plasma.

The goal of this work is to provide insight into the underlying processes during plasma treatment and improve on the previous in-flight techniques by confining particles in a plasma discharge over much longer time scales. Particles inside a plasma quickly gain a negative charge and are then confined in the ambipolar

electric field of the discharge, allowing residence times in the order of minutes to hours. It is then possible to slow down the treatment process through limiting the flow of treatment gasses and observe changes to the nanoparticles in detail. Monitoring is performed via Fourier-transform infrared spectroscopy (FTIR) and additional localised surface plasmon resonance (LSPR) spectroscopy for metallic nanoparticles. These techniques allow measuring changes to the nanoparticle surface over the course of the treatment and give precise control over the resulting particle properties.

The long confinement times open the door for treatments that are difficult to achieve with in-flight methods. Shells with several nanometres of thickness are easily realised and multi-step processes with several shell layers, surface functionalisations, and even gradual changes in composition are possible as a result of this work. One particularly promising application that was explored by our collaborating Chair for Multicomponent Materials of Prof. Faupel at the Faculty of Engineering is the use of silver-silica and silver-carbon core-shell nanoparticles for applications in neuromorphic computing. The metallic particles are usually embedded in an insulating matrix and show memristive behaviour once a critical particle density is reached [13–15]. By coating the nanoparticles directly with an insulating silica shell, the need for a matrix is removed opening the possibility for truly three-dimensional networks of nanoparticles.

Furthermore for semiconductors, when particle dimensions become smaller than the exciton Bohr radius, quantum confinement effects play a significant role in their optical properties. Lowering the dimensionality from 3-d bulk material towards 2-d thin films, 1-d nanorods, and finally 0-d quantum dots leads to an increasing discretisation of energy states and changes in the band structure [16]. For silicon nanoparticles in particular this can change the previously indirect band gap into a direct one, increasing the quantum efficiency of the particles by several orders of magnitude and enabling applications, e.g. in solar cells [17, 18] or light-emitting devices [19, 20].

Photoluminescent silicon nanoparticles have seen intensive research efforts in the last 20 years with the goal of producing light-emitting devices [7, 21–25]. The photoluminescence quantum yield of such particles is very dependent on its properties, such as size [26], crystallinity [23], or surface functionalisation [27]. Furthermore, nanoparticles can be used in biomedicine for sensing, drug delivery, or imaging applications, where once again the particle's size and surface functionalisation determine the efficiency of cellular uptake [28]. Seeing the plasma not as a black box, where particles are put in and treated particles come out, but rather having a fundamental understanding of the plasma interactions allows fine-grained control of these particle properties and makes it possible to tailor the nanoparticles precisely for their specific application.

This work is structured as follows: The fundamental principles behind plasma discharges, dusty plasmas, and the formation, treatment, and diagnostics of

nanoparticles are presented in chapter 2. An overview over the different experimental setups for creating carbon and silicon nanoparticles, as well as silver-silica core-shell nanoparticles is given in chapter 3. In chapter 4 the results obtained with these experimental setups are presented for the three different particle types. The work concludes in chapter 5 with a summary of the presented results and short-form conclusions are drawn.

References

[1]F. Hua, M. T. Swihart, and E. Ruckenstein, "Efficient Surface Grafting of Luminescent Silicon Quantum Dots by Photoinitiated Hydrosilylation", Langmuir **21**, 6054–6062, ISSN: 0743-7463 (2005).

[2]L. L. Araujo and M. C. Ridgway, "Embedded nanoparticles", in *Handbook of Nanophysics: Nanoparticles Quantum Dots*, edited by K. D. Sattler (CRC Press Taylor & Francis Group, Boca Raton, London, New York, 2010), pp. 405–418, ISBN: 978-1-4200-7545-8.

[3]H. Modrow, "Tuning Nanoparticle Properties—The X-ray Absorption Spectroscopic Point of View", Applied Spectroscopy Reviews **39**, 183–290 (2004).

[4]J. Requejo-Isidro, R. del Coso, J. Solis, J. Gonzalo, and C. N. Afonso, "Role of surface-to-volume ratio of metal nanoparticles in optical properties of Cu:Al_2O_3 nanocomposite films", Applied Physics Letters **86**, 193104 (2005).

[5]A. Z. Moshfegh, "Nanoparticle catalysts", Journal of Physics D: Applied Physics **42**, 233001 (2009).

[6]L. Mangolini and U. Kortshagen, "Selective nanoparticle heating: Another form of nonequilibrium in dusty plasmas", Physical Review E **79**, 026405, ISSN: 1539-3755 (2009).

[7]U. R. Kortshagen, R. M. Sankaran, R. N. Pereira, S. L. Girshick, J. J. Wu, and E. S. Aydil, "Nonthermal Plasma Synthesis of Nanocrystals: Fundamental Principles, Materials, and Applications", Chemical Reviews **116**, 11061–11127, ISSN: 0009-2665 (2016).

[8]H. Wiggers and A. Lorke, "Silicon nanocrystals", in *Handbook of Nanophysics: Nanoparticles Quantum Dots*, edited by K. D. Sattler (CRC Press Taylor & Francis Group, Boca Raton, London, New York, 2010), ISBN: 978-1-4200-7545-8.

[9]L. Mangolini and U. Kortshagen, "Nonthermal Plasma Synthesis of Silicon Nanocrystals", in *Silicon Nanocrystals*, edited by L. Pavesi and R. Turan (Wiley-VCH Verlag GmbH & Co. KGaA, Weinheim, 2010-04), pp. 309–348, ISBN: 978-3-527-32160-5.

[10]J. Bai and J.-P. Wang, "High-magnetic-moment core-shell-type FeCo–Au/Ag nanoparticles", Applied Physics Letters **87**, 152502 (2005).

[11]J. Hanuš, M. Vaidulych, O. Kylián, A. Choukourov, J. Kousal, I. Khalakhan, M. Cieslar, P. Solař, and H. Biederman, "Fabrication of Ni@Ti core–shell nanoparticles by modified gas aggregation source", Journal of Physics D: Applied Physics **50**, 475307 (2017).

[12]T. Kretková, J. Hanuš, O. Kylián, P. Solař, M. Dopita, M. Cieslar, I. Khalakhan, A. Choukourov, and H. Biederman, "In-flight modification of Ni nanoparticles by tubular magnetron sputtering", Journal of Physics D: Applied Physics **52**, 205302 (2019).

[13]J.-H. Cha, S. Y. Yang, J. Oh, S. Choi, S. Park, B. C. Jang, W. Ahn, and S.-Y. Choi, "Conductive-bridging random-access memories for emerging neuromorphic computing", Nanoscale **12**, 14339–14368 (2020).

[14]Z. Kuncic and T. Nakayama, "Neuromorphic nanowire networks: principles, progress and future prospects for neuro-inspired information processing", Advances in Physics: X **6**, 10.1080/23746149.2021.1894234 (2021).

[15]N. Carstens, B. Adejube, T. Strunskus, F. Faupel, S. Brown, and A. Vahl, "Brain-like critical dynamics and long-range temporal correlations in percolating networks of silver nanoparticles and functionality preservation after integration of insulating matrix", Nanoscale Advances **4**, 3149–3160 (2022).

[16]A. Yoffe, "Low-dimensional systems: quantum size effects and electronic properties of semiconductor microcrystallites (zero-dimensional systems) and some quasi-two-dimensional systems", Advances in Physics **42**, 173–262 (1993).

[17]O. E. Semonin, J. M. Luther, S. Choi, H.-Y. Chen, J. Gao, A. J. Nozik, and M. C. Beard, "Peak External Photocurrent Quantum Efficiency Exceeding 100% via MEG in a Quantum Dot Solar Cell", Science **334**, 1530–1533 (2011).

[18]G. H. Carey, A. L. Abdelhady, Z. Ning, S. M. Thon, O. M. Bakr, and E. H. Sargent, "Colloidal Quantum Dot Solar Cells", Chemical Reviews **115**, 12732–12763 (2015).

[19]B. S. Mashford, M. Stevenson, Z. Popovic, C. Hamilton, Z. Zhou, C. Breen, J. Steckel, V. Bulovic, M. Bawendi, S. Coe-Sullivan, and P. T. Kazlas, "High-efficiency quantum-dot light-emitting devices with enhanced charge injection", Nature Photonics **7**, 407–412 (2013).

[20]X. Dai, Z. Zhang, Y. Jin, Y. Niu, H. Cao, X. Liang, L. Chen, J. Wang, and X. Peng, "Solution-processed, high-performance light-emitting diodes based on quantum dots", Nature **515**, 96–99 (2014).

[21]L. Mangolini, E. Thimsen, and U. Kortshagen, "High-Yield Plasma Synthesis of Luminescent Silicon Nanocrystals", Nano Letters **5**, 655–659 (2005).

[22]M. C. Beard, K. P. Knutsen, P. Yu, J. M. Luther, Q. Song, W. K. Metzger, R. J. Ellingson, and A. J. Nozik, "Multiple Exciton Generation in Colloidal Silicon Nanocrystals", Nano Letters **7**, 2506–2512 (2007).

[23]R. Anthony and U. Kortshagen, "Photoluminescence quantum yields of amorphous and crystalline silicon nanoparticles", Physical Review B **80**, 115407 (2009).

[24]J. B. Miller, A. R. V. Sickle, R. J. Anthony, D. M. Kroll, U. R. Kortshagen, and E. K. Hobbie, "Ensemble Brightening and Enhanced Quantum Yield in Size-Purified Silicon Nanocrystals", ACS Nano **6**, 7389–7396 (2012).

[25]R. Mandal, K. O'Shea, and R. Anthony, "Silicon nitride-capped silicon nanocrystals via a nonthermal dual-plasma synthesis approach", Journal of Vacuum Science & Technology A: Vacuum, Surfaces, and Films **36**, 051303, ISSN: 0734-2101 (2018).

[26]M. Sykora, L. Mangolini, R. D. Schaller, U. Kortshagen, D. Jurbergs, and V. I. Klimov, "Size-Dependent Intrinsic Radiative Decay Rates of Silicon Nanocrystals at Large Confinement Energies", Physical Review Letters **100**, 067401 (2008).

[27]L. Mangolini, D. Jurbergs, E. Rogojina, and U. Kortshagen, "Plasma synthesis and liquid-phase surface passivation of brightly luminescent Si nanocrystals", Journal of Luminescence **121**, 327–334 (2006).

[28]J. Rauch, W. Kolch, S. Laurent, and M. Mahmoudi, "Big signals from small particles: Regulation of cell signaling pathways by nanoparticles", Chemical Reviews **113**, 3391–3406, ISSN: 0009-2665 (2013).

2

Fundamentals

The field of plasmas deals with what is often called the *fourth state of matter* [1], describing a partially or fully ionised gas of electrons and ions. There are a wide range of plasmas ranging from the high-pressure, high-temperature regime in astrophysics to low-pressure non-equilibrium laboratory systems. This chapter will not attempt to give a full overview over the entirety of the field, but rather present a selection of fundamental aspects of the low pressure, low temperature, non-equilibrium plasmas that were used in this work for the synthesis and treatment of nanoparticles. For a more comprehensive overview, the reader is referred to common textbooks such as [2–4].

This chapter first gives an overview over the fundamental principles behind plasma discharges in general and the typical capacitively and inductively coupled laboratory plasmas in particular. It then describes the effects of the plasma on a cloud of nanoparticles brought into the volume, which typically charge up in the electron-rich environment and can even deplete the plasma of a significant portion of its electron population. From these physical effects, the focus then shifts towards chemical considerations of the plasma-surface interactions with its different reaction mechanisms and effects such as selective heating that specifically occur for nanoparticles given their small thermal mass. Afterwards, focusing closer on each individual nanoparticle, the photoluminescence of semiconductor nanoparticles caused by their nanoscale dimensions and the synthesis mechanisms for creating carbon, silicon and noble metal nanoparticles in a plasma are described. The chapter closes with the fundamental concepts behind the different in and ex situ diagnostics used in this work.

2.1 Plasma discharges

In contrast to a neutral gas, where particles interact via the Van der Waals force scaling with the distance $\propto r^{-6}$, the charged components of a plasma interact via the Coulomb force scaling with $\propto r^{-2}$. This difference leads to the so-called collective behaviour as the particles can interact over comparably long distances. When a point-like charge Q is brought into a plasma, it creates a displacement of the charge distribution in the system. Like-charged plasma components will be repelled, whereas unlike-charged particles will be attracted, creating a net space charge shielding the charge Q from the rest of the plasma. If we assume Q is placed in origin of the coordinate system and the plasma only consists of

singly-ionised particles, we can express the system with a Poisson equation:

$$\Delta\Phi = -\frac{1}{\varepsilon_0}\left[Q\delta(\vec{r}) - en_\mathrm{e}(\vec{r}) + en_\mathrm{i}(\vec{r})\right] , \tag{2.1}$$

where Φ is the electrostatic potential, ε_0 the vacuum permittivity, δ the Dirac delta function, and $n_{\mathrm{e,i}}(\vec{r})$ the local electron and ion density around the charge Q.

The solution of this equation, assuming a small perturbation $e|\Phi| \ll k_\mathrm{B}T$, is the Debye-Hückel potential

$$\Phi(r) = \frac{Q}{4\pi\varepsilon_0 r}\exp\left(-\frac{r}{\lambda_\mathrm{D}}\right) , \tag{2.2}$$

where λ_D is the Debye shielding length, which describes the typical length scale of this shielding interaction. It consists of the individual electron and ion shielding lengths λ_De, λ_Di and can be described using the unperturbed electron density n_e0 and the temperature $T_{\mathrm{e,i}}$ of electrons and ions:

$$\lambda_\mathrm{D}^{-2} = \lambda_\mathrm{De}^{-2} + \lambda_\mathrm{Di}^{-2} = \frac{e^2 n_\mathrm{e0}}{\varepsilon_0}\left(\frac{1}{k_\mathrm{B}T_\mathrm{e}} + \frac{1}{k_\mathrm{B}T_\mathrm{i}}\right) , \tag{2.3}$$

where e is the elementary charge. To enable this collective behaviour the definition of a plasma often requires that the extent L of the plasma is sufficiently larger than the Debye shielding length: $L \gg \lambda_\mathrm{D}$. Furthermore, the Debye sphere, i.e. the sphere with radius λ_D, needs to contain a sufficiently large number of charge carriers to be able to propagate the information needed for collective behaviour: $\frac{4}{3}\pi\lambda_\mathrm{D}^3 n_{\mathrm{e,i}} \gg 1$.

While the charge distribution in a plasma can be disturbed locally, it maintains neutrality on scales larger than the Debye shielding length. This property is called quasineutrality and can be expressed globally for a system containing ions of various charges q_k as:

$$\left|-en_\mathrm{e0} + \sum_k q_k n_{\mathrm{i0},k}\right| \ll en_\mathrm{e0} , \tag{2.4}$$

where $n_{\mathrm{i0},k}$ describes the density of ions carrying q_k elementary charges. In the case of singly ionised ions this simplifies to the common expression of quasineutrality as $n_\mathrm{e0} = n_\mathrm{i0}$. If charged dust particles are present in the system, the quasineutrality expression needs to be modified accordingly:

$$\left|-en_\mathrm{e0} + \sum_k q_k n_{\mathrm{i0},k} + q_\mathrm{d} n_\mathrm{d}\right| \ll en_\mathrm{e0} , \tag{2.5}$$

where q_d is the charge on a single dust particle and n_d describes the particle number density.

Up to this point, the reaction of the plasma to the point-like charge Q was only considered electrostatically. The shielding also has a temporal aspect as the

information about the perturbation needs to be propagated through the plasma. Once again assuming a small perturbation $e|\Phi| \ll k_\mathrm{B}T$, the typical velocity of an electron is determined by its thermal velocity $v_\mathrm{th,e} \approx \sqrt{k_\mathrm{B}T_\mathrm{e}/m_\mathrm{e}}$. To propagate the information of the perturbation into the plasma, the electron needs to move to its new position a typical length scale λ_De away. This movement takes a typical response time $\tau_\mathrm{e} \approx \lambda_\mathrm{De}/v_\mathrm{th,e}$. The same consideration applies analogously for ions and can be expressed as the plasma frequency:

$$\omega_{\mathrm{p}j} = \frac{v_{\mathrm{th},j}}{\lambda_{\mathrm{D}j}} = \sqrt{\frac{n_{j0}e^2}{\varepsilon_0 m_j}}\,, \text{ with } j = \mathrm{e}, \mathrm{i}\,. \tag{2.6}$$

This frequency is significantly different for electrons and ions. In typical laboratory plasmas with densities in the range of $(0.1\text{–}5) \cdot 10^{15}\,\mathrm{m}^{-3}$, the ion plasma frequency is in the range of 0.3–2 MHz, whereas the electron plasma frequency is in the range of 90–600 MHz. For this reason, radio frequency (RF) plasmas are typically operated in the ISM radio band at a frequency of 13.56 MHz or its first harmonic at 26.12 MHz. While ions are too heavy to follow this excitation, electrons are affected by it leading to collisional ionisation as the basis of plasma formation. The next section will explore these dynamics further.

2.1.1 Plasma generation

For a plasma discharge to be sustainable, power needs to be coupled in to offset loss processes, e.g. through photon emission or fluxes towards walls. RF capacitively coupled plasmas (CCPs) provide this power through currents driven by a quickly oscillating voltage between the electrodes. This leads to the formation of sheath regions in front of the electrodes with large voltage drops that limit the applied power to the plasma. Inductively coupled plasmas (ICPs) circumvent this by inducing the current directly in the plasma itself leading to a significantly lower voltage drop across the sheath. An ICP discharge can reach plasma densities several orders of magnitude higher than comparable CCP discharges.

Capacitively coupled plasma discharges

The prototypical form of a CCP discharge is the parallel plate discharge depicted in fig. 2.1a. It consists of two plates between which the plasma is generated by applying an oscillating RF voltage. Given a driving voltage with a frequency $\omega^2 \gg \omega_\mathrm{pi}^2$, the ions cannot follow the oscillation and only react to the time-averaged potential, whereas the electrons can follow as $\omega_\mathrm{pe}^2 \gg \omega^2$. A sheath forms in front of each electrode, which is a space charge region where the quasineutrality of the plasma breaks down due to the ion and electron fluxes to the electrode. As the oscillating potential on the electrode acts on the electrons, the resulting sheath width oscillates.

Two heating processes describe the power influx into the plasma which keeps the discharge stable. Ohmic heating occurs due to the ohmic resistance of the

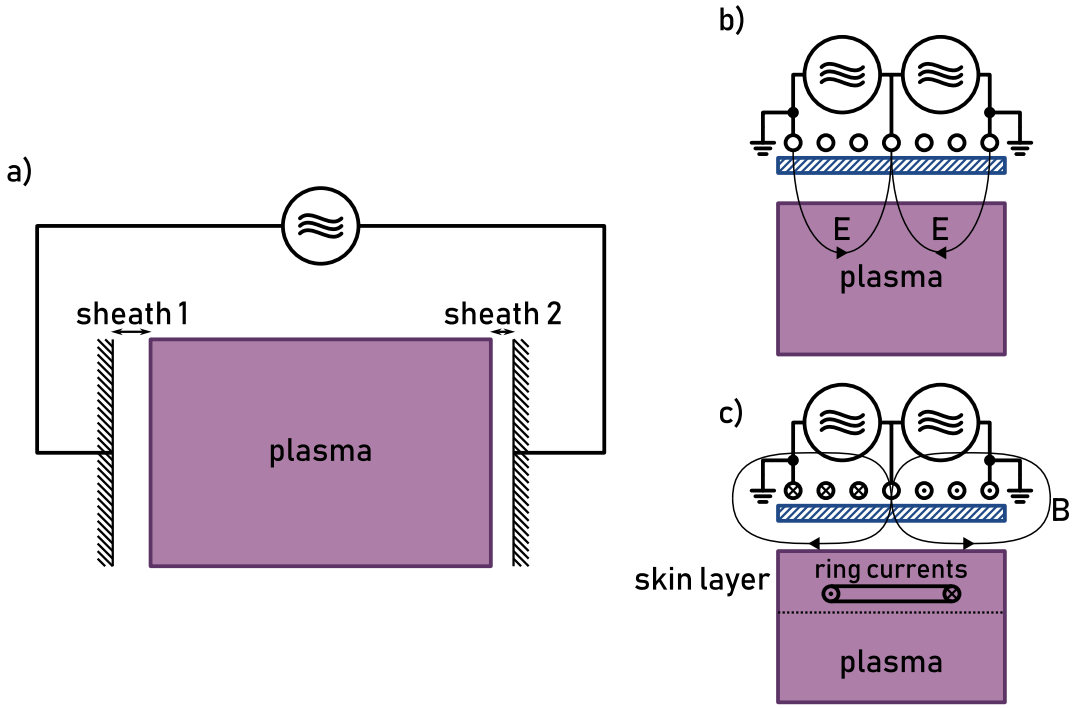

Figure 2.1: a) Sketch of a capacitively coupled plasma. An RF voltage is applied to two parallel plate electrodes, creating a discharge with sheaths in front of the electrodes. b) Sketch of an inductively coupled plasma at low powers. Coupling occurs via electric fields propagating through the dielectric barrier indicated in blue. c) Sketch of an inductively coupled plasma at high powers. Coupling occurs via magnetic fields inducing ring currents in the skin layer of the plasma. Adapted from [3, 4].

plasma. Microscopically, this is caused by collisions of the moving electrons with the neutrals in the plasma. Its impact depends on the plasma density as well as the electron-neutral collision frequency dictated by the neutral gas density.

The oscillating nature of the sheath further leads to stochastic heating. Here, electrons are reflected by the large changing fields in the high-voltage sheath, often compared to the reflection of a ball on a moving tennis racket. In the matrix sheath model, the energy gain from this heating process is frequency dependent and scales with ω^2/ω_{pe}^2. Therefore, by changing the excitation frequency, the ratio of ohmic to stochastic heating can be varied.

Inductively coupled plasma discharges

When higher plasma densities are needed, inductive coupling presents a plasma setup capable of producing densities several orders of magnitude higher than achievable using capacitive coupling at comparable powers. An ICP discharge uses a coil to create fields that couple into the plasma similar to a transformer, where the plasma acts as the secondary coil with a single turn. Depending on

the applied power two operational modes exist: the E-mode at low powers and the H-mode at higher powers (see figs. 2.1b and 2.1c).

In the E-mode, the coupling is dominated by the electrostatic fields of the RF potential differences between the windings of the coil. The plasma density is low enough for the fields to fully penetrate the plasma region, creating a discharge similar to a CCP. Increasing the supplied power leads to a sudden transition into the H-mode characterised by a significantly higher plasma density. Here, the energy is deposited directly in the first layers of the plasma due to the skin effect. A ring current is induced in this skin layer with opposite phase of the exciting coil. Heating occurs both through ohmic heating and a collisionless stochastic process, where electrons are reflected by the quickly changing inductive fields similar to the stochastic heating in the CCP case.

While this work was performed on an ICP setup, it was exclusively operated in the E-mode for nanoparticle treatments. A transition into the H-mode led to the dissociation of any nanoparticles brought into the plasma, which will be shown in detail in section 3.5.

2.2 Effects in dusty plasmas

This section gives a short overview over the aspects of dusty plasmas most relevant for this work. It largely follows arguments which can be found in scientific textbooks on this topic such as references [4, 5]. First, the orbital motion limited (OML) model will be presented as the central way of describing the charging of particles in a plasma using the incoming fluxes of electrons and ions and its limitations seen in the Havnes effect in high particle density situations. Then, the possibility of confining particles in the plasma will be shown through an examination of the various forces acting on charged particles leading to a force balance capable of holding the particles in the plasma volume for extended durations.

2.2.1 Charging of particles in a plasma

When particles are brought into a plasma, they are charged by the incoming flux of electrons and ions. In a typical laboratory situation, the flux of electrons is higher than that of ions because of their lower mass and the resulting higher average velocity[1], leading to a net negative charge on the particle. This situation is described by the orbital motion limited (OML) model, which gives the collision cross section σ_c for a particle with surface potential Φ as:

$$\sigma_c = \pi b_c^2 = \pi r_d^2 \left(1 - \frac{2q\Phi}{mv^2}\right), \tag{2.7}$$

where b_c is the collection radius, r_d the particle's radius, and q the charge of the incoming charge carrier with mass m and velocity v. For $q\Phi \leq 0$, e.g. for positive

[1] Even before considering their significantly higher temperatures in a non-thermal plasma.

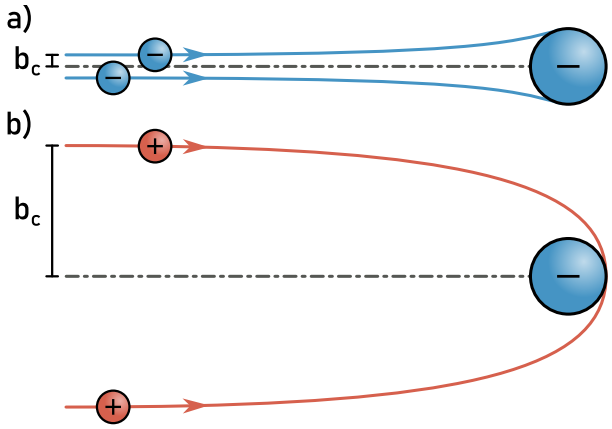

Figure 2.2: Collection radius b_c of an incoming particle for a) a repulsive and b) an attracting potential. Adapted from [4].

ions on a negatively charged particle, the particle's collection radius is larger than its geometric cross section, and respectively smaller for electrons (see fig. 2.2).

Assuming a Maxwellian velocity distribution for both electrons and ions which interact with a particle of radius $r_d < \lambda_D$ and disregarding collisions, the current of electrons and ions on a negatively charged particle can be derived as:

$$\begin{aligned} I_e &= -n_e e v_{th,e} \pi r_d^2 \exp\left(\frac{e\Phi}{k_B T_e}\right), \\ I_i &= n_i e v_{th,i} \pi r_d^2 \left(1 - \frac{e\Phi}{k_B T_i}\right), \end{aligned} \tag{2.8}$$

with $v_{th,j} = \sqrt{8 k_B T_j / (\pi m_j)}$ the thermal velocity of electrons and ions ($j = e, i$ respectively). In the repulsive case, the Boltzmann factor $\exp[e\Phi/(k_B T_e)]$ describes the effect of the potential barrier for electrons presented by the negatively charged particle. For ions, the attractive potential simplifies the underlying integral to result in the so-called OML factor $[1 - e\Phi/(k_B T_i)]$.

Once the system equilibrates, the particle reaches the so-called floating potential Φ_{fl} where ion and electron currents are equal. The resulting implicit equation can be solved numerically and only depends on the temperature ratio T_e/T_i and mass ratio m_e/m_i. Using the particle's floating potential, its charge q_d can be determined by modelling the system as a spherical capacitor with capacitance C:

$$q_d = C\Phi_{fl} = 4\pi\varepsilon_0 r_d \left(1 + \frac{r_d}{\lambda_D}\right) \Phi_{fl}\,. \tag{2.9}$$

For nanoparticles the radius is sufficiently smaller than the Debye length, so that $q_d \propto r_d$.

While this model works well for microparticles, it breaks down for very dense nanoparticle clouds as the particle density n_d approaches n_{e0}/q_d. The Havnes parameter P is a good measure for this depletion of electrons [6–8]:

$$P = 4\pi\varepsilon_0 r_d \frac{k_B T_e}{e^2} \frac{n_d}{n_{i0}}\,. \tag{2.10}$$

With increasing P, a larger portion of the available electron population is located on the nanoparticles, which raises the question of how the plasma can operate under highly electron-depleted conditions. In reality, the dust does not only reduce the electron density, but also strongly influences other parameters such as the electron energy distribution function and the density of excited states [9, 10], which in turn keeps ionisation rates high enough for the plasma to continue operation, i.e. n_i becomes greater than the initial $n_{\mathrm{i}0}$ used in the definition of the Havnes parameter.

Even further, for $P \gtrsim 1$ charging does not follow the OML model any more, as the incoming electron current breaks down. For a typical laboratory situation with a particle diameter of about 400 nm, ion densities in the order of $10^{15}\,\mathrm{m}^{-3}$, and dust densities in the order of $10^{13}\,\mathrm{m}^{-3}$, dust charges of around 20 elementary charges were measured, whereas the OML model would predict 1600 elementary charges for particles of that size [11]. In the theoretical limit $P \to \infty$, where all electrons are located on the particles, the electron density reaches zero. Using the adjusted quasineutrality condition in eq. (2.5), the dust charge is then solely determined by the ion and dust densities, yielding $q_\mathrm{d} = n_\mathrm{i}/n_\mathrm{d}$ for a singly ionised plasma.

2.2.2 Confinement of charged particles

There are a number of forces acting on a charged particle with radius r_d in a plasma environment (see fig. 2.3):

Gravitational force $F_\mathrm{g} \propto r_\mathrm{d}^3$
: In all earthbound plasma experiments, the gravitational force acts on the particle. It is proportional to the particle's mass $m \propto r_\mathrm{d}^3$, compared to the other forces which scale with r_d^2 or r_d. This leads to it being the dominant force for microparticles whereas often being negligible for nanoparticles.

Neutral drag force $F_\mathrm{n} \propto r_\mathrm{d}^2$
: Moving particles experience a drag force caused by collisions with the neutral gas; a situation that is described by Epstein friction [12]. The magnitude of this friction force is determined by the neutral gas density and its thermal velocity, the type of reflection (specular vs diffuse) of the neutral gas on the particle surface, as well as the particle's geometric cross section, which results in a dependency $\propto r_\mathrm{d}^2$.

Ion drag force $F_\mathrm{i} \propto r_\mathrm{d}^2$
: Flowing ions, e.g. from the ambipolar electric field that develops in a confined system, lead to a drag force on the particles. As both ions and the particles are charged, momentum can be transferred both through collisions or the bending of ion trajectories. These separate phenomena are typically split up into the collection force and the orbit force, which together constitute the ion drag force.

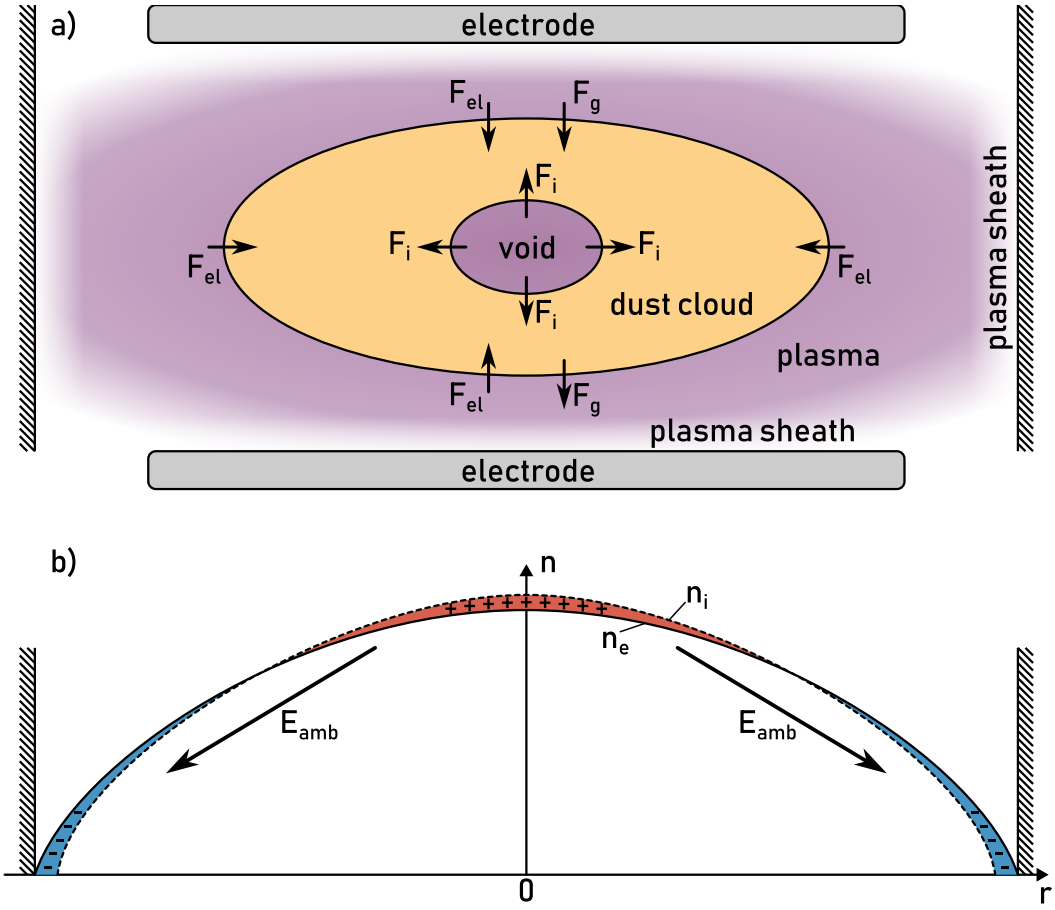

Figure 2.3: a) Sketch of a typical parallel plate discharge containing a dust cloud depicted in yellow. The gravitational, electrostatic, and ion drag forces acting on the particles are shown as arrows. The balance between ion drag force and electric field force leads to the formation of a dust-free region marked as the void. b) Sketch of the slightly different ion and electron density profiles $n_{e,i}$ leading to the formation of an ambipolar electric field. Adapted from [4].

Thermophoretic force $F_{th} \propto r_d^2$

When a temperature gradient is present in the neutral gas, the different momentum transferred from the hotter gas on one side compared to the colder gas on the other side of the particle leads to a net force scaling with the geometric cross section $\propto r_d^2$.

Electrostatic force $F_{el} \propto r_d$

The presence of electrostatic fields leads to a force on the charged particles. This is dependent on the particle charge, which according to eq. (2.9) is proportional to $r_d(1 + r_d/\lambda_D)$. As the Debye length in typical laboratory plasmas is in the order of millimetres, this results in a net proportionality $\propto r_d$ for micro- and nanoparticles.

Interparticle force F_Y

Finally, in a system with more than one particle, interparticle forces exist between each pair of particles. This interaction is shielded by the presence

of the plasma as described in section 2.1, modifying the Coulomb potential of each particle to the so-called Yukawa potential which considers an additional exponential shielding length that in the isotropic case in the bulk of a plasma is equal to the Debye length. The Coulomb force between two particles carrying charges $q_{1,2}$ in a distance r_{12} from each other is therefore modified to yield:

$$F_{\mathrm{Y}}(r_{12}) = -\frac{q_1 q_2}{4\pi\varepsilon_0 r_{12}^2}\left(1+\frac{r_{12}}{\lambda_{\mathrm{D}}}\right)\exp\left(-\frac{r_{12}}{\lambda_{\mathrm{D}}}\right). \tag{2.11}$$

In most dusty plasma situations where particles are present in the entire plasma volume, i.e. microparticles in microgravity experiments [13] or earth-bound nanoparticle experiments such as the one presented in this work, a dust-free region forms in the centre of the discharge called a *void* (see fig. 2.3). In a typical parallel plate discharge, the void forms because of the electric field caused by ambipolar diffusion. The field acts on the particles both directly through the electrostatic force as well as indirectly through generating streaming ions which lead to an ion drag force. The balance between outward facing ion drag force and inward facing electrostatic force defines an equilibrium point around which the dust cloud fills up, leaving the dust-free void in the middle and defining a outer boundary that provides the confinement of the dust cloud.

2.3 Plasma-surface interactions

The interactions in a low-pressure non-thermal plasma are well known and can be described from multiple perspectives such as kinetic and statistical approaches focusing on particle ensembles and the self-consistent description of the electric and magnetic fields they cause, or hydrodynamic approaches viewing the ions and electrons as macroscopic fluids [14]. Once that plasma comes into contact with a surface, the situation becomes disproportionately more complicated with many unknown quantities depending on the specific materials involved. It is comparatively easy to describe the surface processes by listing macroscopic system quantities such as used gas mixture, discharge power, or geometry that result in macroscopic film or particle properties like surface roughness, composition, stress, hardness, and so on. A deeper understanding of the underlying processes necessitates a microscopic view of the involved plasma-surface interaction processes and the particle and energy balances involved on both sides. While macroscopic descriptions have lead to a variety of technological applications, the underlying microscopic processes are yet to be fully examined and understood [15].

The central process in plasma-surface interactions is a particle (electron, ion, neutral, radical, or metastable) from the plasma volume impinging the surface. While electrons mainly play a role in the charge and energy balances, the impinging larger species interact with the surface in varied ways. Depending on their kinetic energy, they can adsorb at the surface at low energies, cause sputtering

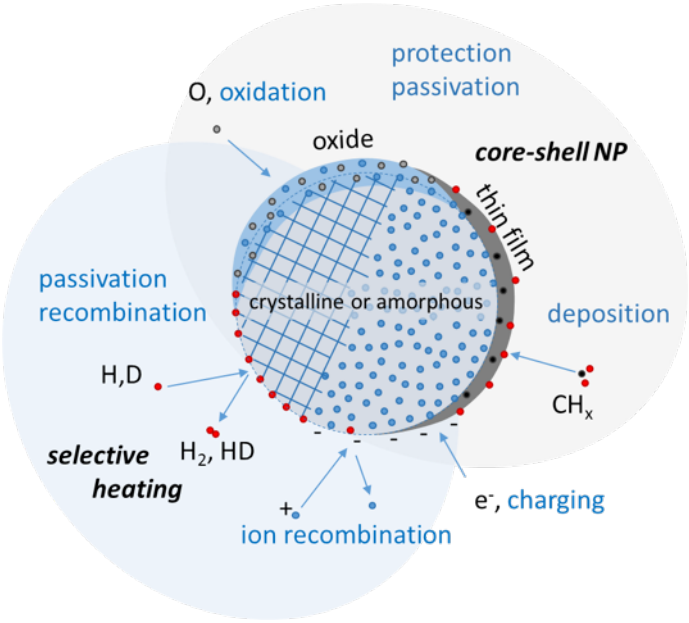

Figure 2.4: Overview of the various pathways for plasma interactions on a silicon nanoparticle. Atomic hydrogen and ions from the plasma can perform selective heating through recombination processes on the surface. Furthermore, passivation can be obtained through oxygen injection, generating an oxide layer or addition of other reactive groups depositing a thin film shell on the nanoparticle. Used with permission from Jan Benedikt, private communication.

at high energies, or be reflected at the surface in the intermediate energy region, causing heating of the substrate. An example for the possible passivation reactions for silicon nanoparticles is given in fig. 2.4. This chapter will provide insight into the various microscopic processes involved in these interactions.

2.3.1 Adsorption

Adsorption differentiates into two stages: physisorption and chemisorption [16]. Physisorption describes the trapping of the impinging particle mediated by electrostatic forces with the released adsorption heat being comparatively low with $E_{\text{ads}} < 0.5\,\text{eV}$, whereas chemisorption is mediated by valence forces leading to covalent bonds with larger amounts of released energy. Often, impinging molecules first need to lose a part of their kinetic energy in the collision with the surface to be able to be bound in a physisorbed state. Afterwards, they may diffuse along the surface or even into the solid, until they either become desorbed or form a chemisorbed bond at a fitting site.

An incoming molecule may also undergo dissociative chemisorption. Here, the molecule breaks apart after physisorption, leaving two parts that can each undergo chemisorption afterwards. Depending on the energy levels of the involved states, an activation barrier may lie between the physisorbed molecular state and the chemisorbed state of its parts. Both the kinetic energy brought in by the incoming molecule and the thermal energy of the surface can aid in overcoming

this barrier and lead to chemisorption. One prototypical example of this process is the dissociative chemisorption of molecular hydrogen on a silicon surface [17].

The absorption process is summarized by the sticking coefficient γ, which describes the probability of an impinging particle to be trapped on the surface. In most experiments, the sticking coefficient is inaccessible and only the surface loss probability β can be measured, which is the probability of loss of an impinging particle in surface reactions, which includes sticking but also reactions that create volatile non-reactive compounds, e.g. the abstraction from a surface hydrogen $SiH_3(s) + H \longrightarrow SiH_4(g)$.

In the binary collision approximation, the maximal energy T_{max} an impinging projectile with kinetic energy E_{kin} can transfer to the surface is determined by the masses $m_{p,t}$ of the involved projectile and target:

$$T_{max} = E_{kin} \frac{4 m_p m_t}{\left(m_p + m_t\right)^2} . \tag{2.12}$$

This energy is then transferred to the surface and dissipated via phonon excitation. For a light projectile such as atomic hydrogen the transferable energy is small, leading to a low sticking coefficient for most materials, as the fraction of the energy distribution function below the chemisorption bonding threshold is low.

Up to now only the adsorption of a single projectile was considered. Looking at the entire flux j of impinging species, the surface coverage $\Theta = n_{ads}/n_0$ plays a significant role, i.e. ratio of the surface density n_{ads} of adsorbed particles to the total density of available surface sites. The overall rate of adsorption is therefore described by

$$\frac{\mathrm{d}n_{ads}}{\mathrm{d}t} = \gamma j f(\Theta) , \tag{2.13}$$

with $f(\theta)$ describing the ability of the surface to accommodate another adsorbant. In the simplest case, this can simply be defined as the fraction of unoccupied sites $f(\Theta) = 1 - \Theta$.

To get a more realistic picture of the adsorption rate, time-dependent processes can be included in this equation such as the desorption time scale τ_{des}, after which particles desorb and return to the plasma, or the time τ_{chem} it takes for the chemisorption reaction to occur:

$$\frac{\mathrm{d}n_{ads}}{\mathrm{d}t} = \gamma j f(\Theta) - \frac{n_0 \Theta}{\tau_{des}} - \frac{n_0 \Theta}{\tau_{chem}} . \tag{2.14}$$

As these time scales tend to also be temperature-sensitive, the surface temperature plays a significant role in this model. An increased surface temperature leads to thermal desorption overcoming the chemisorption reaction and slowing down the deposition, e.g. of epitaxial Si on a crystalline Si substrate [18].

If the impinging particle can only transfer a small fraction of their kinetic energy, but is still weakly bound to an adsorbed state, it can diffuse on the surface as a so-called *hot precursor*. It performs a random walk along neighbouring

chemisorption sites with a small chemisorption probability at each. This process competes with the thermal desorption back into the plasma volume and the average distance between unoccupied surface sites determines the chemisorption probability in this case. One common scenario is the adsorption of atomic hydrogen on a hydrogen-terminated silicon surface [19].

Depending on the specific reactions that occur while a species is adsorbed at the surface, growth or etching of material can be observed [20]. If, e.g. in the case of amorphous hydrogenated silicon (a-Si:H) deposition, a SiH_3 fragment adsorbs at the surface, it may react with other nearby SiH_x molecules forming H_2 which then desorbs. When a large enough number of hydrogen molecules is formed, the silicon atom remains bound to the surface and film formation is observed. Similarly, an etching compound such as atomic hydrogen can adsorb at the surface, react with a SiH_3 molecule to form volatile SiH_4 which then desorbs [21]. Macroscopically, this results in the etching of the silicon film and is sometimes also referred to as chemical sputtering.

2.3.2 Surface reaction mechanisms

While more complex interactions are possible, the main relevant surface reactions are those, where exactly two species meet at the surface. These can be fundamentally divided into two categories based on the thermal state of the incoming species prior to the reaction: the Langmuir-Hinshelwood (L-H) process and the Eley-Rideal (E-R) process [16, 22]. In both processes, two incoming species A and B react at the surface to form a molecule AB which then desorbs.

In the Langmuir-Hinshelwood process, both A and B first adsorb at the surface and thermalise prior to reacting with each other. This leads to the reaction obeying second-order kinetics, i.e. the reaction rate being proportional to the surface coverage Θ_A and Θ_B of the two species. As both species are thermalised before the reaction, the leaving molecule AB has a kinetic energy matching the surface temperature. The reaction with surface sites S can be described as following:

$$\begin{aligned} A_{(g)} + S_{(s)} &\rightleftharpoons AS_{(s)}\,, \\ B_{(g)} + S_{(s)} &\rightleftharpoons BS_{(s)}\,, \\ AS_{(s)} + BS_{(s)} &\longrightarrow AB_{(g)} + 2\,S_{(s)}\,. \end{aligned} \tag{2.15}$$

The Eley-Rideal process describes a situation, where A directly reacts with B without adsorbing first. This leads to the reaction primarily obeying first-order kinetics in A, i.e. being proportional to the flux of incoming species A, with a more complex dependency on the surface coverage Θ_B. As the incoming species does not thermalise prior to the reaction, the desorbing product AB carries part of that kinetic energy and is itself not thermalised. In general, this reaction has a significantly smaller cross section than the L-H process, as the incoming species needs to break the chemical bond of B with the surface in time scales of molecular vibrations compared to the much larger interaction times at the surface in the L-H

process. Furthermore, as the incoming species carries significant momentum, the resulting reaction cross sections are dependent on the specific isotope, especially in the case of hydrogen and deuterium abstraction at a surface. Here, the reaction with a surface site S can be described as following:

$$\begin{aligned} \mathrm{B_{(g)} + S_{(s)} &\rightleftharpoons BS_{(s)}\,,} \\ \mathrm{A_{(g)} + BS_{(s)} &\longrightarrow AB_{(g)} + S_{(s)}\,.} \end{aligned} \tag{2.16}$$

Due to the flux of ions from the plasma, ion bombardment can play an additional role depending on the electric potential of the substrate. Energetic ions impacting the surface lead to the physical sputtering of material and can create defects if the momentum of the incoming ion overcomes the surface binding energy of the substrate. For a-Si:H films, this is typically not desirable as the defects act as recombination centres that hinder the transport of electrons [16]. On the other hand, for amorphous hydrogenated carbon (a-C:H) films, the subplantation of energetic ions with energies above 90 eV leads to the formation of a diamond-like structure [23, 24]. These effects do not play a significant role for nanoparticles positioned in the plasma bulk with floating potentials of only a few volts.

2.3.3 Selective heating and crystallisation

One inherent effect of non-thermal plasmas on very small particles is selective heating. Due to their small heat capacitance, a single heating event can increase the temperature of a small particle in the range of nanometres by several hundred Kelvin above the gas temperature for very short durations [25, 26]. This makes non-thermal plasma treatment ideal for the annealing of group IV and III-V semiconductors to obtain nanocrystals.

Experiments using a type of flow-through reactor using a capacitively coupled low pressure non-thermal plasma have shown the generation of silicon nanocrystals [27]. The crystallisation temperature of small silicon particles of sizes between 4–10 nm lies at 500–1000 °C, far above the measured gas temperature of only 150–250 °C. Yet, particles appear to have reached conditions for crystallisation.

Mangolini et al. [28] provide a possible explanation for a plasma-based heating mechanism backed by a self-consistent stochastic Monte-Carlo simulation. For the heat loss term, only heat conduction through neutral collisions with the background argon gas is considered, as radiative effects are significantly slower than conduction. Furthermore, it is assumed that the particle temperature equilibrates instantly, as solid state heat transfer happens on much shorter time scales than all other involved heat transfer processes.

The heat generation happens through collisions with ions, where a collision with an argon ion leads to recombination on the particle surface, releasing energy equal to the ionisation potential of argon of 15.76 eV. Collisions with atomic

hydrogen have multiple pathways. If the collision surface site is a dangling bond, the hydrogen ion has a 100 % probability of binding to the site, releasing the binding energy of an Si−H bond of 3.1 eV. On a hydrogen-terminated surface site, there is an 11 % probability of abstraction through the Eley-Rideal mechanism (see eq. (2.16)) releasing an energy of 1.41 eV. The remaining cases are physisorption of the hydrogen, which given enough time can diffuse to a dangling bond, reacting there for a release of 3.1 eV. Otherwise, it recombines with an incoming radical instead, releasing 4.51 eV. Finally, at high particle temperatures above 900 K, thermal desorption through the Langmuir-Hinshelwood mechanism (see eq. (2.15)) becomes relevant, leading to a loss of 1.69 eV through the removal of two hydrogen atoms from the surface.

Collisions with ions and electrons also lead to changes in the particle charge, which in turn changes the collision rates calculated using the OML model (cf. section 2.2.1). The changes in particle charge are tracked over the collision events.

The simulations show that the average particle temperature stays constant at about 400 K for all particle sizes. On the other hand, the instantaneous particle temperatures become increasingly unsteady for smaller particle sizes with momentary temperatures reaching 1000–1100 K for a 2 nm particle, due to its small heat capacitance. The authors introduce the particle temperature density function (PTDF) as the fraction of time the particle spends above a given temperature and show that it becomes wider for smaller particle sizes.

Finally, the effect of an increasing particle density is investigated, where the Havnes effect (see section 2.2.1) limits the available particle charge as a significant portion of the available electrons are located on the nanoparticles. The authors show that the width of the PTDF as well as the average particle temperature drops to about half when increasing the particle density from $10^{15}\,\mathrm{m}^{-3}$ to $3 \cdot 10^{16}\,\mathrm{m}^{-3}$, while the Havnes parameter increases from about 0.1 to 2.

2.3.4 Surface passivation and functionalisation

The classic way of treating the surface of nanoparticles is liquid-phase functionalisation [29–34]. In this process, nanoparticles are either created or dissolved in a colloidal solution where they then react with various substances to create a passivation or functionalisation of the particle's surface. There is a large body of work regarding the treatment of silicon nanocrystals as the goal of creating silicon-based photonic applications has attracted a lot of research on this topic.

A 1 nm oxide shell can already increase photoluminescence of silicon nanocrystals [35, 36]. Using organic capping of the silicon surface can further increase photoluminescence significantly in porous silicon [30, 31] and free-standing silicon nanocrystals in colloidal solution [32–34]. These methods are based on the hydrosilylation of the Si−H surface bonds to create a Si−C covalent bond. While they can achieve nanocrystals with excellent optical properties, this method presents a

number of drawbacks. The liquid-phase hydrosilylation reactions are slow with reactions taking several hours and requiring precise conditions in nitrogen-purged, oxygen-free, heated systems. As the boiling points of precursors become lower with shorter organic chains, the viable reaction temperatures decrease, in turn increasing reaction times even further. Additionally, solvent and organic precursor need to overcome the van der Waals forces that hold particles together in agglomerates for reactions to occur, which limits the ability to use shorter organic chains as well. In-flight aerosol-based processing presents a much faster processing alternative and has a larger range of usable precursors [37]. Yet, these methods require high-temperature furnaces for the thermal aerosol-phase reactions and have problems due to particle agglomeration.

Plasma-based techniques overcome all of these drawbacks. Oxygen impurities can be eliminated by using systems capable of ultra-high vacuum conditions. Agglomeration is inherently suppressed by the charging and resulting repulsive Coulomb forces of particles in dusty plasma systems. Plasmas also provide the necessary energy to overcome thermal activation barriers and the presence of excited species can further aid the functionalisation process.

Mangolini et al. [38] have performed plasma grafting of silicon nanocrystals resulting in organically functionalised surfaces with a wide range of organic compounds. They used a two-stage setup, where particles are first synthesised in a flow-through plasma reactor and then treated in a secondary continuous flow reactor operated at very low power (10–15 W), where organic compounds are added through a bubbler system. Fourier-transform infrared spectroscopy (FTIR) of particles treated with 1-dodecene shows excellent results comparable to liquid-phase functionalisation, but achieved in less than 1 s of residence time in the treatment plasma compared to several hours using liquid-phase chemistry. The authors have also successfully grafted a wide variety of compounds on the particle surface ranging from long chained 1-dodecene ($H_3C{-}(CH_2)_9{-}CH{=}CH_2$) to very short ethylene-glycol ($HO{-}CH_2{-}CH_2{-}OH$), which usually is inaccessible via liquid-phase chemistry.

2.4 Nanoparticles

Shrinking dimensions from the micro to the nanoscale brings about fundamental changes in material properties which have enabled discoveries and applications in microelectronics, photonics, photovoltaics, biotechnology, and many other fields [39]. This section centres on different aspects of nanoparticles, starting with the quantum effects of silicon when reducing its dimensions to the nanoscale as an example of a group IV semiconductor. Afterwards, synthesis options for carbon and silicon nanoparticles from reactive gasses in a low pressure non-thermal plasma discharge are presented. A different approach is used for noble metal nanoparticles, which can be created in a gas aggregation source (GAS).

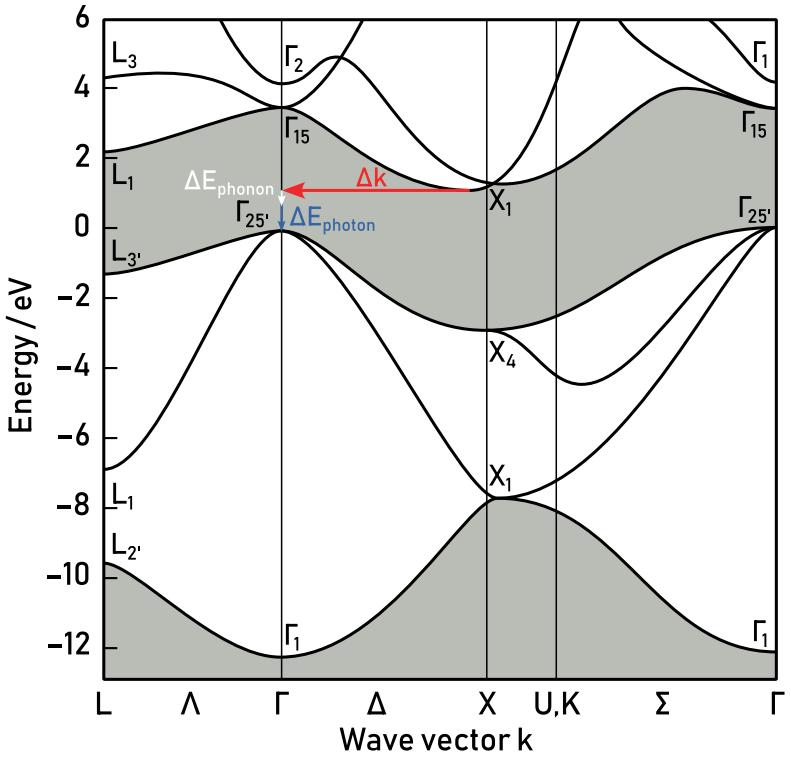

Figure 2.5: Theoretical band structure for bulk silicon from an energy-dependent nonlocal-pseudopotential calculation [40]. The electronic transition across the band gap between the conductive band above and the valence band below (with forbidden regions marked in grey) is only possible in a three body process between an electron, a hole, and a phonon to mediate the necessary change in wave vector Δk (red). The phonon receives an energy of ΔE_{phonon} (white) with the remaining energy being released in the form of a photon with energy ΔE_{photon} (blue). Adapted from [40].

2.4.1 From bulk silicon to quantum dots

While bulk silicon is the main material used for microelectronics today, its band structure does not lend itself well for photonic applications. The recombination of an electron in the lowest unoccupied molecular orbital (LUMO) near the X point with a hole in the highest occupied molecular orbital (HOMO) at the Γ point necessitates a significant change Δk in wave vector (see fig. 2.5). To cross this indirect band gap in an electronic transition a three body process between an electron, a hole, and a phonon mediating the wave vector change is needed. Such a process has a very low collision rate leading to long radiative lifetimes, which are competing against non-radiative processes.

The luminescence efficiency η is determined by the comparison of radiative processes with non-radiative ones:

$$\eta = \frac{\tau_{\text{nr}}}{\tau_{\text{r}} + \tau_{\text{nr}}}, \tag{2.17}$$

where $\tau_{\text{r,nr}}$ are the lifetimes of radiative and non-radiative processes respectively. There are various relevant non-radiative processes for silicon semiconductors:

Shockley-Read-Hall recombination occurs at a defect or impurity site, which represents a trap for electrons (and/or holes) creating a localised state [41, 42]. Electrons and holes can recombine at such a site with the transition energy being emitted in the form of a phonon. Auger recombination is the electron-hole recombination transferring the energy and momentum change onto another electron and/or hole [43]. Especially for nanoparticles, surface mediated recombinations can also play a significant role. The rates of all these processes are dependent on a number of factors like the quality of the surface passivation or doping / impurity concentrations of the silicon material. Typical non-radiative lifetimes are in the order of microseconds or lower, several orders of magnitude faster than the radiative lifetimes of the indirect band gap transition with a lifetime of milliseconds, compared to typical direct band gap semiconductors with lifetimes in the order of nanoseconds. This leads to bulk silicon having a very low quantum efficiency for photonic applications.

These properties change drastically when restricting the physical dimensions of the semiconductor from three to lower dimensions in the form of 2-d thin films, 1-d nanowires or 0-d quantum dots [44]. The relevant size parameter is the exciton Bohr radius, i.e. the physical separation of the electron and hole comprising the exciton, which for silicon is about 5 nm. When the dimensions of the semiconductor are in the order of the exciton Bohr radius or smaller, quantum confinement effects start playing a role and increase the overlap of electrons and holes in k-space. This decreases radiative recombination times significantly, leading to a 3 to 4 orders of magnitude higher luminescence efficiency, which has made silicon nanocrystals the subject of very intensive studies [45–48].

Another property of nanocrystals is their large surface-to-volume ratio. A 2 nm icosahedral silicon nanocrystal contains about 280 Si atoms, 120 of which (43 %) are making up its surface [49]. With these immense surface-to-volume ratios, the properties of nanocrystals depend strongly on their surface functionalisation. While the specific mechanisms of photoluminescence of silicon nanocrystals are the topic of ongoing research, clear differences between surface functionalisations can be observed. For example, while the physical dimensions of a nanocrystal tend to increase the band gap from 1.12 eV in bulk silicon to higher values, the increase is limited to about 1.6 eV for O-terminated silicon nanocrystals. For a H-termination on the other hand, this can be extended to about 2.2 eV [50–52]. Furthermore, functionalising the surface with compounds containing carbon-carbon double or triple bonds can strongly inhibit photoluminescence efficiency, with aromatic compounds even completely quenching the emission [30, 53]. Precise control over the surface quality of nanoparticles is key for their optical application.

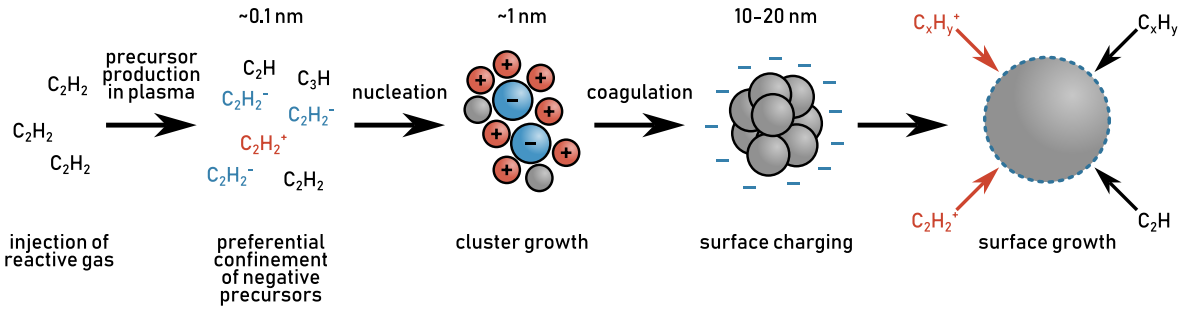

Figure 2.6: Sketch of the particle growth process in a reactive plasma using the example of acetylene to form a-C:H nanoparticles. Particle formation happens in three distinct stages: nucleation from precursors, coagulation, and surface growth. Adapted from [54].

2.4.2 Synthesis of carbon and silicon nanoparticles from reactive gasses

The synthesis of nanoparticles can fundamentally be classified into two categories: the top-down and the bottom-up approach [45]. In the top-down approach, bulk material is processed to create nanoparticles. One such widely used method is the wet chemical etching of crystalline silicon wafers in hydrofluoric acid to create porous silicon. This can yield various nanomaterials such as nanowires or nanocrystals, depending on the subsequent processing steps.

While this approach can yield nanoparticles of excellent quality and narrowly defined size distributions, the bottom-up approach scales up more easily towards higher production rates. Here, particles are build from precursors via liquid or gas phase chemical routes. These approaches provide fine control over the resulting particles and modifications such as doping are easily performed. Plasma synthesis offers a significant improvement over the classical gas phase options by particles accumulating negative charge in the plasma and therefore suppressing agglomeration of particles. Furthermore, the plasma chemistry allows for a variety of physical and chemical processes to occur that would otherwise need significantly higher temperatures.

Particles are generated in a reactive plasma in three three distinct phases [55]: Nucleation, coagulation, and accretion (see fig. 2.6). The process of nucleation can be abstractly described in two steps following Yasuda and Hsu [56]: *initiation* where reactive precursors are generated, and *propagation* where the precursors interact and form bigger molecules. The precursors can be ions of both positive or negative charge, excited molecules or free radicals, which in our typical plasma environment are primarily generated via electron impact reactions. Larger polymers are then formed in reactions of precursors either with each other or with other present molecules. The crucial part is that this product can then be initiated again and propagate further, leading to continuous growth in a repeated process.

The nucleation process creates clusters in the order of a few nanometres in

size, which are mainly neutral but in a plasma can undergo charge fluctuations to carry at most one positive or a few negative elementary charges depending on their size [57]. As confining forces in the plasma only apply to negative species, positively charged clusters are lost to the ion drag forces (see section 2.2.2) and neutral clusters slowly diffuse out of the plasma volume. Furthermore at this size, the previous growth mechanisms become less effective [58], leading to slower growth of the clusters from this point onwards.

Where previous models suggested a critical cluster density to enter the coagulation phase [54, 55], more recent investigations suggest that nucleation does not stop, but continues in dust-free regions [59]. The particle size distribution becomes bimodal as two species emerge [60, 61]: 1. large particles that have grown to sizes between 10–20 nm and carry several negative elementary charges, and 2. freshly generated clusters up to 2 nm from nucleation in the dust-free region. Here, coagulation becomes the dominant growth process, as large negative particles attract both the positively charged clusters and the more abundant neutral clusters through an enhancing effect of induced image potentials [61]. The now quickly growing particles start accumulating more charge and spread through stronger ion drag forces, quenching the nucleation in the discharge and stopping this process.

At this point, the particles have a size of about hundred nanometres and we enter the accretion phase. Surface growth becomes the dominant process as the generated ions and neutrals (mainly radicals) attach to the particle's surface. This phase is characterized by linear growth of the particle radius, which can be derived assuming only neutral radicals contribute to the growth. In this case, the acquired mass per unit of time is proportional to the radical density n_r and the particle's surface area $4\pi r^2$ [55]:

$$\frac{\mathrm{d}m}{\mathrm{d}t} \propto n_\mathrm{r} r^2 \,, \tag{2.18}$$

$$\frac{\mathrm{d}m}{\mathrm{d}t} = \rho \frac{\mathrm{d}V}{\mathrm{d}t} = \rho \frac{4\pi}{3} \frac{\mathrm{d}(r^3)}{\mathrm{d}t} = 4\pi r^2 \rho \frac{\mathrm{d}r}{\mathrm{d}t} \,, \tag{2.19}$$

$$\Rightarrow \frac{\mathrm{d}r}{\mathrm{d}t} \propto \frac{n_\mathrm{r}}{4\pi\rho} \,, \tag{2.20}$$

showing the linear growth of the particle's radius.

Finally, the reaction rates are dependent on the gas temperature. Temperatures between 250–500 K show a variation of dust production of over an order of magnitude, as many of the involved reactions are temperature dependent for silane, methane, and acetylene plasmas. This effect was used to delay or speed up the onset of particle formation in silane [58, 62–64], acetylene [65] and methane plasmas [66].

Carbon nanoparticles

Based on their original technological application in etching plasmas for microelectronic devices, some of the most thorough investigations of plasmas creating carbon nanoparticles are discharges operated using fluorocarbons like CF_4 or C_2F_6. A different commonly used class are hydrocarbons, which see a wide range of applications in plasma enhanced chemical vapour deposition (PECVD) systems using gases like methane (CH_4) or acetylene (C_2H_2). Both are producing a variety of precursors that lead to particle formation in a plasma environment but show significant differences especially during nucleation. Acetylene plasmas lead to fast polymerisation under a wide range of parameters, whereas methane and similar hydrocarbons either fail to generate dust at all or need specific circumstances for initiation.

Investigations using mass spectrometry and FTIR [67, 68], as well as chemical kinetic simulations [69–71] have lead to a deeper understanding of the main reaction pathways of particle growth [72]. For acetylene, as the C≡C triple bond has a high dissociation threshold, typically even carbon numbers in $C_{2n}H_m$ are seen as products during nucleation. The modelling of De Bleecker et al. [70] presents three main pathways for polymerisation: 1. the Winchester mechanism consisting of anion-acetylene collisions 2. the cation-acetylene reaction pathways, and 3. collisions of neutral acetylene with radicals.

As anions are confined by the electrostatic forces in the plasma environment, they play a large role in the plasma chemistry even as their generation rates through electron impact dissociative attachment are about three to four orders of magnitude lower than their cationic counterpart. The main reaction pathway for anions is called the Winchester mechanism and consists of a chain of polymerisation reactions involving ever larger $C_{2n}H^-$ anions:

$$\begin{aligned} C_2H^- + C_2H_2 &\longrightarrow C_4H^- + H_2\,, \\ C_4H^- + C_2H_2 &\longrightarrow C_6H^- + H_2\,, \\ &\vdots \\ C_{2n}H^- + C_2H_2 &\longrightarrow C_{2n+2}H^- + H_2\,. \end{aligned} \tag{2.21}$$

In this reaction, acetylene is continuously appended to the end of the chain releasing a hydrogen molecule. This generates almost pure carbon ions that are bound to only a single hydrogen atom. This reaction keeps the triple bond of the acetylene molecule intact, creating an ever longer chain of alternating single and triple bonds between the carbon atoms.

A second pathway consists of cation-acetylene reactions mainly starting with $C_2H_2^+$ ions present in the discharge. At each step acetylene is added to the ion in a condensation reaction, sometimes releasing a hydrogen molecule depending on

the number of carbon atoms and specific stability of the intermediate product:

$$\begin{aligned} C_2H_2^+ + C_2H_2 &\longrightarrow C_4H_2^+ + H_2\,, \\ C_4H_2^+ + C_2H_2 &\longrightarrow C_6H_4^+\,, \\ C_6H_4^+ + C_2H_2 &\longrightarrow C_8H_6^+\,, \\ C_8H_4^+ + C_2H_2 &\longrightarrow C_{10}H_6^+ + H_2\,. \\ &\vdots \end{aligned} \tag{2.22}$$

This creates carbon clusters with much larger hydrogen content than in the Winchester mechanism.

Finally, there are neutral collisions with ethynyl (C_2H) radicals that are created through dissociation of acetylene. The ethynyl radical is a very reactive intermediate product and is part of a polymerisation process through continuous insertion into ever larger clusters:

$$\begin{aligned} C_2H + C_2H_2 &\longrightarrow C_4H_2 + H\,, \\ C_2H + C_4H_2 &\longrightarrow C_6H_2 + H\,, \\ &\vdots \\ C_2H + C_{2n}H_2 &\longrightarrow C_{2n+2}H_2 + H\,. \end{aligned} \tag{2.23}$$

This pathway create chains of alternating single and triple bonds with a very low hydrogen content similar to the Winchester reaction. At later stages, the cluster itself can become a $C_{2n}H$ radical through electron induced dissociation. Furthermore, insertion of atomic hydrogen can lead to the formation of $C_{2n}H_3$ radicals and higher.

Silicon nanoparticles

Silicon nanoparticles can be synthesised in a low-temperature plasma similar to carbon particles using silicon-containing molecules as precursors. The simplest form is silane (SiH_4) which unlike its carbon equivalent methane is already very reactive in a plasma environment and can initiate particle generation on its own.

The reaction kinetics of silicon nucleation are fundamentally different than those of carbon molecules. While carbon exhibits relevant cation reactions even at higher cluster sizes, the silane has a "kinetic bottleneck" at $Si_3H_7^+$ preventing the formation of larger cation clusters [70, 73–75]. The main pathway in silane discharges are anion-silane collisions, where both silyl ($Si_nH_{2n+1}^-$) and silylene ($Si_nH_{2n}^-$) anions undergo chain reactions forming ever larger clusters:

$$Si_nH_{2n+1}^- + SiH_4 \longrightarrow Si_{n+1}H_{2n+3}^- + H_2\,, \tag{2.24}$$

$$Si_nH_{2n}^- + SiH_4 \longrightarrow Si_{n+1}H_{2n+2}^- + H_2\,. \tag{2.25}$$

The enthalpies of these reactions are around thermoneutral ranging from -0.07 to $0.07\,\mathrm{eV}$ [58]. The slightly endothermic reactions present an energy barrier that would make the process unfavourable. Numerical simulations by De

Bleecker et al. [74] take vibrationally excited silane molecules into account besides ground state molecules, ions, and radicals, as they play a vital role in the initial stages of particle formation. The vibrational excitation brings in the necessary internal energy to overcome the energy barrier. Furthermore, the dissociative attachment reactions into silyl ($SiH_4^* + e^- \longrightarrow SiH_3^- + H$) and silylene ($SiH_4^* + e^- \longrightarrow SiH_2^- + 2\,H$) are the main reaction pathway for creating the silyl and silylene, which start the anion-silane chain reactions. The reaction cross sections of these reactions are an order of magnitude larger for vibrationally excited silane than for their corresponding ground state species. Finally, the vibrational excitation of silane also presents a major source of energy loss for electrons in electron-silane collisions that needs to be taken into account.

Comparing the two anion-silane pathways, the simulations [74] show that 90 % of particle formation occurs through the silyl pathway and the silylene pathway comprises only the remaining 10 %. A further pathway are collisions between anions and SiH_3 radicals, which can have a significant impact on the formation of dust particles. Simulations grouping up both silyl and silylene clusters into a single species and including SiH_m^- radicals have shown an increase of a factor of 1.8 in dust formation compared to simulations ignoring radicals.

The impact of anion reactions with SiH_3 radicals and excited SiH_4^* species depends on the rate constant of the reaction between anions and ground state SiH_4, which is not well known. De Bleecker et al. [74] have shown that the relative contribution of the different reactions varies strongly and can be between 40 % ground state, 35 % excited state, and 25 % radical reactions at the lowest examined reaction rate to an almost completely ground state dominated reaction at the highest reaction rate. The authors conclude that as the general consensus in the literature indicates an importance of vibrationally excited species, the reaction rate is more likely to be located towards the lower bound.

2.4.3 Synthesis of noble metal nanoparticles through gas aggregation

Following the initial work by Haberland et al. [76], the GAS has become a staple for the generation of nanoparticles. The most common setup consists of a planar direct current (DC) magnetron source with a metal target from which sputtered material is carried away into the condensation zone using a laminar inert gas flow [77].

There are two requirements for the condensation of this supersaturated metal vapour: low temperature and condensation germs. The cooling is provided by a comparatively high background gas pressure of several tens to a few hundred Pa. Furthermore, ions and charged clusters formed in the magnetron discharge pose very effective condensation germs because of their r^{-4} polarisation interaction between an ion and a neutral particle compared to the van der Waals forces with r^{-6} between two neutral particles [77]. Magnetron discharges also tend to

produce a higher number of dimers, which helps to overcome the higher energy barrier of the initial stages of nucleation [78]. The residence time in this condensation zone defines the final particle size and can lead to a variety of size distributions depending on the geometry of the particular setup. Nearly monodisperse size distributions with full-width half-maximums of 20 % are possible, but other configurations producing producing multi-peaked size distributions have been reported [77, 79, 80].

While the main use case of a GAS is the generation of metal nanoparticles, changing the target composition allows for the generation of nanoparticles of a wide range of materials such as different metals, alloys, inorganic compounds, and even polymers [81]. The localisation of sputtering, which happens primarily on the so-called *racetrack* due to the magnetic field configuration, can be used to create alloy nanoparticles with tunable composition [82]. By placing Au wires in the racetrack of an Ag target, Drewes et al. [82] were able to tune the Au/Ag ratio of the resulting nanoparticles by varying the used gas pressure, which determines the width of the erosion zone. Further effects from material redeposition on the target need to be taken into account to reliably recreate the desired particle composition.

2.5 In situ and ex situ diagnostics of nanoparticles

This section presents the fundamental principles behind the diagnostics used in this work: Fourier-transform infrared spectroscopy (FTIR) for the analysis of the chemical composition of the nanoparticles, localised surface plasmon resonance for the sensitive measurement of changes to the particle's surface, and electron microscopy for the ex situ imaging. The technical details on absorption spectroscopy and its data analysis follow in section 3.1.

2.5.1 Fourier-transform infrared spectroscopy

Explanations in this section follow scientific textbooks on infrared spectroscopy such as [83–85].

Working principle

While the term Fourier-transform infrared spectroscopy (FTIR) simply refers to one specific method of measuring infrared spectra, it has become synonymous with the act of measuring an infrared spectrum itself and one can find many references to "FTIR spectra" throughout the scientific literature. It is an indicator for the incredible improvement that FTIR spectrometers represented over the traditional grating monochromators, being able to scan a large range of wavenumbers in the same time it previously took to measure one small slice of it.

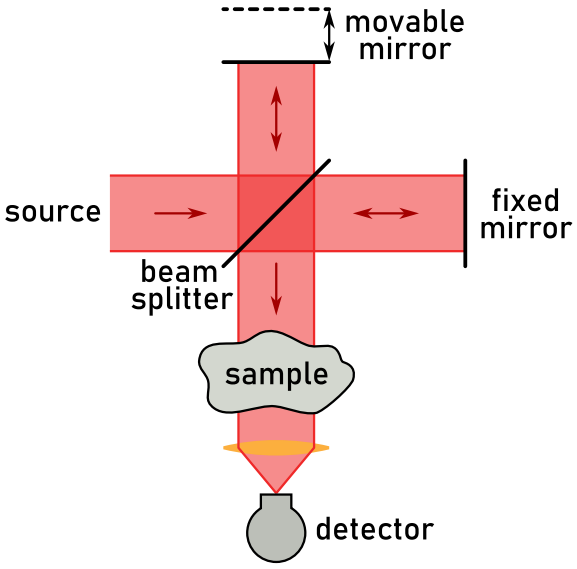

Figure 2.7: Sketch of a Michelson two-beam interferometer setup, where the light from a source is split into two paths. One path leads to a fixed mirror, while the other hits a movable mirror. After recombination, the light is passed through the sample and then measured with a detector.

This is achieved by using a two-beam interferometer setup similar to the well-known Michelson-Morley experiment where a beam is split into two paths using a beam splitter as depicted in fig. 2.7. One of these paths leads to a fixed mirror, while the other hits a movable mirror, with both mirrors reflecting the beam back onto the beam splitter. Whereas in holography the object to be studied would be put into one of these beam paths to record its impact on the wave fronts, with FTIR, the sample is placed after the recombination of both beam paths. The resulting recombined beam is finally measured using a detector. In this way, the interferometer acts as a special sort of wavelength filter, where the interference between the two beams creates different spectral patterns depending on the position of the movable mirror. This process encodes the spectral information of the sample as a function of the mirror position.

A typical interferogram obtained by this method is shown in fig. 2.8a. When both mirrors are placed in the same distance from the beam splitter, all wavelengths interfere constructively leading to the formation of the so-called centre burst. A displacement of the movable mirror by a distance $\Delta/2$ leads to a beam path length difference of Δ and therefore to constructive interference for all wavelengths that fulfil $\Delta = n\lambda$ for positive integers n. As half of the initial intensity $I_0(\lambda)$ passes directly through the beam splitter, the complete interference record $I(\Delta, \lambda)$ measured after the beam splitter is given by:

$$I(\Delta, \lambda) = \frac{1}{2} I_0(\lambda) \left[1 + \cos\left(2\pi \frac{\Delta}{\lambda} \right) \right] . \tag{2.26}$$

The term interferogram refers specifically to the cosine term in eq. (2.26).

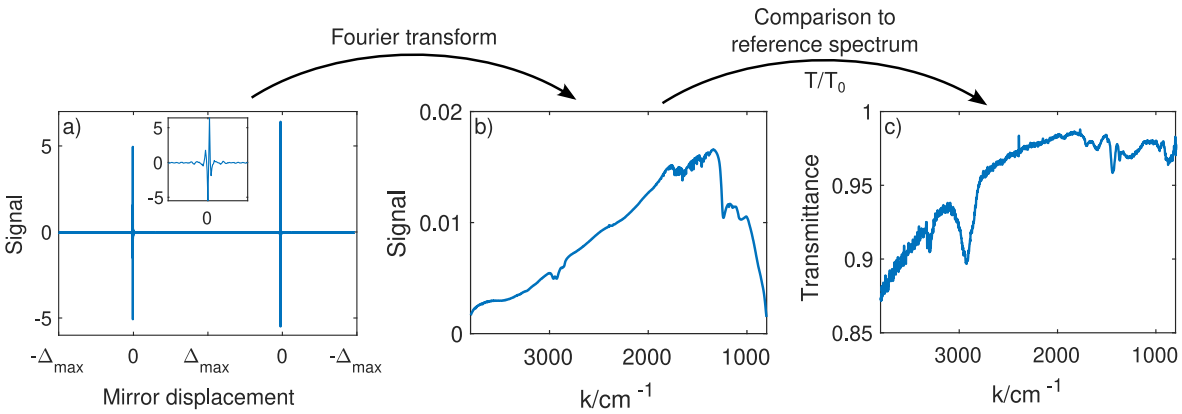

Figure 2.8: Processing steps of a measured interferogram. a) Bi-directional interferogram showing two centre bursts at the zero path difference crossings. The interferogram is measured both in forward and backward direction. A small interval around $\Delta = 0$ is shown as an inset. b) Fourier transform of the interferogram giving the sample spectrum. c) The ratio of sample and reference spectrum gives the transmission spectrum.

Applying a Fourier transform to the interferogram yields:

$$S(\nu) = \mathcal{F}\left\{\cos\left(2\pi\frac{\Delta}{\lambda}\right)\right\} = \frac{1}{2}\left[\delta\left(\nu - \frac{1}{\lambda}\right) + \delta\left(\nu + \frac{1}{\lambda}\right)\right] . \tag{2.27}$$

The various wavelengths of light and their respective differently spaced intensity patterns have now been separated into their spectral components resulting in the spectrum $S(\nu)$. The mathematical operation of a Fourier transform involves an integral from $\Delta = 0$ to $+\infty$ and works on the continuous function $I(\Delta)$. In practice, the available movement range of the mirror is finite and the function $I(\Delta)$ is measured in discrete steps, which present the resolution and bandwidth limitations of this method.

Maybe counterintuitive at first glance, the limited range of the mirror defines not the bandwidth but rather the resolution of the spectrum. The implications of the Fourier transform are understood better, if one assumes the movement of the mirror to be linear (as is the case in many commercially available FTIR spectrometers) with a mirror velocity of V. The interferogram for a mirror displacement $\Delta = Vt$ can now be seen as a temporal signal rather than a spatial one. All effects known from the spectral analysis of temporal signals do apply in this case, e.g. the spectral resolution is being defined by the length of the sample. Similarly, the temporal resolution of the signal determines the bandwidth of the spectrum according to the Nyquist theorem.

When using the rapid scan functionality of the Bruker VERTEX 80v as described in section 3.1, the mirror is moved at relatively high speeds. Here, the maximum sampling rate of the analogue-to-digital converter limits the available bandwidth to about $4000\,\mathrm{cm}^{-1}$. Any spectral components above this wavenumber will undergo aliasing, i.e. the spectrum will be folded back into the available

bandwidth. This is avoided by using an optical long wave pass filter which cuts off all spectral components above the Nyquist limit.

Overall, the application of the Fourier transform brings two big advantages over traditional grating spectrometers called the multiplex (or Fellgett's) and throughput (or Jacquinot) advantages. This also applies for other methods such as Fourier-transform nuclear magnetic resonance (FT-NMR) compared to its predecessor of the continuous-wave nuclear magnetic resonance spectroscopy (NMR). The multiplex advantage describes the fact that measuring the entire spectrum at once leads to a higher signal-to-noise ratio compared to a grating spectrometer at the same parameters (resolution, integration time, optical throughput, etc.). This advantage scales with the square root of the number of resolution elements in the spectrum. Typical measurements performed in this thesis use a spectral range of 0–4000 cm^{-1} with a resolution of 2 cm^{-1} and take about 15 s. To reach the same signal-to-noise ratio on a grating spectrometer, the measurement time would need to be increased by a factor of $2000 = 4000\,\mathrm{cm}^{-1}/2\,\mathrm{cm}^{-1}$ to over 8 h.

An FTIR spectrometers throughput is limited only by the effective area of the interferometer mirrors, whereas a grating spectrometer uses a small slit to create its spectral resolution. The throughput advantage of FTIR over grating spectrometers scales with ν^2, giving a factor of about 10–30 for 0–1000 cm^{-1} and about 150–250 for 3000–4000 cm^{-1} for the typical gratings used in infrared spectrometers.

While these advantages are significant in the infrared range and have led to FTIR spectrometers being the go-to solution for infrared spectroscopy, these types of two-beam interferometers see little use in the optical and ultraviolet range. The underlying reason is the effect of shot noise, which describes the effect of discretisation of the energy flux into single photons and scales with the square root of the incident radiation power. This exactly counteracts the multiplex advantage, where increasing the number of resolution elements is equivalent to splitting up the incident power into increasingly smaller parts. The only remaining advantage of two-beam interferometers in shot-noise limited situations is the absolute wavenumber precision given by the usage of a reference laser to determine the mirror position.

Vibrational transitions of molecules

The absorptions visible in infrared spectra are the result of vibrational transitions of molecules. In a molecule with N atoms, each atom has $3N$ degrees of freedom by translating in any of the three cartesian axes. The number of vibrational degrees of freedom is equal to $3N - 6$, subtracting the three translations and rotations of the entire molecule around the coordinate axes. For linear molecules, this number changes to $3N - 5$ as the rotation around the molecule axis does not displace any of its atoms. A diatomic molecule like CO therefore has one vibrational stretching mode, representing an oscillation of the bond length, whereas

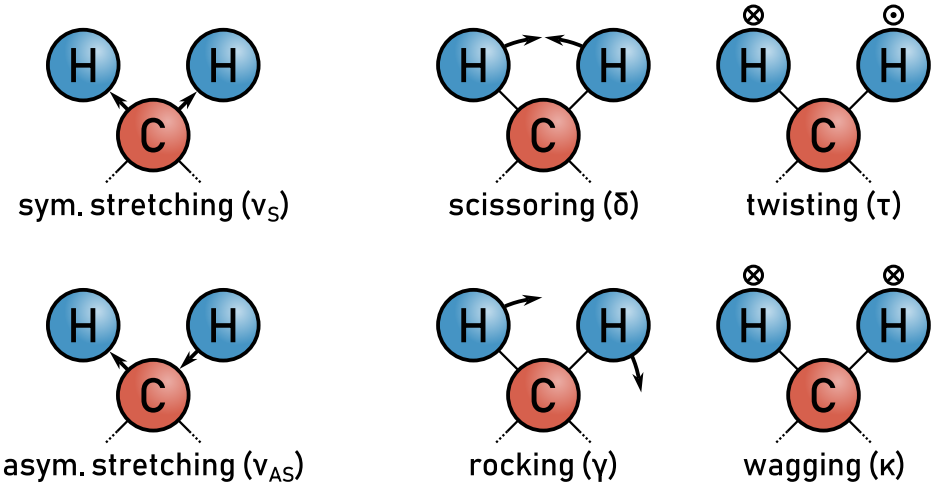

Figure 2.9: Different types of molecular vibrations shown on the example of a methylene group $-CH_2$. Vibrations can generally be differentiated into stretching modes (symmetric ν_S / asymmetric ν_{AS} depending on the phase of the separate oscillations) and deformation modes (scissoring δ / rocking γ, twisting τ / wagging κ) and are sometimes denoted by Greek letters in scientific literature.

tri-atomic molecules such as CO_2 or H_2O have three vibrational modes. For larger molecules, it is often sufficient to examine the vibration of a local group, e.g. a CH_x group in a longer hydrocarbon chain, as only a few atoms show strong displacements whereas the others stay mostly stationary. Vibrations are typically described using a set of six vibrational modes, which are further sub-divided into stretching and deformation modes as shown in fig. 2.9. Furthermore, so-called skeletal modes can be observed in larger molecules, which are large-scale oscillations of e.g. the carbon backbone of a large hydrocarbon. These are often found towards the far-infrared region $\leq 400\,\mathrm{cm}^{-1}$ but can also reach up to $1600\,\mathrm{cm}^{-1}$.

Vibrational potentials can often be adequately described with a simple harmonic oscillator and typically the strongest absorption lines in the infrared region correspond to a vibrational transition from the ground state to the first excited state. Vibrational excitations are only capable of absorbing infrared radiation if they result in a change in dipole moment. This results in symmetrical diatomic molecules such as O_2 or N_2 being completely infrared inactive and the absorption strength of the oscillations depending strongly on the specific molecule. As the absorption ratios between the different vibrational modes of the groups in a molecule are very characteristic for that particular arrangement, infrared spectra are often used by chemists to identify compounds and large reference works exist for the characterisation of organic compounds [83, 84, 86].

Transitions do not only occur between vibrational states, but can also simultaneously happen between different rotational states. These ro-vibrational transitions lead to the formation of a band structure, which can be very prominently seen in CO_2 and H_2O vapour present in ambient air (see fig. 2.10). While rotational transitions also occur in larger molecules, the separation between different

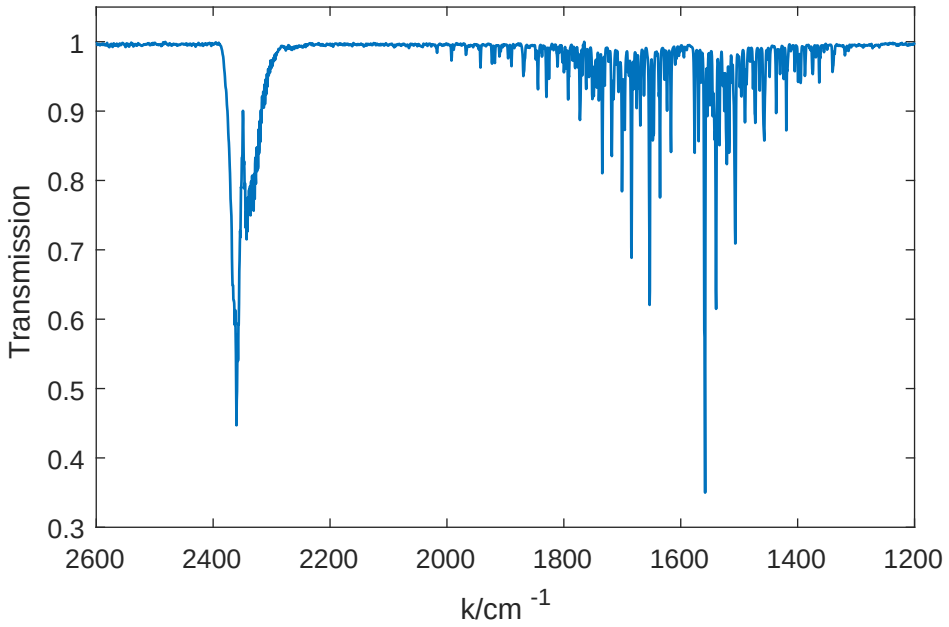

Figure 2.10: Transmission spectrum of ambient air. Ro-vibrational absorption bands can be seen from CO_2 (2290–2390 cm^{-1}) and H_2O (1300–2000 cm^{-1}).

rotational absorption lines is typically smaller than the resolution of the spectrometer.

Whereas the frequency of the different oscillations of organic molecules is readily found in reference works, their oscillator strengths are not so well documented. Many original sources are more than half a century old and specify values using various different definitions and units. Wexler (1967) [87] offers a solid reference work for hydrocarbons, which defines integrated absorption intensity in so-called "practical units"[2] in $L\,cm^{-2}\,mol^{-1}$ and gives typical conversions from other often found units. Using this definition, the measured integrated intensities can be converted into amount concentrations μ of a specific vibrational excitation mode, i.e., the bond concentration of that particular bond in the observed volume. The specific implementation of this conversion will be presented in section 3.1.2. In this system, the integrated intensity A is defined as the area underneath the curve of absorbance ϵ_ν over wavenumbers ν:

$$\begin{aligned} A &= \int \epsilon_\nu \, \mathrm{d}\nu \,, \\ &= \frac{1}{d} \int \log_{10} \frac{T_0}{T_i} \, \mathrm{d}\nu = B_i \mu \,, \end{aligned} \tag{2.28}$$

where d is the optical path length, T_0/T_i the ratio of incident intensity and transmitted intensity of a specific vibrational mode i, B_i the calibration factor for that vibrational mode in practical units, and μ the amount concentration (also called

[2]These were called "practical units" as they were a description of the integrated absorption intensity that only needed the maximum absorbance ϵ_{max} and the FWHM $\Delta\nu_{1/2}$ as described by Wexler, which were both particularly easy to determine manually from measurements at the time. While this is not a concern any more today, these units still provide a useful definition as a basis that other definitions in literature can be converted into.

molarity) in units of $\mathrm{mol\,L^{-1}}$. Other definitions can differ in a variety of ways for two main values: using the natural logarithm ln instead of the decadic logarithm $\log_{10}$ in the definition of the absorbance and specifying the vibrational frequency axis in frequencies $\mathrm{d}f$, logarithmic wavenumbers $\mathrm{d}\ln\nu$, or wavelengths $\mathrm{d}\lambda$ instead of wavenumbers $\mathrm{d}\nu$.

2.5.2 Localised surface plasmon resonance

This section aims to present the basic concepts and ideas behind localised surface plasmon resonance (LSPR) to provide an overview over the topic. More detailed descriptions can be found in scientific textbooks on the topic such as [88–90].

A surface plasmon is a dielectric eigenmode of a free electron gas at the boundary between two dielectrics. It is the solution of Maxwell's equations under the conditions that the electric field $\mathbf{E}$ is divergence-free and irrotational, i.e.

$$\begin{aligned} \nabla \cdot \mathbf{E} &= 0\,, \\ \nabla \times \mathbf{E} &= 0\,. \end{aligned} \tag{2.29}$$

As the electric field is the gradient of a potential ϕ, we arrive at the Laplace equation

$$\Delta\phi = 0\,. \tag{2.30}$$

The solution to this equation is a wave that is localized to the interface at $z = 0$ with

$$\phi(x,z,t) = \phi_0 \mathrm{e}^{-q|z|}\mathrm{e}^{\mathrm{i}(qx-\omega t)} \tag{2.31}$$

leading to electric field lines as shown in fig. 2.11 that are described by

$$\begin{aligned} E_\mathrm{x} &= q\phi_0 \mathrm{e}^{-q|z|}\cos(qx-\omega t)\,, \\ E_z &= -q\,\mathrm{sgn}(z)\phi_0 \mathrm{e}^{-q|z|}\sin(qx-\omega t)\,. \end{aligned} \tag{2.32}$$

The frequency of this wave can be determined by following the dielectric displacement $\mathbf{D} = \varepsilon_0\varepsilon_r^{(\pm)}(\omega)\mathbf{E}$ across the boundary between the dielectrics with the relative permittivity $\varepsilon_\mathrm{r}^{(\pm)}(\omega)$ in the positive and negative half space respectively. We define the boundary condition such that the normal component D_z must be continuous across the interface $z = 0$:

$$D_z = -\varepsilon_0\varepsilon_\mathrm{r}^{(-)}(\omega)\left.\frac{\partial\phi}{\partial z}\right|_{z\nearrow 0} \overset{!}{=} -\varepsilon_0\varepsilon_\mathrm{r}^{(+)}(\omega)\left.\frac{\partial\phi}{\partial z}\right|_{z\searrow 0}\,. \tag{2.33}$$

As the potential is at least C^1-continuous across the boundary, it follows that $\varepsilon_\mathrm{r}^{(-)}(\omega) = -\varepsilon_\mathrm{r}^{(+)}(\omega)$. For our typical case of the boundary of a particle in a vacuum, the permittivity of the positive half space equals unity and so the condition reduces to

$$\varepsilon_\mathrm{r}(\omega) \equiv \varepsilon_\mathrm{r}^{(-)}(\omega) = -1\,. \tag{2.34}$$

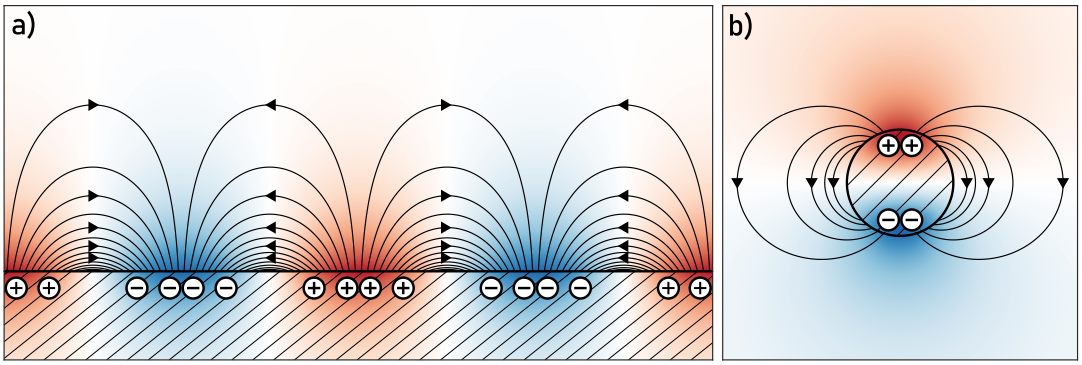

Figure 2.11: Sketch of a) a propagating surface plasmon on a metal-vacuum interface and b) a localised surface plasmon on a metallic nanoparticle. The metallic material is shown as a hatched area. The local electrostatic potential resulting from the surface charge is shown with red for positive and blue for negative values. The resulting electric displacement is shown as field lines. Note that there is no electric displacement field inside of the metal.

Inside the metal, the electric field induces a polarisation wave counteracting the electric field, i.e. $\mathbf{P}(z<0) = -\varepsilon_0\mathbf{E}$. Therefore, the induced charge distribution ρ_P can be obtained using eq. (2.32)

$$\begin{aligned}
\rho_\mathrm{P} &= -\nabla\cdot\mathbf{P} \\
&= \varepsilon_0\nabla\cdot\mathbf{E} \\
&= \varepsilon_0\left[-q^2\phi_0 \mathrm{e}^{-q|z|}\sin(qx-\omega t) - q\phi_0\sin(qx-\omega t)\frac{\partial}{\partial z}\left(\mathrm{sgn}(z)\cdot\mathrm{e}^{-q|z|}\right)\right] \\
&= 2\varepsilon_0 q\phi_0 \mathrm{e}^{-q|z|}\sin(qx-\omega t)\cdot\delta(z)\,. \qquad (2.35)
\end{aligned}$$

The charge distribution resembles a delta-function in z-direction, i.e. it represents a surface charge wave on the boundary between metal and vacuum.

The Drude model gives the dielectric function of a free electron gas in a metal as

$$\varepsilon(\omega) = 1 - \frac{\omega_\mathrm{p}^2}{\omega^2 + \mathrm{i}\varepsilon_0\omega\omega_\mathrm{p}^2/\sigma(\omega)}\,, \qquad (2.36)$$

where $\sigma(\omega)$ is the conductivity and ω_p the plasma frequency as described in section 2.1. Neglecting damping from a finite conductivity, i.e. $\sigma(\omega)=\infty$, and applying the permittivity constraint from eq. (2.34) results in the resonance frequency of the surface plasmon

$$\omega_\mathrm{s} = \frac{\omega_\mathrm{p}}{\sqrt{2}}\,. \qquad (2.37)$$

The theoretical considerations above were performed for the interface between a semi-infinite metal surface and vacuum. Under those circumstances, it is impossible for light to directly couple to surface plasmon excitations, as energy and momentum of the photon cannot be conserved simultaneously. The dispersion curves for bulk and surface plasmon as well as the light dispersion curve in vacuum are shown in fig. 2.12.

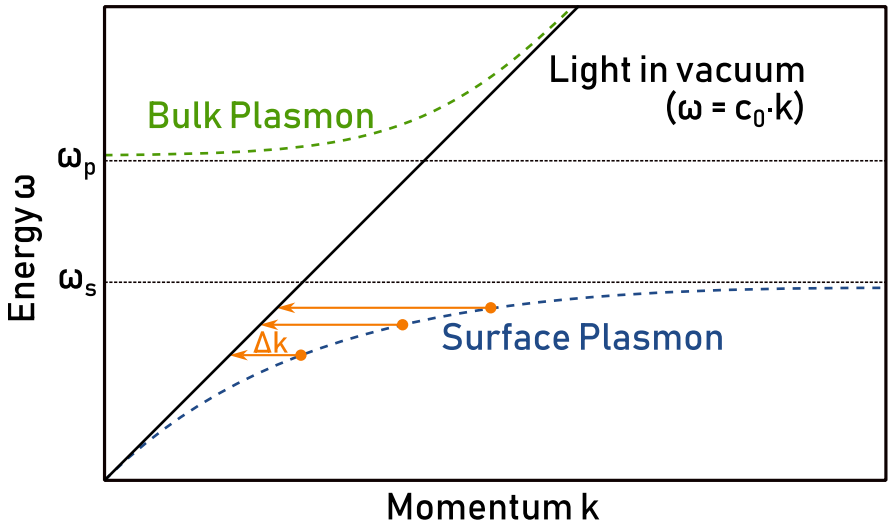

Figure 2.12: Dispersion relation curve for both bulk plasmons (green), surface plasmons (blue) and light in vacuum (black). Plasma frequency ω_p and surface plasmon resonance frequency ω_s are marked. Photons can normally not couple to surface plasmons because of a momentum mismatch. The small dimensions of the nanoparticle resemble a momentum provision Δk that can mediate and allow coupling between photons and localised surface plasmons. Adapted from [89].

In the metallic nanoparticles used in this work, the finite geometry of the nanoparticle allows localised excitation modes of the surface charge density. The limited extent of the particle with diameter d provides quantised amounts of momentum roughly approximated by $\Delta k \approx n\frac{2\pi}{d}$ depending on the order n of the localised surface plasmon mode [89]. This momentum provision allows coupling light directly to the LSPR.

These modes can also be understood as optical antenna resonances with the lowest mode representing a dipole excitation of the electrons in the particle. For the dipolar excitation mode of a spherical particle with radius a smaller than the incoming wavelength, the polarisability α is given by

$$\alpha = 4\pi\varepsilon_0 a^3 \frac{\varepsilon(\omega) - \varepsilon_{\text{med}}}{\varepsilon(\omega) + 2\varepsilon_{\text{med}}}, \tag{2.38}$$

where ε is the dielectric function of the particle and ε_{med} that of the surrounding medium. The LSPR is defined by the pole of α at $\varepsilon(\omega) + 2\varepsilon_{\text{med}} = 0$. For a particle in vacuum with $\varepsilon_{\text{med}} = 1$, and using the Drude model for a free electron gas given in eq. (2.36) the resonance frequency for the spherical dipolar surface plasmon follows as

$$\omega_{\text{res}} = \frac{\omega_p}{\sqrt{3}}. \tag{2.39}$$

Compare this to $\omega_s = \omega_p/\sqrt{2}$ obtained in eq. (2.37) for the resonance of a surface plasmon.

2.5.3 Electron microscopy

In the course of this work, both scanning electron microscopy (SEM) and transmission electron microscopy (TEM) measurements were performed on nanoparticle samples. Both methods image the sample by directing an electron beam onto it, but where SEM measures mainly secondary electron emission signals, TEM measures the primary transmitted electrons directly [91, 92]. The resolution limit of microscopy is given by the Abbe diffraction limit [93], which results in hundreds of nanometres for light in the optical range. For electron beams in the range of kV, the corresponding de Broglie wavelength is only a few Å, allowing a resolution in the sub-nanometre regime.

An SEM uses multiple stages of demagnification of an electron beam to create a spot on the sample with a diameter of 1–10 nm that is then scanned over the sample to create an image. Commercial SEM systems can measure multiple different signals, such as secondary electrons (SE), backscattered electrons (BSE), and energy-dispersive X-ray spectroscopy (EDX). The SE consists of secondary electrons with most probable exit energies of 2–5 eV and surveys the top few nanometres of the sample's surface. The BSE consists of scattered primary electrons with energies that can range from 50 eV to the energy of the original beam of up to 30 kV. The depth of the region probed by BSE is much deeper with 0.1–1 µm depending on the beam energy. With EDX, the electron beam stimulates the emission of characteristic X-rays from the sample at depths of 1–10 µm which allows determining its elemental composition.

The contrast of the resulting image for both SE and BSE depends on multiple factors, such as the surface topology and relative angle of incidence of the electron beam, mean atomic number of the target material, orientation of crystalline samples, and electrostatic and magnetic fields near the surface. For non-conductive samples such as carbon and silicon nanoparticles, charging effects can further lead to imaging artefacts. Often, a thin conductive coating is applied to eliminate this effect.

A conventional transmission electron microscopy (CTEM) uses an electron beam with higher energies of 100 keV to 1 MeV. Instead of focusing down to a single spot, a larger area of a thin sample is illuminated by the electron beam. The transmitted electron beam is then focused to create a magnified image of the sample on a screen or detector.

The scanning transmission electron microscopy (STEM) relates to the CTEM via the principle of reciprocity, which states that assuming elastic scattering the propagation of electrons is time-reversible. This means that the beam path of the CTEM can also be followed in reverse, i.e. replacing the original electron source with a detector and the original detector with an array of electron sources does not change the measured intensities. This is the foundational idea behind the STEM, where a single focused spot with a typical size of 50–200 pm is scanned over the sample to create a high resolution image of the sample. The STEM setup

can more easily fulfil the requirements of a perfectly coherent plane wave, giving a technical advantage over the conventional method. Special techniques such as high-angle annular dark-field (HAADF) imaging allow taking larger scattering angles into account to increase the contrast especially of materials with differences in their atomic number Z and allow the central transmitted beam to be used for simultaneous EDX measurements. Furthermore, electron diffraction methods such as selected area electron diffraction (SAED) can be used to determine the lattice-plane spacings in crystalline nanoparticles.

References

[1]D. A. Frank-Kamenetskii, *Plasma: The Fourth State of Matter* (Springer US, 1972), ISBN: 978-1-4684-1896-5.

[2]F. F. Chen, *Introduction to Plasma Physics and Controlled Fusion* (Springer US, 1984), ISBN: 978-1-4419-3201-3.

[3]M. A. Lieberman and A. J. Lichtenberg, *Principles of Plasma Discharges and Materials Processing*, 2nd ed. (John Wiley & Sons, Inc., 2005), ISBN: 978-0-471-72001-0.

[4]A. Piel, *Plasma Physics, An Introduction to Laboratory, Space, and Fusion Plasmas*, 2nd ed. (Springer International Publishing, 2017), ISBN: 978-3-31963425-8.

[5]A. Melzer, *Physics of Dusty Plasmas, An Introduction* (Springer International Publishing, 2019), p. 245, ISBN: 978-3-030-20259-0.

[6]C. K. Goertz and W.-H. Ip, "Limitation of electrostatic charging of dust particles in a plasma", Geophysical Research Letters **11**, 349–352 (1984).

[7]O. Havnes, T. K. Aanesen, and F. Melandsø, "On dust charges and plasma potentials in a dusty plasma with dust size distribution", Journal of Geophysical Research **95**, 6581 (1990).

[8]F. Greiner, A. Melzer, B. Tadsen, S. Groth, C. Killer, F. Kirchschlager, F. Wieben, I. Pilch, H. Krüger, D. Block, A. Piel, and S. Wolf, "Diagnostics and characterization of nanodust and nanodusty plasmas", The European Physical Journal D: Atomic, Molecular, Optical and Plasma Physics **72**, 81, ISSN: 1434-6060 (2018).

[9]I. Denysenko, J. Berndt, E. Kovacevic, I. Stefanovic, V. Selenin, and J. Winter, "The response of a capacitively coupled discharge to the formation of dust particles: Experiments and modeling", Physics of Plasmas **13**, 073507 (2006).

[10]N. Bilik, R. Anthony, B. A. Merritt, E. S. Aydil, and U. R. Kortshagen, "Langmuir probe measurements of electron energy probability functions in dusty plasmas", Journal of Physics D: Applied Physics **48**, 105204 (2015).

[11]B. Tadsen, F. Greiner, S. Groth, and A. Piel, "Self-excited dust-acoustic waves in an electron-depleted nanodusty plasma", Physics of Plasmas **22**, 113701, ISSN: 1070-664X (2015).

[12]P. S. Epstein, "On the Resistance Experienced by Spheres in their Motion through Gases", Physical Review **23**, 710–733 (1924).

[13]M. H. Thoma, H. M. Thomas, C. A. Knapek, A. Melzer, and U. Konopka, "Complex plasma research under microgravity conditions", npj Microgravity **9**, 10.1038/s41526-023-00261-8 (2023).

[14]A. Rutscher, "Characteristics of Low-Temperature Plasmas Under Nonthermal Conditions - A Short Summary, Fundamentals, Technologies and Techniques", in *Low Temperature Plasmas*, edited by R. Hippler, H. Kersten, M. Schmidt, and K. H. Schoenbach, 2nd ed. (Wiley-VCH, 2008), pp. 1–14, ISBN: 978-3-52740673-9.

[15]R. Hippler, "Elementary Processes of Plasma-Surface Interactions, Fundamentals, Technologies and Techniques", in *Low Temperature Plasmas*, edited by R. Hippler, H. Kersten, M. Schmidt, and K. H. Schoenbach, 2nd ed. (Wiley-VCH, 2008), pp. 71–102, ISBN: 978-3-52740673-9.

[16]H. Kersten and A. von Keudell, "Plasma-Surface Interaction, Fundamentals, Technologies and Techniques", in *Low Temperature Plasmas*, edited by R. Hippler, H. Kersten, M. Schmidt, and K. H. Schoenbach, 2nd ed. (Wiley-VCH, 2008), pp. 103–128, ISBN: 978-3-52740673-9.

[17]M. Dürr and U. Höfer, "Dissociative adsorption of molecular hydrogen on silicon surfaces", Surface Science Reports **61**, 465–526 (2006).

[18]J. J. H. Gielis, B. Hoex, P. J. van den Oever, M. C. M. van de Sanden, and W. M. M. Kessels, "Silicon surface passivation by hot-wire CVD Si thin films studied by in situ surface spectroscopy", Thin Solid Films **517**, 3456–3460, ISSN: 0040-6090 (2009).

[19]S. Agarwal, A. Takano, M. C. M. van de Sanden, D. Maroudas, and E. S. Aydil, "Abstraction of atomic hydrogen by atomic deuterium from an amorphous hydrogenated silicon surface", The Journal of Chemical Physics **117**, 10805–10816 (2002).

[20]G. S. Oehrlein and S. Hamaguchi, "Foundations of low-temperature plasma enhanced materials synthesis and etching", Plasma Sources Science and Technology **27**, 023001 (2018).

[21]J. A. Glass, E. A. Wovchko, and J. T. Yates, "Reaction of atomic hydrogen with hydrogenated porous silicon – detection of precursor to silane formation", Surface Science **348**, 325–334 (1996).

[22]A. von Keudell, "Surface processes during thin-film growth", Plasma Sources Science and Technology **9**, 455–467 (2000).

[23]Y. Lifshitz, S. R. Kasi, J. W. Rabalais, and W. Eckstein, "Subplantation model for film growth from hyperthermal species", Physical Review B **41**, 10468–10480 (1990).

[24]J. Robertson, "Deposition mechanisms for promoting sp^3 bonding in diamond-like carbon", Diamond and Related Materials **2**, 984–989 (1993).

[25]M. Hirasawa, T. Orii, and T. Seto, "Size-dependent crystallization of Si nanoparticles", Applied Physics Letters **88**, 093119, ISSN: 0003-6951 (2006).

[26]H. R. Maurer and H. Kersten, "On the heating of nano- and microparticles in process plasmas", Journal of Physics D: Applied Physics **44**, 174029 (2011).

[27]L. Mangolini, E. Thimsen, and U. Kortshagen, "High-Yield Plasma Synthesis of Luminescent Silicon Nanocrystals", Nano Letters **5**, 655–659 (2005).

[28]L. Mangolini and U. Kortshagen, "Selective nanoparticle heating: Another form of nonequilibrium in dusty plasmas", Physical Review E **79**, 026405, ISSN: 1539-3755 (2009).

[29]W. F. Bergerson, J. A. Mulder, R. P. Hsung, and X.-Y. Zhu, "Assembly of Organic Molecules on Silicon Surfaces via the Si-N Linkage", Journal of the American Chemical Society **121**, 454–455 (1998).

[30]J. M. Buriak, M. P. Stewart, T. W. Geders, M. J. Allen, H. C. Choi, J. Smith, D. Raftery, and L. T. Canham, "Lewis Acid Mediated Hydrosilylation on Porous Silicon Surfaces", Journal of the American Chemical Society **121**, 11491–11502 (1999).

[31]L. C. P. M. de Smet, H. Zuilhof, E. J. R. Sudhölter, L. H. Lie, A. Houlton, and B. R. Horrocks, "Mechanism of the Hydrosilylation Reaction of Alkenes at Porous Silicon: Experimental and Computational Deuterium Labeling Studies", The Journal of Physical Chemistry B **109**, 12020–12031 (2005).

[32]R. K. Baldwin, K. A. Pettigrew, E. Ratai, M. P. Augustine, and S. M. Kauzlarich, "Solution reduction synthesis of surface stabilized silicon nanoparticles", Chemical Communications, 1822–1823 (2002).

[33]R. D. Tilley and K. Yamamoto, "The Microemulsion Synthesis of Hydrophobic and Hydrophilic Silicon Nanocrystals", Advanced Materials **18**, 2053–2056 (2006).

[34]E. V. Rogozhina, D. A. Eckhoff, E. Gratton, and P. V. Braun, "Carboxyl functionalization of ultrasmall luminescent silicon nanoparticles through thermal hydrosilylation", Journal of Materials Chemistry **16**, 1421 (2006).

[35]G. Ledoux, O. Guillois, D. Porterat, C. Reynaud, F. Huisken, B. Kohn, and V. Paillard, "Photoluminescence properties of silicon nanocrystals as a function of their size", Physical Review B **62**, 15942–15951 (2000).

[36]G. Ledoux, J. Gong, F. Huisken, O. Guillois, and C. Reynaud, "Photoluminescence of size-separated silicon nanocrystals: Confirmation of quantum confinement", Applied Physics Letters **80**, 4834–4836 (2002).

[37]Y.-C. Liao and J. T. Roberts, "Self-Assembly of Organic Monolayers on Aerosolized Silicon Nanoparticles", Journal of the American Chemical Society **128**, 9061–9065 (2006).

[38]L. Mangolini and U. Kortshagen, "Nonthermal Plasma Synthesis of Silicon Nanocrystals", in *Silicon Nanocrystals*, edited by L. Pavesi and R. Turan (Wiley-VCH Verlag GmbH & Co. KGaA, Weinheim, 2010-04), pp. 309–348, ISBN: 978-3-527-32160-5.

[39]S. Bayda, M. Adeel, T. Tuccinardi, M. Cordani, and F. Rizzolio, "The History of Nanoscience and Nanotechnology: From Chemical–Physical Applications to Nanomedicine", Molecules **25**, 112, ISSN: 1420-3049 (2019).

[40]J. R. Chelikowsky and M. L. Cohen, "Electronic structure of silicon", Physical Review B **10**, 5095–5107, ISSN: 0163-1829 (1974).

[41]W. Shockley and W. T. Read, "Statistics of the Recombinations of Holes and Electrons", Physical Review **87**, 835–842 (1952).

[42]R. N. Hall, "Electron-Hole Recombination in Germanium", Physical Review **87**, 387–387 (1952).

[43]S. Ossicini, L. Pavesi, and F. Priolo, "Light Emitting Silicon for Microphotonics", in *Springer Tracts in Modern Physics* (Springer, Berlin, 2003), ISBN: 978-3-54040233-6.

[44]L. L. Araujo and M. C. Ridgway, "Embedded nanoparticles", in *Handbook of Nanophysics: Nanoparticles Quantum Dots*, edited by K. D. Sattler (CRC Press Taylor & Francis Group, Boca Raton, London, New York, 2010), pp. 405–418, ISBN: 978-1-4200-7545-8.

[45]H. Wiggers and A. Lorke, "Silicon nanocrystals", in *Handbook of Nanophysics: Nanoparticles Quantum Dots*, edited by K. D. Sattler (CRC Press Taylor & Francis Group, Boca Raton, London, New York, 2010), ISBN: 978-1-4200-7545-8.

[46]J. Linnros, "Nanocrystals brighten transistors", Nature Materials **4**, 117–119 (2005).

[47]U. Kortshagen, "Nonthermal plasma synthesis of semiconductor nanocrystals", Journal of Physics D: Applied Physics **42**, 10.1088/0022-3727/42/11/113001, ISSN: 0022-3727 (2009).

[48]L. Mangolini, "Synthesis, properties, and applications of silicon nanocrystals", Journal of Vacuum Science & Technology B **31**, 020801, ISSN: 2166-2746 (2013).

[49]F. Hua, M. T. Swihart, and E. Ruckenstein, "Efficient Surface Grafting of Luminescent Silicon Quantum Dots by Photoinitiated Hydrosilylation", Langmuir **21**, 6054–6062, ISSN: 0743-7463 (2005).

[50]M. V. Wolkin, J. Jorne, and P. M. Fauchet, "Electronic States and Luminescence in Porous Silicon Quantum Dots: The Role of Oxygen", Physical Review Letters **82**, 197–200 (1999).

[51]D. Kovalev, H. Heckler, G. Polisski, and F. Koch, "Optical Properties of Si Nanocrystals", physica status solidi (b) **215**, 871–932 (1999).

[52]M. Fujii, "Optical Properties of Intrinsic and Shallow Impurity-Doped Silicon Nanocrystals", in *Silicon Nanocrystals*, edited by L. Pavesi and R. Turan (Wiley-VCH Verlag GmbH & Co. KGaA, Weinheim, 2010), pp. 43–68, ISBN: 978-3-527-32160-5.

[53]J. Veinot, "Surface Passivation and Functionalization of Si Nanocrystals", in *Silicon Nanocrystals*, edited by L. Pavesi and R. Turan (Wiley-VCH Verlag GmbH & Co. KGaA, Weinheim, 2010), pp. 155–172, ISBN: 978-3-527-32160-5.

[54]E. Kovačević, J. Berndt, T. Strunskus, and L. Boufendi, "Size dependent characteristics of plasma synthesized carbonaceous nanoparticles", Journal of Applied Physics **112**, 013303, ISSN: 0021-8979 (2012).

[55]J. Berndt, E. Kovačević, I. Stefanović, O. Stepanović, S. H. Hong, L. Boufendi, and J. Winter, "Some Aspects of Reactive Complex Plasmas", Contributions to Plasma Physics **49**, 107–133, ISSN: 0863-1042 (2009).

[56]H. Yasuda and T. Hsu, "Some aspects of plasma polymerization investigated by pulsed R.F. discharge", Journal of Polymer Science: Polymer Chemistry Edition **15**, 81–97 (1977).

[57]A. Gallagher, "Model of particle growth in silane discharges", Physical Review E **62**, 2690–2706, ISSN: 1063-651X (2000).

[58]A. A. Fridman, L. Boufendi, T. Hbid, B. V. Potapkin, and A. Bouchoule, "Dusty plasma formation: Physics and critical phenomena. Theoretical approach", Journal of Applied Physics **79**, 1303–1314, ISSN: 0021-8979 (1996).

[59]P. Agarwal and S. L. Girshick, "Sectional modeling of nanoparticle size and charge distributions in dusty plasmas", Plasma Sources Science and Technology **21**, 055023, ISSN: 0963-0252 (2012).

[60]M. Shiratani, H. Kawasaki, T. Fukuzawa, T. Yoshioka, Y. Ueda, S. Singh, and Y. Watanabe, "Simultaneous in situ measurements of properties of particulates in rf silane plasmas using a polarization-sensitive laser-light-scattering method", Journal of Applied Physics **79**, 104–109, ISSN: 0021-8979 (1996).

[61]L. Ravi and S. L. Girshick, "Coagulation of nanoparticles in a plasma", Physical Review E **79**, 026408, ISSN: 1539-3755 (2009).

[62]L. Boufendi and A. Bouchoule, "Particle nucleation and growth in a low-pressure argon-silane discharge", Plasma Sources Science and Technology **3**, 262–267, ISSN: 0963-0252 (1994).

[63]M. Cavarroc, M. Mikikian, L. Couëdel, and L. Boufendi, "Formation of single-crystal silicon nanoparticles at very low gas temperature in a rf silane-based discharge", in 33rd European Physical Society Conference on Plasma Physics, Vol. 2 (2006), pp. 1392–1395, ISBN: 978-1-62276-333-7.

[64]M. Cavarroc, M. C. Jouanny, K. Radouane, M. Mikikian, and L. Boufendi, "Self-excited instability occurring during the nanoparticle formation in an Ar–SiH_4 low pressure radio frequency plasma", Journal of Applied Physics **99**, 064301, ISSN: 0021-8979 (2006).

[65]J. Lin, S. Orazbayev, M. Hénault, T. Lecas, K. Takahashi, and L. Boufendi, "Effects of gas temperature, pressure, and discharge power on nucleation time of nano-particles in low pressure C_2H_2/Ar RF plasmas", Journal of Applied Physics **122**, 163302 (2017).

[66]S. A. Orazbayev, M. Henault, T. S. Ramazanov, L. Boufendi, D. G. Batryshev, and M. T. Gabdullin, "Influence of Gas Temperature on Nucleation and Growth of Dust Nanoparticles in RF Plasma", IEEE Transactions on Plasma Science **47**, 3069–3073, ISSN: 1939-9375 (2019).

[67]C. Deschenaux, A. Affolter, D. Magni, C. Hollenstein, and P. Fayet, "Investigations of CH_4, C_2H_2 and C_2H_4 dusty RF plasmas by means of FTIR absorption spectroscopy and mass spectrometry", Journal of Physics D: Applied Physics **32**, 1876–1886, ISSN: 0022-3727 (1999).

[68]E. Kovačević, I. Stefanović, J. Berndt, and J. Winter, "Infrared fingerprints and periodic formation of nanoparticles in Ar/C_2H_2 plasmas", Journal of Applied Physics **93**, 2924–2930, ISSN: 0021-8979 (2003).

[69]D. Herrebout, A. Bogaerts, M. Yan, R. Gijbels, W. Goedheer, and E. Dekempeneer, "One-dimensional fluid model for an rf methane plasma of interest in deposition of diamond-like carbon layers", Journal of Applied Physics **90**, 570–579, ISSN: 0021-8979 (2001).

[70]K. De Bleecker, A. Bogaerts, and W. Goedheer, "Detailed modeling of hydrocarbon nanoparticle nucleation in acetylene discharges", Physical Review E **73**, 026405, ISSN: 1539-3755 (2006).

[71]D. A. Ariskin, I. V. Schweigert, A. L. Alexandrov, A. Bogaerts, and F. M. Peeters, "Modeling of chemical processes in the low pressure capacitive radio frequency discharges in a mixture of Ar/C_2H_2", Journal of Applied Physics **105**, 063305, ISSN: 0021-8979 (2009).

[72]J. Benedikt, "Plasma-chemical reactions: low pressure acetylene plasmas", Journal of Physics D: Applied Physics **43**, 043001, ISSN: 0022-3727 (2010).

[73]M. L. Mandich, W. D. Reents, and K. D. Kolenbrander, "Sequential clustering reactions of SiD_3^+ with SiD_4 and SiH_3^+ with SiH_4 : Another case of arrested growth of hydrogenated silicon particles", The Journal of Chemical Physics **92**, 437–451, ISSN: 0021-9606 (1990).

[74]K. De Bleecker, A. Bogaerts, R. Gijbels, and W. Goedheer, "Numerical investigation of particle formation mechanisms in silane discharges", Physical Review E **69**, 056409, ISSN: 1063-651X (2004).

[75]K. De Bleecker, A. Bogaerts, W. Goedheer, and R. Gijbels, "Investigation of Growth Mechanisms of Clusters in a Silane Discharge With the Use of a Fluid Model", IEEE Transactions on Plasma Science **32**, 691–698, ISSN: 0093-3813 (2004).

[76]H. Haberland, M. Karrais, M. Mall, and Y. Thurner, "Thin films from energetic cluster impact: A feasibility study", Journal of Vacuum Science & Technology A: Vacuum, Surfaces, and Films **10**, 3266–3271, ISSN: 0734-2101 (1992).

[77]H. Haberland, "History, Some Basics, and an Outlook", in *Gas-Phase Synthesis of Nanoparticles*, edited by Y. Huttel (Wiley-VCH Verlag GmbH & Co. KGaA, 2017-06-19), pp. 3–21, ISBN: 978-3-52734060-6.

[78]J. A. De Toro, P. S. Normile, and C. Binns, "Types of Cluster Sources", in *Gas-Phase Synthesis of Nanoparticles*, edited by Y. Huttel (Wiley-VCH Verlag GmbH & Co. KGaA, 2017-06-19), pp. 39–55, ISBN: 978-3-52734060-6.

[79]O. Polonskyi, A. M. Ahadi, T. Peter, K. Fujioka, J. W. Abraham, E. Vasiliauskaite, A. Hinz, T. Strunskus, S. Wolf, M. Bonitz, H. Kersten, and F. Faupel, "Plasma based formation and deposition of metal and metal oxide nanoparticles using a gas aggregation source", The European Physical Journal D **72**, 10.1140/epjd/e2017-80419-8 (2018).

[80]J. Drewes, S. Ali-Ogly, T. Strunskus, O. Polonskyi, H. Biederman, F. Faupel, and A. Vahl, "Impact of argon flow and pressure on the trapping behavior of nanoparticles inside a gas aggregation source", Plasma Processes and Polymers **19**, 2100125 (2021).

[81]O. Kylián, A. Shelemin, P. Solař, P. Pleskunov, D. Nikitin, A. Kuzminova, R. Štefaníková, P. Kúš, M. Cieslar, J. Hanuš, A. Choukourov, and H. Biederman, "Magnetron Sputtering of Polymeric Targets: From Thin Films to Heterogeneous Metal/Plasma Polymer Nanoparticles", Materials **12**, 2366 (2019).

[82]J. Drewes, A. Vahl, N. Carstens, T. Strunskus, O. Polonskyi, and F. Faupel, "Enhancing composition control of alloy nanoparticles from gas aggregation source by in operando optical emission spectroscopy", Plasma Processes and Polymers **18**, 2000208 (2020).

[83]N. B. Colthup, L. H. Daly, and S. E. Wiberley, *Introduction to Infrared and Raman Spectroscopy* (1990), ISBN: 978-0-12-182554-6.

[84]G. Socrates, *Infrared and Raman Characteristic Group Frequencies, Tables and Charts*, 3rd ed. (Wiley, Chichester, 2001), ISBN: 978-0-470-09307-8.

[85]P. R. Griffiths and J. A. de Haseth, *Fourier Transform Infrared Spectrometry*, 2nd ed. (John Wiley & Sons, Inc., Hoboken, New Jersey, 2007-04), ISBN: 978-0-471-19404-0.

[86]NIST Mass Spectrometry Data Center and William E. Wallace, director, "Infrared Spectra", in *NIST Chemistry WebBook, NIST Standard Reference Database Number 69*, edited by P. J. Linstrom and W. G. Mallard (2023).

[87]A. S. Wexler, "Integrated Intensities of Absorption Bands in Infrared Spectroscopy", Applied Spectroscopy Reviews **1**, 29–98, ISSN: 0570-4928 (1967).

[88]J.-J. Greffet, "Introduction to Surface Plasmon Theory", in *Plasmonics*, edited by S. Enoch and N. Bonod (Springer, Berlin Heidelberg, 2012), pp. 105–148, ISBN: 978-3-642-28078-8.

[89]J. Aizpurua and R. Hillenbrand, "Localized Surface Plasmons: Basics and Applications in Field-Enhanced Spectroscopy", in *Plasmonics*, edited by S. Enoch and N. Bonod (Springer, Berlin Heidelberg, 2012), pp. 151–176, ISBN: 978-3-642-28078-8.

[90]H. Ibach, *Physics of Surfaces and Interfaces* (Springer, Berlin Heidelberg, 2006), ISBN: 978-3-540-34709-5.

[91]L. Reimer and H. Kohl, *Transmission Electron Microscopy, Physics of Image Formation*, 5th ed. (Springer New York, 2008), ISBN: 978-0-387-40093-8.

[92]P. D. Nellist, "The Principles of STEM Imaging", in *Scanning Transmission Electron Microscopy, Imaging and Analysis*, edited by S. J. Pennycook and P. D. Nellist (Springer New York, 2011), pp. 91–115, ISBN: 978-1-4419-7199-9.

[93]M. Born and E. Wolf, *Principles of Optics, 60th Anniversary Edition* (University of Cambridge ESOL Examinations, 2019), ISBN: 978-1-108-47743-7.

3

Experimental setups and diagnostics

The crucial parameter for the treatment and coating of nanoparticles is their residence time in the treatment region. Prior works using in-flight treatment setups were able to increase the residence times from a few milliseconds to the order order of seconds [1–4]. This is achieved by increasing the pressure in the deposition region to several tens of Pa to decelerate particles through collisions with neutral gas from the 10–100 $\mathrm{m\,s^{-1}}$ at the gas aggregation source (GAS) to values in the order of tens of $\mathrm{cm\,s^{-1}}$. With deposition rates in the order of $\mathrm{nm\,s^{-1}}$, this gives enough time to create coatings of a few nanometre thickness during the residence time in the deposition region.

One option for larger shells is the inclusion of a reactive gas directly inside the GAS. Solař et al. [5] demonstrated the generation of silver-polymer multi-core-shell nanoparticles through the addition of hexamethyldisiloxane (HMDSO) in front of the sputter target. The resulting nanoparticles consisted of multiple silver cores inside of a single polymer shell. The cores were significantly smaller than under operation without HMDSO, as the injection of the reactive gas drastically changes the conditions for condensation.

Larger shells through longer residence times can be achieved by using a secondary plasma discharge. One proof of principle setup was described by Libenská et al. [6], using a circular antenna in a secondary chamber to create a radio frequency (RF) deposition plasma. This plasma was not used for depositing new material onto the particles, but rather annealed the previously amorphous iron carbide nanoparticle to become crystalline cementite (Fe_3C) covered by a thin hydrocarbon shell. Given their setup, particles need to naturally leave the secondary discharge to be deposited for extraction. This led to the choice of pulsing the RF plasma at 100 Hz with a duty cycle of 75 %. The authors show that particles become trapped in the secondary discharge for at least 24 s, although the exact mechanisms of how the particles leave the discharge are not investigated in detail.

The primary goal of this work is the creation of a secondary plasma system capable of confining particles for minutes to hours. This enables various options for controlled treatment, monitoring, and extraction of nanoparticles that would otherwise not be possible. The first section of this chapter presents Fourier-transform infrared spectroscopy (FTIR) which is used as the main diagnostic tool to analyse

and monitor the chemical composition of the particles and the applied surface treatments. Where section 2.5.1 focused on the operating principles of an FTIR spectrometer, here, the actual setup will be described. After the treatment of the particles, an electrostatic extraction system is used to prepare samples for ex situ analysis. The second section describes the different setups used for extraction. The final three sections describe the different setups used in this work to produce different compositions: carbon and silicon nanoparticles, and silver-silica core-shell nanoparticles.

3.1 Infrared absorption spectroscopy

The central piece of the infrared absorption spectroscopy setup is the commercial Bruker Vertex 80v FTIR spectrometer. It is equipped with a potassium bromide (KBr) beam splitter for operation in the mid-infrared (MIR) range from 10 000–380 cm^{-1}. The measurements in this work make use of its rapid scan option, which increases the mirror velocity to record up to 11 scans per second at a resolution of 2 cm^{-1}. Typically 64 spectra are averaged to give one data point, resulting in a time resolution of one spectrum every 6–7 s. To avoid aliasing effects as described in section 2.5.1, an optical long wave pass filter is installed in the filter wheel to cut off any incoming spectral components above 3861 cm^{-1}.

For the measurements in this work, the right exit of the spectrometer is used to obtain a collimated infrared beam with a diameter of 40 mm. It is then focused down to a spot of about 5 mm diameter using a converging mirror lens with a long focal length of $f = 1106\,\mathrm{mm}$. The entire beam path is encased in two aluminium boxes connected via a sealed aluminium tube, which is constantly flushed with dry nitrogen gas to limit the absorption by CO_2 and H_2O in ambient air.

Using a system of two mirrors, the focus point is positioned on the KBr entry window of a commercial multi-pass cell (also called a White cell) by neoplas control GmbH that was custom made for the exact dimensions of the plasma chamber with a flange distance of 283.3 mm. It consists of two CF40 flanges with the field mirror on the entry/exit window side and the two object mirrors on the opposing side. Additional gas inlets provide a protective argon flow over the mirrors to avoid possible particle depositions. After passing through the entry window, the beam defocuses again until being reflected at the object mirror, which is a reflective lens focusing it back to a point on the field mirror. This is the reason for using a long focal length for the initial converging mirror lens, as the beam diameter at the object mirror should not exceed the mirror's dimensions and so the numerical aperture of the focusing lens needs to be chosen very small.

The geometry of the cell allows for $4n$ reflections before the exit window is hit and the number of reflections can be set dynamically from outside the vacuum chamber via a thumb screw. As the mirrors only have about 96.5 % reflectivity in the infrared and about 95 % in the ultraviolet-visible (UV-Vis) range, the exit

intensity becomes lower with an increasing number of reflections.

After exiting the multi-pass cell, the beam is focused using a zinc selenide (ZnSe) lens onto a liquid nitrogen cooled mercury cadmium telluride (MCT) detector. The detector has a spectral range of 12 000–850 cm^{-1}, determining the final usable spectral range of the entire setup to be 3861–850 cm^{-1} with the upper bound determined by the LWP filter and the lower bound set by the detector.

3.1.1 Adaptation for UV-Vis spectroscopy

The setup can quickly be converted for UV-Vis measurements of localised surface plasmon resonance (LSPR) measurements which were described in section 2.5.2. A combined deuterium / halogen light source (OceanOptics DH-2000-BAL-TTL-24V) is used to perform the UV-Vis spectroscopy and provides a balanced output in the range from 210–2500 nm by specifically filtering the deuterium D_α emission lines leaving a continuous spectrum that does not lead to saturation in the measured spectra. The light is coupled into the setup via a vertical arrangement of a glass fibre adapter with collimation optics and 45° mirror that is placed in the dotted region in fig. 3.1. This places the collimated white light onto the same beam path as the infrared beam from the FTIR to minimise adjustments on the remaining setup, making it possible to switch between UV-Vis and infrared measurements with minimal effort. The beam is then decoupled by replacing the mirror after the exit of the multi-pass with a focusing lens and a glass fibre adapter, which then is connected to an Ocean Optics USB4000 spectrometer capable of measuring the spectral range from 200–1100 nm.

As the LSPR leads to comparatively strong absorption, the multi-pass cell is set to the lowest setting at 4 reflections in this case. This low number of reflections already leads to a peak absorption intensities of up to 80 % for the highest silver nanoparticle densities shown in section 4.3.1 giving an excellent signal-to-noise ratio of $A/\Delta A = 50$.

3.1.2 Spectral decomposition

An FTIR measurement consists of taking two spectra: a reference (labelled with `Rf` in the OPUS software) and a sample spectrum (labelled with `Sm`). The reference spectrum is taken prior to the start of the experiment in an empty chamber without nanoparticles to determine the spectrum of the IR source and the detector sensitivity curve. The transmission spectrum is then calculated by taking the ratio of sample spectrum to its reference spectrum as shown in the previous chapter in fig. 2.8c.

To obtain quantitative data from the measured infrared transmission spectra, a fit-based approach is used, which decomposes the spectrum into its constituting vibrational excitation modes. As particle densities can reach the order of 10^{13} m^{-3} and particles can grow to diameters up to hundreds of nanometres, significant

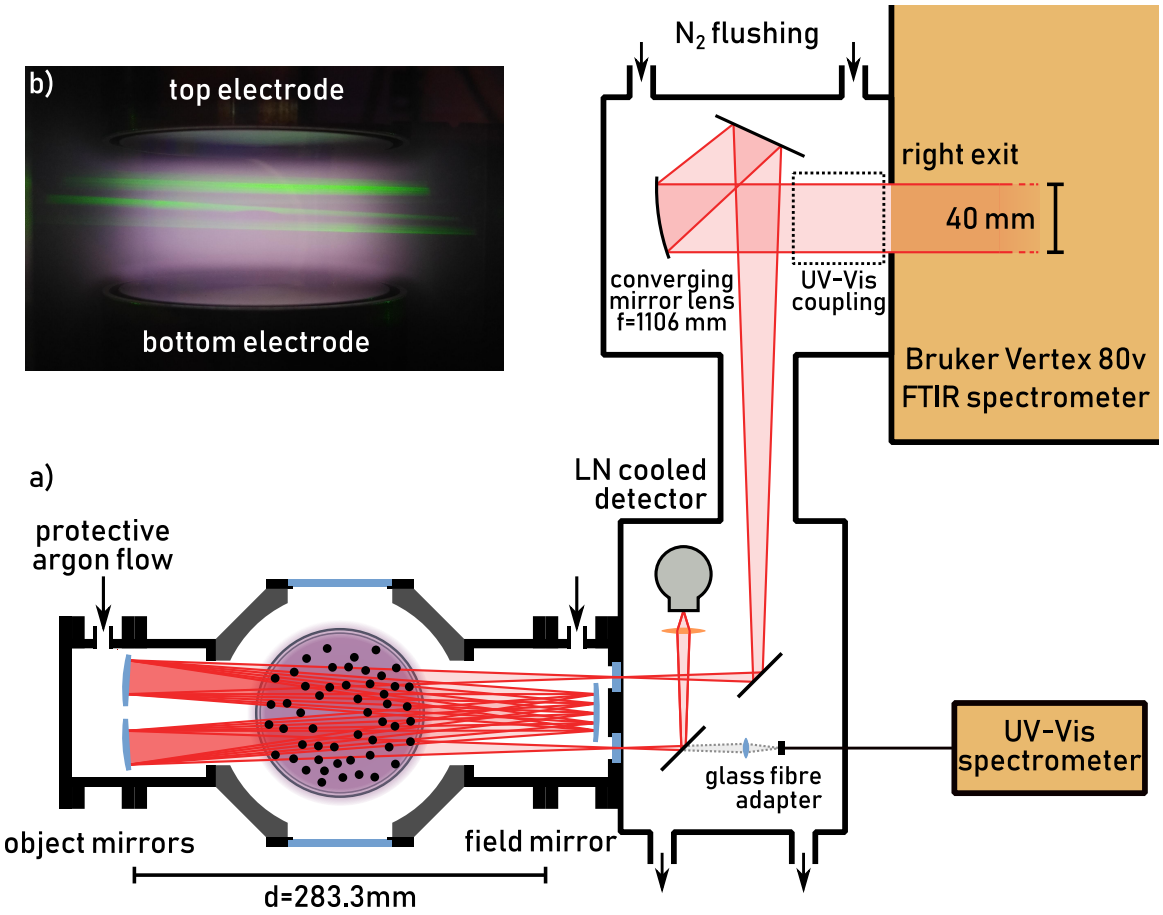

Figure 3.1: a) Top view sketch of the infrared beam path. The beam originates in the Bruker Vertex 80v FTIR spectrometer as a collimated beam with a diameter of 40 mm. It is then be focused down to a point of about 5 mm diameter using a converging mirror lens with a focal length of 1106 mm and a set of two reflective mirrors that guide the beam through a tunnel setup into the secondary box. The focused beam enters the multi-pass cell through a KBr window and is reflected back and forth, each time being defocused on the way to the object mirrors and refocused on the way to the field mirror. After $4n$ reflections it exits the multi-pass cell through another KBr window and is reflected onto a ZnSe optical lens which focuses the beam onto the liquid nitrogen cooled MCT detector. The entire beam path outside of the plasma chamber is enclosed in a nitrogen-flushed aluminium box to avoid atmospheric absorptions from ambient air. Alternatively for UV-Vis measurements, a collimated beam from a broad white light source can be coupled in at the marked spot coming from above the drawing plane and being reflected into the drawing plane with a 45° mirror. The mirror in front of the exit of the multi-pass cell is replaced with a focusing lens and a glass fibre adapter connected to an UV-Vis spectrometer. b) Picture of the side view into the plasma chamber. A green laser beam was used with the UV-Vis coupling system to trace the beam path through the chamber. The green light is scattered by carbon nanoparticles created in the capacitively coupled plasma (CCP) discharge.

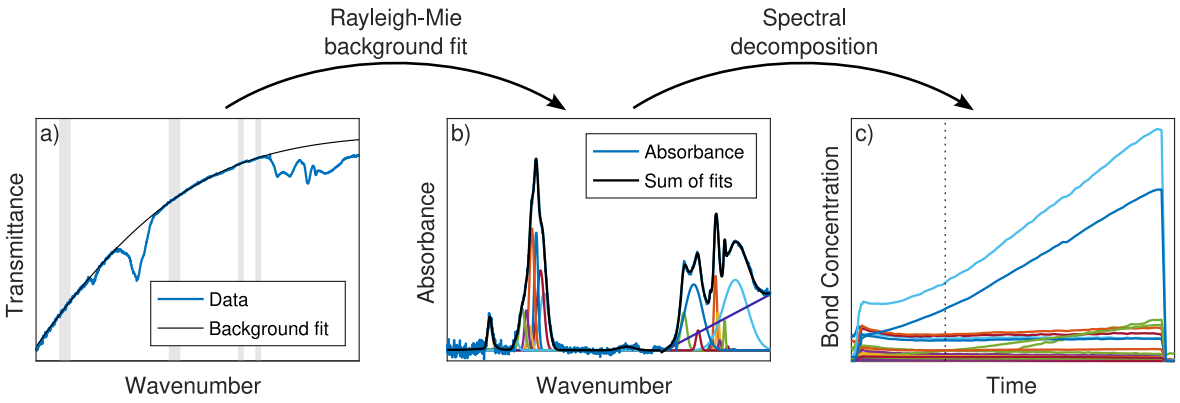

Figure 3.2: Schematic overview of the data analysis procedure. a) Measured transmittance data I/I_0 with fitted Rayleigh-Mie background shown in black. Regions used for fit are marked in grey. b) Corrected absorbance data after subtraction of background. Overlaid are 29 different Gaussian functions for each visible vibrational excitation mode with the sum of all fits shown in black. c) Calculated bond concentrations from the performed fit shown over time. The spectrum of the previous figures was taken at the time indicated by a dotted line.

Rayleigh-Mie scattering can occur in the infrared region. Absorption spectra are therefore processed by first fitting a Rayleigh-Mie background in regions without vibrational absorption lines, as shown in fig. 3.2a. The resulting background-corrected absorption curve now only contains the vibrational absorption lines and bands from different bonds and molecules.

To differentiate and quantify them, Gaussian functions are fitted to this data obtaining a spectral decomposition[1]. Depending on the pressure and temperature range, the absorption lines can show both Doppler and collision broadening and the use of other profiles such as a Lorentzian or Voigt profile (the convolution of a Lorentzian with a Gaussian profile) may be necessary. The position and width of the resonance of the individual oscillators in the particle depends on their local environment. In some cases such as amorphous hydrogenated silicon (a-Si:H) nanoparticles, this allows for the differentiation between bulk and surface bonds, where surface bonds show significantly narrower absorption peaks than their bulk counterparts, sometimes at slightly shifted wavenumbers. As the composition of the material can change over time, reference works often give ranges for absorption peak positions and widths, which need to be considered during the fitting process.

The spectral decomposition is done using the FTIR Suite [7] created as part of this PhD work. It is a collection of classes written in MATLAB for the processing of absorption spectroscopy data from the Bruker OPUS `.0` format with the steps

[1]In the literature, this is often called *spectral deconvolution*. It is an incorrect application of the term "deconvolution" found in signal processing to describe reverting the mathematical convolution of the underlying signal with the instrumental profile. In the present case of a superposition of multiple absorption peaks, no convolution is involved. Therefore, I decided to use the less common, yet more correct term *decomposition* for describing this processing step.

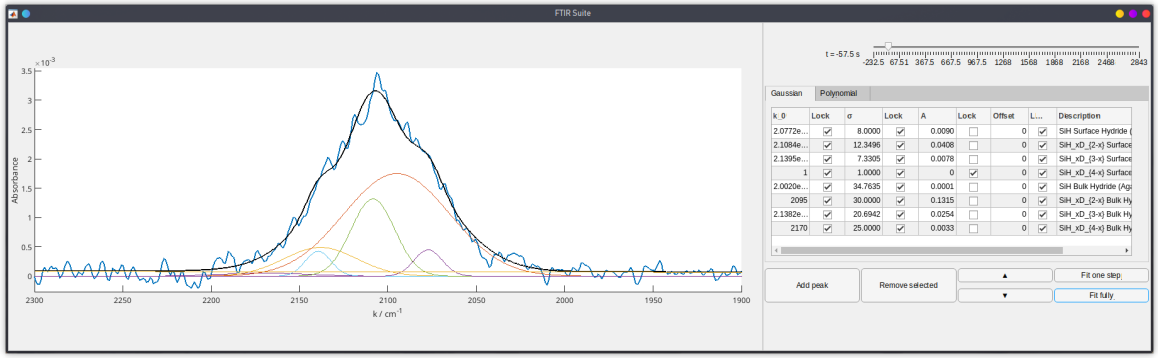

Figure 3.3: Region edit view of the `OverviewFitAnalysis` class of the FTIR Suite. A number of gaussian and polynomial functions are listed to be fitted to the spectrum. The measured data is shown in blue, while the sum of fitted lines is overlaid in black.

shown in figs. 2.8 and 3.2. It performs the necessary background corrections and provides a user interface for manipulating the different Gaussian peaks during spectral decomposition (see. fig. 3.3).

The analysis for a single curve is done in an iterative process. First, all entered peaks are fitted to the given data. Then, if negative absorption intensities are found, which can often occur for noisy data and narrow peak widths, all negative entries are removed from the collection of functions to be fitted, and the fit is run again. The removal of negative peaks is preferable to setting a lower bound to their amplitude as it adds numerical stability to the fitting routine. This process is repeated until no further negative absorption intensities are obtained. This entire procedure is then repeated for each single measurement in a series to obtain the time evolution of the integrated absorption of each absorption peak shown in fig. 3.2c.

In the last step, the integrated absorption along the line-of-sight of the infrared spectrometer needs to be converted into bond concentrations. Both the path length through the particle cloud and the specific oscillator strength of the respective vibrational excitation need to be known (see section 2.5.1). For the silicon and silver-silica core-shell experiments described in sections 3.4 and 3.5, a confining mesh was used, clearly defining the extents of the particle cloud, whereas for the carbon experiments in section 3.3 the extent of the dust cloud needs to be estimated. Furthermore, as the central void (dust-free region, see section 2.2.2) can be present in the beam path, the measured integrated absorption will vary when the void changes its size during the experiment, e.g. when electronegative reactive gasses are introduced, increasing the ion wind force on the particles. This effect was not corrected for and is present as an artefact in the processed absorption time evolutions.

Table 3.1: Assignment of absorption peak positions $\bar{\nu}$ and widths σ for the decomposition of absorption spectra of amorphous hydrogenated carbon (a-C:H) nanoparticles. Absorption lines in the second half of the table were not used for further analysis in this work.

Excitation mode	$\bar{\nu}/\mathrm{cm}^{-1}$	σ/cm^{-1}	Reference
sp^2CH_2 olef. asym. str.	3085	20	[8–10]
sp^2CH arom. str.	3035	23	[8–10]
sp^2CH olef. sym. str.	3000	16	[8–10]
sp^2CH_2 olef. sym. str.	2975	18	[8–10]
sp^3CH_3 asym. str.	2955	20	[8–10]
sp^3CH, sp^3CH_2 asym. str.	2920	16	[8–10]
sp^3CH_3 sym. str.	2885	28	[8–10]
sp^3CH_2 sym. str.	2855	40	[8–10]
H-bonded OH str.	3320	100	[10, 11]
C=O str.	1710	25	[10]
cyclic C=O str.	1670	13	[10]
Not used in further analysis			
sp^1CH str.	3300	18	[8]
CC skeletal str.	2180	70	[8]
	1630	70	[12]
	1592	18	[12]
	1300	120	[12]
sp^3CH_3 asym. bend.	1480	15	[8, 9]
sp^3CH_2 asym. bend.	1450	13	[8, 9]
sp^2CH arom. bend.	1430	12	[8, 9]
sp^2CH_2 olef. bend.	1415	11	[8, 9]
sp^3CH_3 sym. bend.	1375	8	[8, 9]
C_2H_2	3310	21	[13]
	3257	22	[13]
	1740	20	[13]
	1351	11	[13]
	1303	16	[13]
unidentified C_2H_2 product	1251	6	—
	1232	6	—
unidentified	1493	5	—

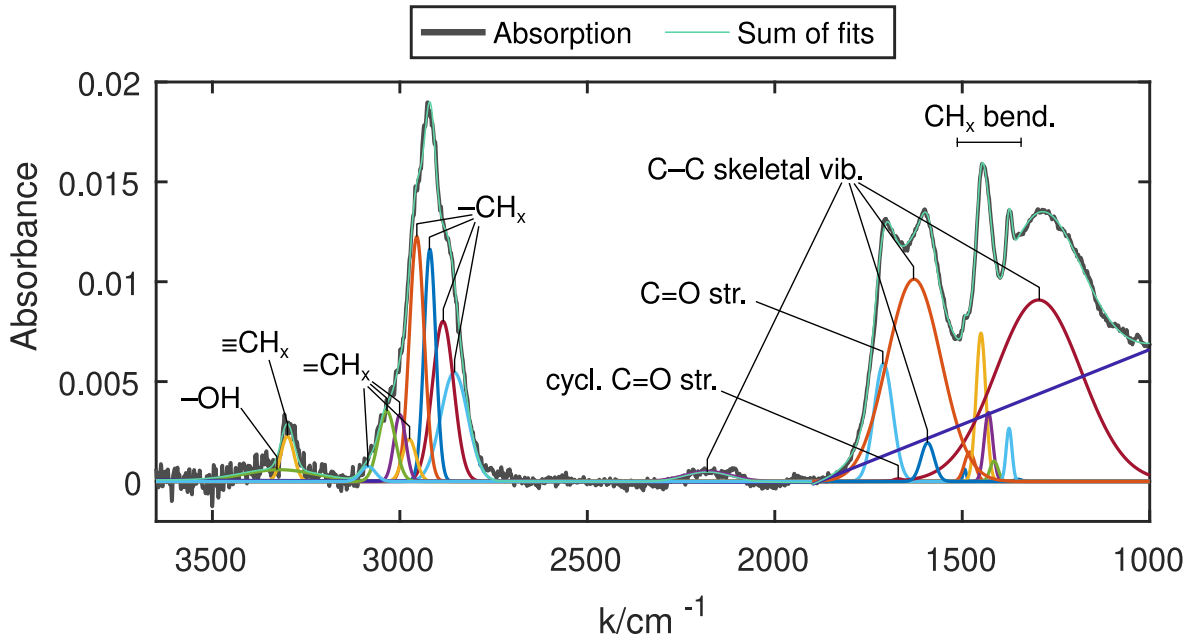

Figure 3.4: Decomposition of an infrared absorption spectrum of argon-treated a-C:H nanoparticles shortly after generation. Gaussian peaks were fitted to the data according to table 3.1. An additional linear background is applied in the region from 1900–1000 cm^{-1} (marked in purple).

3.1.2.1 Line assignments for carbon bonds

The absorption spectra of a-C:H material shows two large features in the measured region: CH_x stretching vibrations [8–10] between 2800–3100 cm^{-1} and the region below 1900 cm^{-1} with CH_x bending [8–10], C=O stretching [10], and H-bonded OH stretching vibrations [10, 11], as well as skeletal vibrations of the underlying C−C bonds [12]. Peak positions $\bar{\nu}$ and corresponding widths σ were kept constant for all fits and can be found in table 3.1. An exemplary decomposition of an absorption spectrum is shown in fig. 3.4. Integrated absorption intensities for the analysed lines are given by Wexler [10, 14] with an additional correction for the refractive index of the used solvent described by Ristein et al. [15].

Carbon in its different hybridisation states can be differentiated in infrared spectra, i.e. sp^3-hybridised carbon with four single bonds has a different oscillation frequency than sp^2-hybridised carbon with a double bond and two single bonds. In this work, the ratio between sp^2 and sp^3-hybridised CH bonds in the infrared spectra is used to show the effects of various treatments. Such analysis needs to be performed with care, as a metastudy for diamondlike carbon (DLC) films comparing results from nuclear magnetic resonance spectroscopy (NMR), forward recoil elastic scattering (FRES), electron energy loss spectroscopy (EELS), ion beam analysis (IBA), and combustion analysis has proven infrared spectroscopy based results to be unreliable for measuring parameters such as the H-content of a film or the ratio of sp^2 to sp^3 bound carbon sites [16]. These are relevant parameters for the characterization of DLC films for, e.g. their optical

gap, electrical resistivity, or mechanical properties.

One source of this uncertainty is the assumption of constant oscillator strengths for the different CH_x groups over the course of the treatment. As the structure of the film changes, the individual dipole moments can change depending on their local environment, which leads to the misestimation of concentrations. Furthermore, as the infrared analysis can only detect hydrogenated carbon, i.e. carbon atoms bound to hydrogen. Any unhydrogenated site will not be accounted for. For DLC films it has been shown that a significant portion of hydrogen of up to 50 % can be present in an unbounded state trapped interstitially in the film structure [17]. While almost all sp^3 hybridised carbon atoms are bounded to hydrogen, only a third of sp^2 carbon is hydrogenated. The infrared analysis therefore cannot be used to determine the proportions of the three phases of sp^3 carbon, sp^2 carbon, and hydrogen in the film. As was suggested by Grill et al. [17], in this work, infrared analysis is therefore only used to identify changes to the material during the various treatments rather than make absolute statements about the carbon fractions.

During oxygen treatment, CO_2 and CO absorption bands appear between 2300–2380 cm^{-1} and 2060–2220 cm^{-1} respectively. The integrated absorbance of these bands was converted into concentrations using calibration factors by Ventura et al. [18] for CO_2 and Buback et al. [19] for CO.

3.1.2.2 Line assignments for silicon bonds

The decomposition of the various silicon hydride and deuteride bonds in absorption spectra is performed following the work of Agarwal et al. [20] (see fig. 3.5). They assign peaks in the region 1900–2300 cm^{-1} to the vibrational stretching excitation of hydrides and the region 1400–1600 cm^{-1} to deuterides as detailed in table 3.2. The different peak positions for hydrides and deuterides stem from

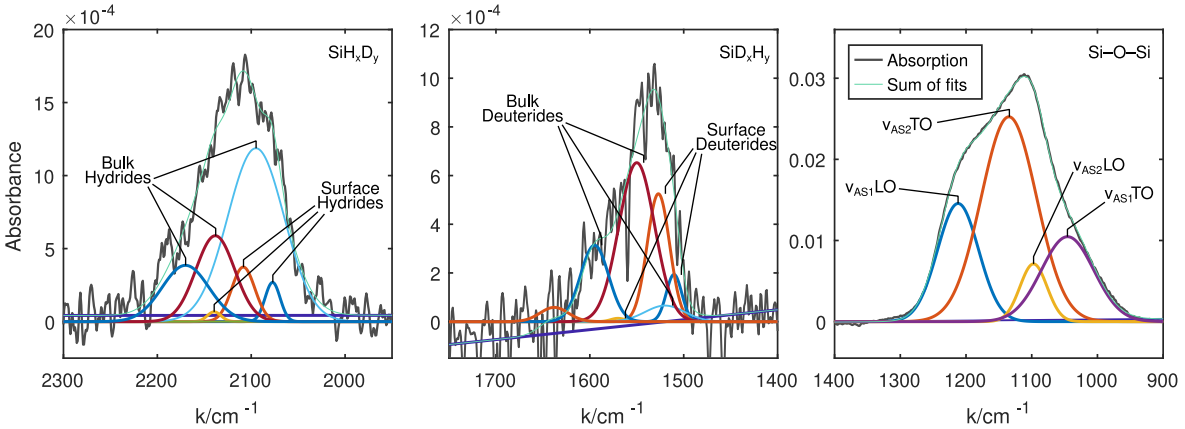

Figure 3.5: Decomposition of an infrared absorption spectrum of silicon nanoparticles into hydrides, deuterides and Si−O−Si bonds. Gaussian peaks are fitted to the data according to table 3.2. An additional linear background is fitted to the data (marked in purple).

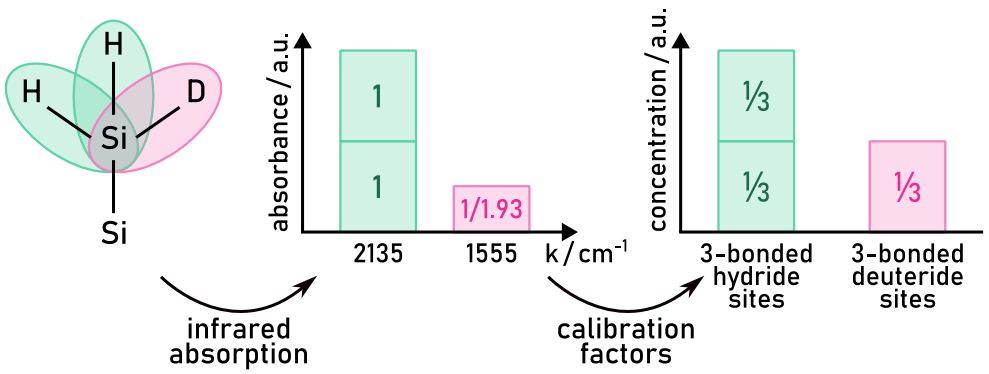

Figure 3.6: Sketch explaining the infrared absorption of a SiH_2D group. The two 3-bonded hydrides absorb one unit of radiation at $2135\,cm^{-1}$ each and the one 3-bonded deuterides absorbs $1/1.93$ units at $1555\,cm^{-1}$ according to the ratio of reduced masses of SiH and SiD. Using calibration factors from literature, this is converted into the concentration of hydride and deuteride sites with 3-bonded hydrides being counted in two parts and 3-bonded deuterides counted in one part.

of a factor of $1/\sqrt{2}$ between vibration frequencies due to the 1:2 mass ratio of H_2 and D_2. The peaks are further differentiated by their number of bonded hydrogen / deuterium atoms. Another distinction can be made depending on their surroundings in the surface or bulk of the material as the vibrational excitation of the bond depends on its surrounding dielectric. A bond on the particle's surface therefore has a narrower response than in its bulk as well as a slightly shifted peak position.

While the excitation frequency of the stretching vibration of individual hydrides or deuterides shifts with the total number of bonded hydrogen (and/or deuterium) atoms to the silicon atom, their oscillator strength is not correlated, i.e., each SiH bond oscillates with independent strength. [23, 24]. Therefore, a single calibration factor $B = 3.83 \cdot 10^3\,L\,cm^{-2}\,mol^{-1}$ can be used to cover all hydrides from SiH to SiH_4 [25]. For SiD bonds, this factor needs to be approximately halved, as the oscillator strength is inversely proportional to the reduced mass $\mu_{SiD} = 1.93\mu_{SiH}$ of the bond. Unfortunately, this calibration factor is not available for species on the particle surface. Lacking this distinction, this work will follow Kessels et al. [23] and apply the same calibration factor for both surface and bulk species.

As the deuterium treatment generates partially deuterated groups, we introduce specific nomenclature to refer to the different groups: A silicon site with a total of n hydrogen and deuterium atoms will be called an *n-bonded* silicon atom[2]. The term *hydride* refers to any silicon group containing hydrogen, while *deuteride* refers to silicon groups containing deuterium. This means that, e.g. an SiH_2D group can be referred to as both a 3-bonded hydride and a 3-bonded deuteride,

Table 3.2: Assignment of absorption peak positions $\bar{\nu}$ and widths σ to silicon absorption lines. Hydrides and deuterides both on the particle surface and in bulk material assigned following Agarwal et al. [20]. Asymmetric stretching of Si−O−Si following Kirk and Fidalgo et al. [21, 22].

	Surface		Bulk	
Species	$\bar{\nu}/\mathrm{cm}^{-1}$	σ/cm^{-1}	$\bar{\nu}/\mathrm{cm}^{-1}$	σ/cm^{-1}
Hydride stretching				
SiH	2069–2084	10–20	1995–2002	80–105
SiH_xD_{2-x} $x = 1, 2$	2106–2112	29–35	2095	55–70
SiH_xD_{3-x} $x = 1, 2, 3$	2130–2140	10–30	2135–2140	40–50
SiH_xD_{4-x} $x = 1, 2, 3, 4$	—	—	2170	60
Deuteride stretching				
SiD	1510[a]	10–30[a]	1460–1470	65–70
SiH_xD_{2-x} $x = 0, 1$	1523–1527	23–28	1520	50
SiH_xD_{3-x} $x = 0, 1, 2$	1540–1570	10–20	1550	45
SiH_xD_{4-x} $x = 0, 1, 2, 3$	—	—	1595–1600	30-35
Unassigned			1638	25–35
Si−O−Si asymmetric stretching				
ν_{AS1} LO	—	—	1195–1221	40
ν_{AS2} TO	—	—	1117–1141	40
ν_{AS2} LO	—	—	1187–1109	15
ν_{AS1} TO	—	—	935–1115	50

[a] Agarwal et al. did not observe this peak, but expected it at this position. In this work, the width is assumed following the width of SiH bonds but leaving a slightly wider range of possibilities for the fit.

depending on whether the focus lies on the SiH or SiD bond.

To convert from the absorbance of SiH and SiD bonds in the infrared spectrum to the concentration of hydrogenated or deuterated Si sites, the measured concentration for a given SiH_xD_y hydride needs to be divided by the number $x+y$ of hydrogen and deuterium atoms bonded to a silicon site. Note that these silicon site concentrations can be misleading for partially deuterated silicon atoms. For example the SiH_2D group shown in fig. 3.6 gets counted in two parts towards the 3-bonded hydride and one part towards the 3-bonded deuteride concentration. Furthermore, note that this approach cannot detect pure Si sites, as Si−Si bonds are inactive in the infrared. Therefore the term "hydrogenated (or deuterated) Si site" is used to specifically refer to the measurable quantity.

After oxidation, further Si−O−Si asymmetric stretching absorptions appear in the spectrum and are assigned following the work of Kirk and Fidalgo et al. [21, 22]. This vibrational excitation is split into four separate absorption lines. One splitting occurs as the asymmetric stretching motion of two adjacent oxygen atoms can happen either in phase (ν_{AS1}) or shifted by 180° (ν_{AS2}). Furthermore, the stretching vibration is possible both in longitudinal optical (LO) and transversal optical (TO) mode, coupled to each other through long-range Coulomb interactions. Calibration factors given by Zamchiy et al. [26] are used to convert into absolute concentrations.

3.2 Particle extraction

To perform ex situ measurements of the nanoparticles created in the system, an extraction setup is necessary. The simplest way of extracting particles is by placing a sample (e.g. a silicon wafer) on the bottom electrode and turning off the plasma. Without the electrostatic confinement forces, the particles fall onto the bottom electrode and can be then be removed by opening up the vacuum chamber and taking out the sample. This was done, e.g. by Groth et al. [27] to obtain reference particle sizes. This method has the disadvantage of disrupting the plasma discharge as well as the vacuum system and therefore making multiple measurements of a single treatment cycle very difficult. The experiment needs to be repeated for each extraction and the initial conditions need to be kept the same to ensure repeatability. Furthermore, when using an isolating material residual charges on the sample can repel the charged particles, leading to an uneven coverage of the sample.

Other prior works used the thermophoretic force by a cooled probe [28], the drag from a neutral gas flow [29] or the electrostatic force through biased substrates [30] to directly attract particles onto a substrate for extraction. Similarly,

[2] In the existing literature, authors avoid directly referring to this number and typically write of mono-, di-, or tri-hydrides. For the sake of brevity as well as precision (as this work examines both hydrides and deuterides that can even be in overcoordinated or interstitial 4-bonded states), I decided to introduce the term "n-bonded" to describe this property instead.

during the course of her master's thesis, Maren Dworschak [31, 32] has built the electrostatic particle extractor (EPEX), which uses an electrostatic pulse extract the charged particles from the plasma volume (see fig. 3.7a). The EPEX consists of an octagon wheel, where up to 8 samples can be placed. The samples are held in place by a metallic front plate, onto which a voltage pulse is applied. Typical extractions of large nanoparticles with a diameter of 100 nm use a voltage of −170 V applied for 200 ms. The octagon wheel can be rotated from outside the vacuum vessel via a rotary vacuum feedthrough that is connected to a chain transmission. This way, up to 8 samples can be extracted before the vacuum needs to be broken to retrieve the samples.

It was shown that the EPEX presents a minimally invasive method as the electrostatic pulse only briefly interferes with the plasma [32]. Therefore, multiple samples can be extracted from the same particle cloud during a single plasma treatment. The only limiting factor is the amount of particles extracted with each sample, as the particle density should not be allowed to drop significantly through the extraction. This ensures comparability of the different samples and allows closely measuring the impact of various treatments such as growth processes or particle surface treatments.

The EPEX was used for extracting the particles in the carbon nanoparticle experiments, whereas the silver-silicon core-shell particles were extracted using a simpler holder with only one sample as the adapter to connect the EPEX to a CF63 flange was not ready in time for the measurements. The simpler holder consists of a polyether ether ketone (PEEK) block on which a silicon wafer is fixed with a stainless steel plate similar to the EPEX front plates (see fig. 3.7b). This holder has a smaller diameter and fits through a KF40 flange. It is placed on top of a hollow rod with 8 mm diameter in a linear vacuum feedthrough and an electrical vacuum feedthrough on one end for the extraction voltage. A KF40 T-piece was used to create a provisional load lock setup that can be closed off using a gate valve connected to port 3 of the SFB chamber (see fig. 3.10 in section 3.4). The holder is brought near the plasma for extractions and is then pulled out through the load lock, which is then closed off to leave the vacuum undisturbed.

A more advanced version of this sample holder was created in the course of Florian Ziegler's master's thesis [33]. This system allows for either a capacitor stack of two brass rings (see fig. 3.7c) or a single contact holder to be used with special patterned wafers. The brass rings act as an electrostatic lens when a voltage is applied to the bottom ring, while grounding the top ring, guiding the particles to the centre of the circular aperture. The resulting extraction quality can be seen in fig. 3.8. The single contact holder is used with special lithographically patterned wafers with 8 platinum contacts that lead to 10 µm wide legs that meet in the middle in a 30 µm wide gap. Each of the contacts can be addressed separately, allowing to specifically attract incoming particles to each individual leg. First measurements have shown that ground should not be applied to a leg, as the ion bombardment from the plasma leads to significant damaging of the

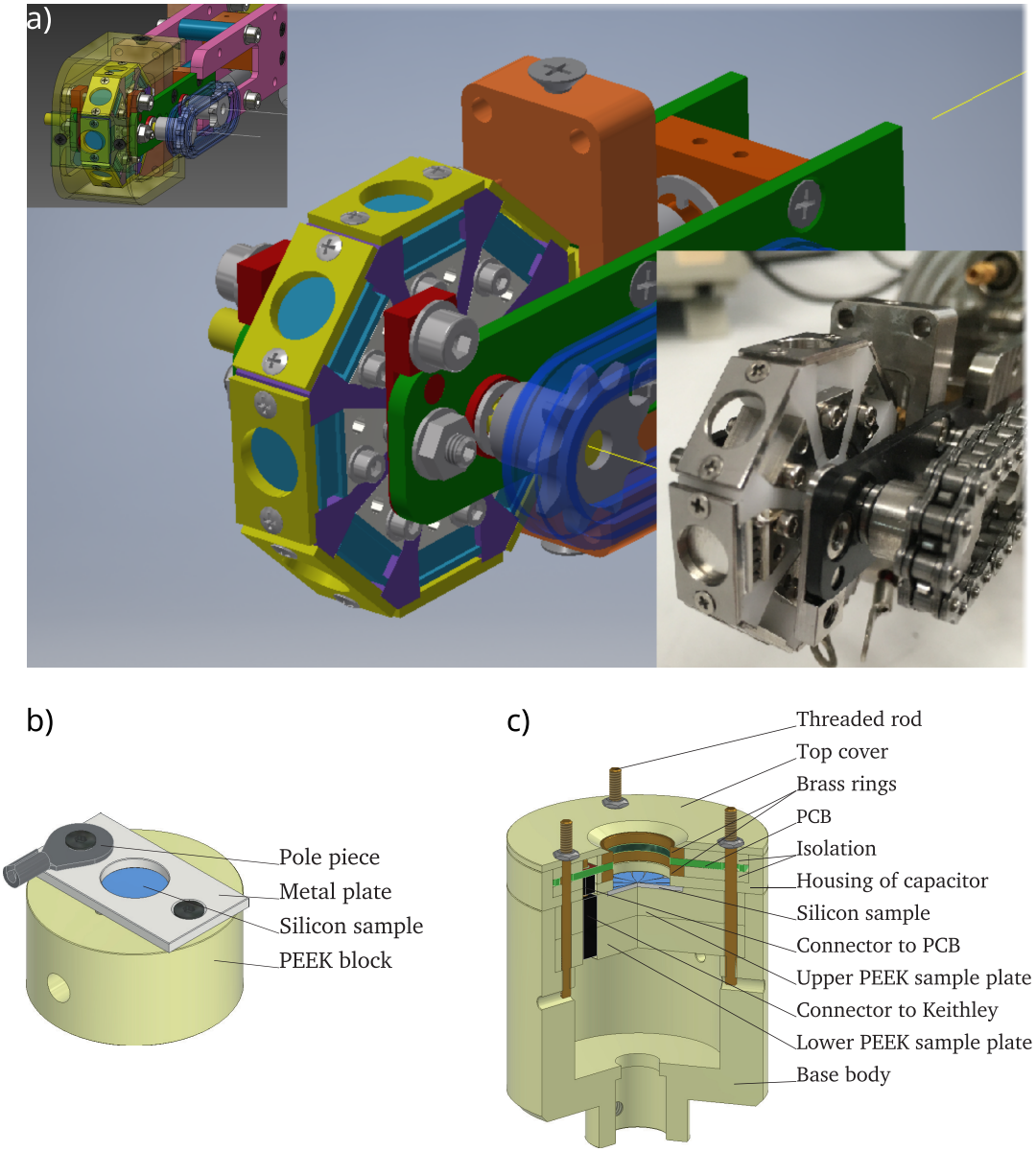

Figure 3.7: a) Sketch of the EPEX. It consists of an octagon wheel with 8 sample holders. A potential is applied to the metal face plates shown in yellow to attract particles onto the sample. Used with permission from [31]. b) Simple provisional holder used for experiments with Ag@SiO_2 particles. Used with permission from [33]. c) Capacitor stack holder with two brass rings. The outer ring is connected to ground potential while the other ring is on the extraction potential to create a lens effect, focusing particles on the centre of the sample. Used with permission from [33].

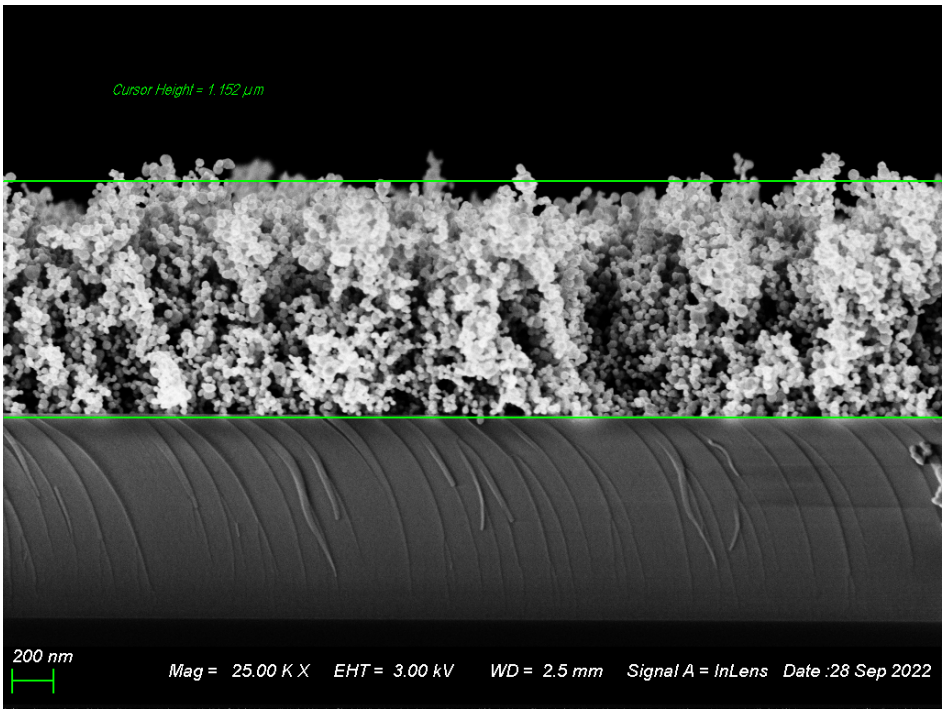

Figure 3.8: Side-on scanning electron microscopy (SEM) image of a wafer coated with the capacitor stack arrangement. Particles were produced by injecting silver particles for 60 s and then coating them with 60 s of 20 sccm Ar/SiH_4(0.01 %). A layer of Ag@SiO_2 particles of over 1 µm thickness can be seen on top of the wafer. Extraction was performed 10 pulses each of −170 V and 200 µs and the entire process was repeated a total of six times. The sample was created by Florian Ziegler in the course of his master's thesis and SEM micrograph was taken by Alexander Vahl.

structures on the wafer. Instead, legs not be coated with particles should be left at floating potential, whereas a negative voltage is applied to the other legs to achieve a good coating. More details on this extraction process can be found in Florian Ziegler's master's thesis [33].

3.3 Carbon experiments: Suleika

Before beginning work on an entirely new chamber setup that will be described in the next section, the Suleika Nano[3] chamber was used as a well-characterised system to gain experience using the multi-pass infrared setup. The goal of the experiments was to investigate the mass loss during plasma exposure that was known from previous works on both microparticles [34–37] and nanoparticles [27].

The chamber is cylindrical stainless steel vessel with a height of 200 mm and a diameter of 147 mm (see fig. 3.9). It has four access ports on its sides that can be equipped with windows or adapters for different applications. In this work, two opposing ports were used for the multi-pass cell. With a port distance of

[3] **SU**pra**LEI**tender-Magnet-**KA**mmer zur Untersuchung von **NANO**staub

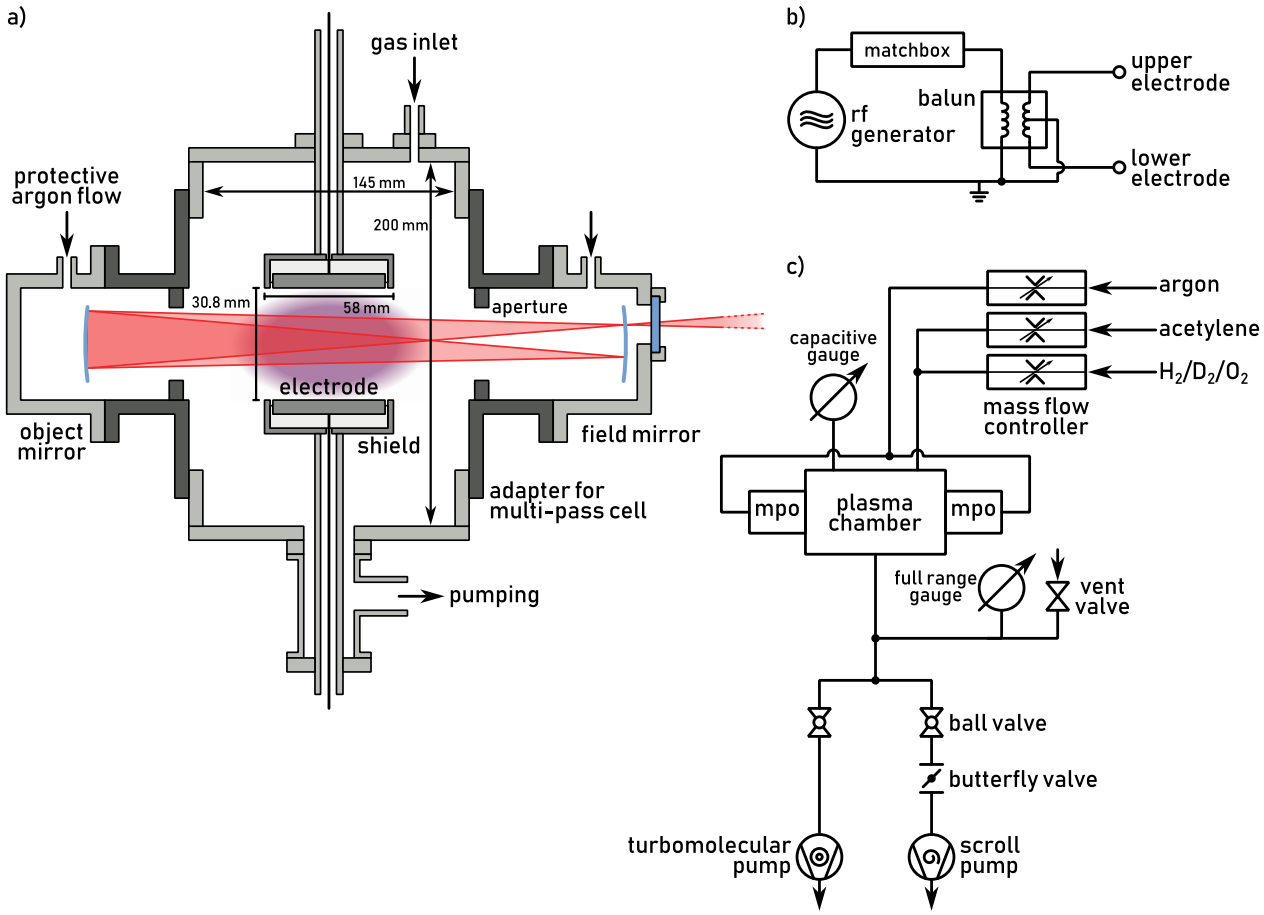

Figure 3.9: a) Side-view sketch of the Suleika chamber. The multi-pass cell is mounted on two opposing ports of the chamber with gas inlets for the protective argon flow. The infrared beam path is shown in red. An adapter is needed to reach the necessary flange distance for the multi-pass cell. Electrodes are mounted with vacuum feedthroughs and consist of a grounded shield and a driven electrode. Reactive gasses are injected through the gas inlet on the top of the chamber. Pumping is done at the bottom electrode feedthrough to ensure a symmetric gas flow. b) Sketch of the electrical setup. The RF power is coupled through a matchbox for impedance matching into a balun (balanced-unbalanced). This creates two RF voltages with 180° phase difference, which are fed into the upper and lower electrode. c) Sketch of the vacuum setup. Argon is let in through the multi-pass optics (mpo), while the reactive gasses use the separate inlet on the top of the chamber. Both flows are controlled through mass flow controllers. The pressure in the chamber is measured with a capacitive gauge. Pumping is done via two pumps, which are each connected through a ball valve: a turbomolecular pump for use without nanoparticles and a scroll pump, which can be regulated using a butterfly valve. An additional full range pressure gauge and a vent valve is located near the pumping.

173 mm, the Suleika chambers are smaller than the SFB chamber for which the multi-pass cell was designed. An additional adapter flange was used to reach the necessary flange distance of 283.3 mm needed for the multi-pass cell. An aperture was mounted inside the adapter flange to confine the plasma inside the chamber and further protect the windows from damage.

The electrodes are mounted using vacuum feedthroughs on the top and bottom flange. They consist of a circular plate with a diameter of 58 mm inside of a grounded shield. Electrode and shield are isolated from each other with a Macor holder. The electrode gap is set to 30.8 mm to avoid parasitic discharges towards the chamber walls.

A port on the top flange is used to let in the process gasses argon and acetylene via mass flow controllers (MFCs). Two vacuum pumps are connected laterally on the bottom feedthrough to pump the system. This placement ensures that the gas flow is symmetrical around the bottom electrode, largely avoiding asymmetrical forces on the dust cloud. A turbomolecular pump Pfeiffer HiPace 80 with a diaphragm pre-pump is used for continuous pumping of the chamber outside of nanoparticle operation reaching a final pressure in the order of 10^{-1} Pa. During nanoparticle generation, a scroll pump Edwards 6i is used instead with a final pressure of 3 Pa. This pump can be throttled using a butterfly valve for setting the desired pressure while keeping gas flows constant. The pressure is measured with a Pfeiffer Vacuum PKR 251 compact full range gauge located near the pumps and a Pfeiffer Vacuum CMR 263 capacitive gauge located near the chamber.

The RF power is supplied by a Coaxial Power RFG300-13 power generator at 13.56 MHz connected via a matching network MMN300-13 for impedance matching. A balun (**bal**anced to **un**balanced, 1:1 transformer) is used to generate two RF voltages with 180° phase difference to operate the electrodes in a push-pull mode. The centre connector of the secondary coil is grounded so that both voltages are symmetric with respect to ground. The power was set to 5 W for all experiments.

3.4 Silicon experiments: SFB chamber with external ccp source

After the proof of principle measurements with the Suleika chamber, the setup was completely reworked to use the ultra-high vacuum capable SFB chamber[4]. The SFB chamber is a cylindrical vessel with an inner diameter of 200 mm and several welded-on access ports on its sides for various uses (see fig. 3.10). In its configuration for this work, ports 5 and 6 are used for the multi-pass setup previously described in section 3.3. The vacuum system consists of a turbomolecular pump Pfeiffer HiPace 80 attached at port 4 and a rotary vane pump Pfeiffer Duo 030A attached at port 8. While the system was never operated at ultra-high

[4]Short for *silicon forming box*, a backronym as a throwback to the rejected collaborative research centre (*Sonderforschungsbereich*) that it was initially built for.

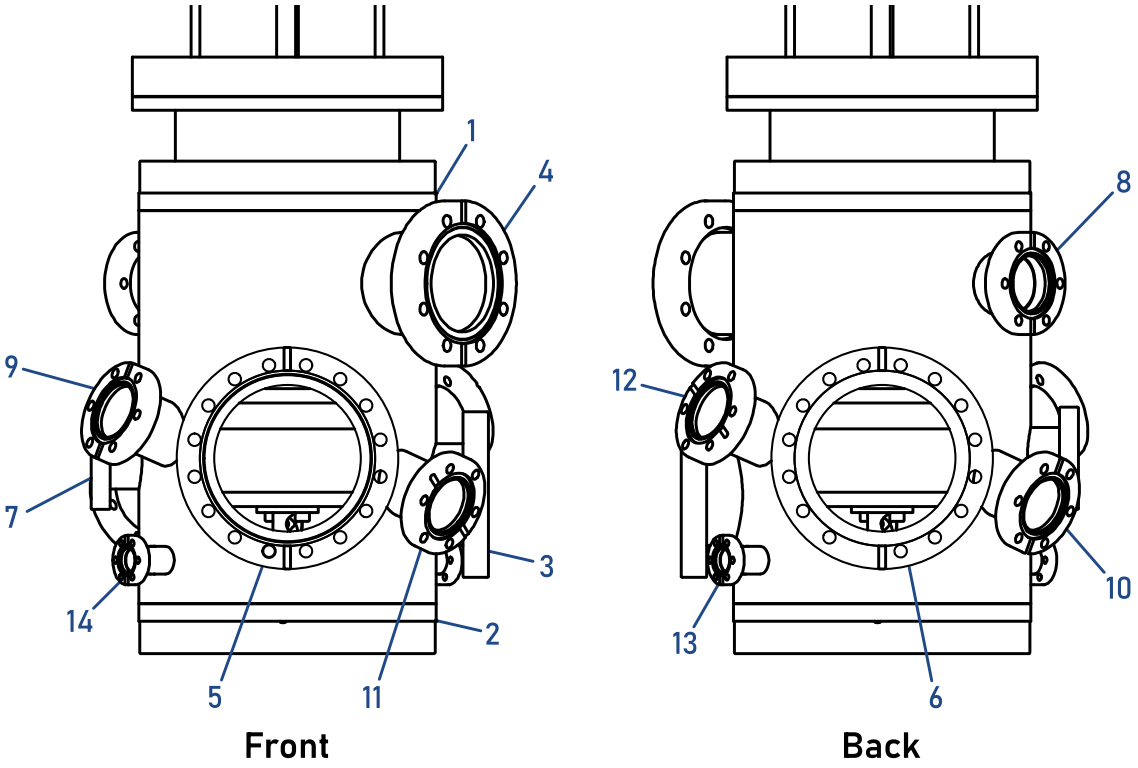

Figure 3.10: Front and back view sketch of the SFB chamber with all available ports labelled with numbers for referencing.

vacuum because of the use of Viton seals in several ISO-KF flanges for easier configurability, base pressures of $3 \cdot 10^{-5}$ Pa are achieved using the turbomolecular pump. During experiments, only the rotary vane pump is used to prevent nanoparticles contaminating the turbomolecular pump.

The bottom electrode is a stainless steel plate with a diameter of 142 mm and a thickness of 10 mm mounted via a connecting piece on a large M8 threaded rod. For experiments with a driven bottom electrode, the connecting piece is replaced with a MACOR ceramic piece for isolation from the grounded rod and a hole for connecting the driving voltage is placed on the electrode. This allows for another option of using the grounded electrode together with a vertically mounted isolated metal pin to which a direct current (DC) or RF voltage can be applied though a electrical feedthrough at port 14. This was used to bias the plasma potential with respect to ground in an attempt to improve the confinement capabilities of the system. To be able to vary the electrode gap during operation, the direct connection was replaced with a membrane bellow with a stroke of up to 80 mm.

The upper electrode is a copper coil with two windings separated from the vacuum by a glass cylinder which powers an inductively coupled plasma (ICP). While the coil is hollow and can be flushed with air or water cooling, the system is operated at a relatively low maximum power of about 150 W which is sustainable without additional cooling. The position of the upper coil and glass cylinder can be adjusted with three spacers with a thickness of 2×10 mm and 1×30 mm. The typical chamber setup did not use any cylinders and used a bottom electrode

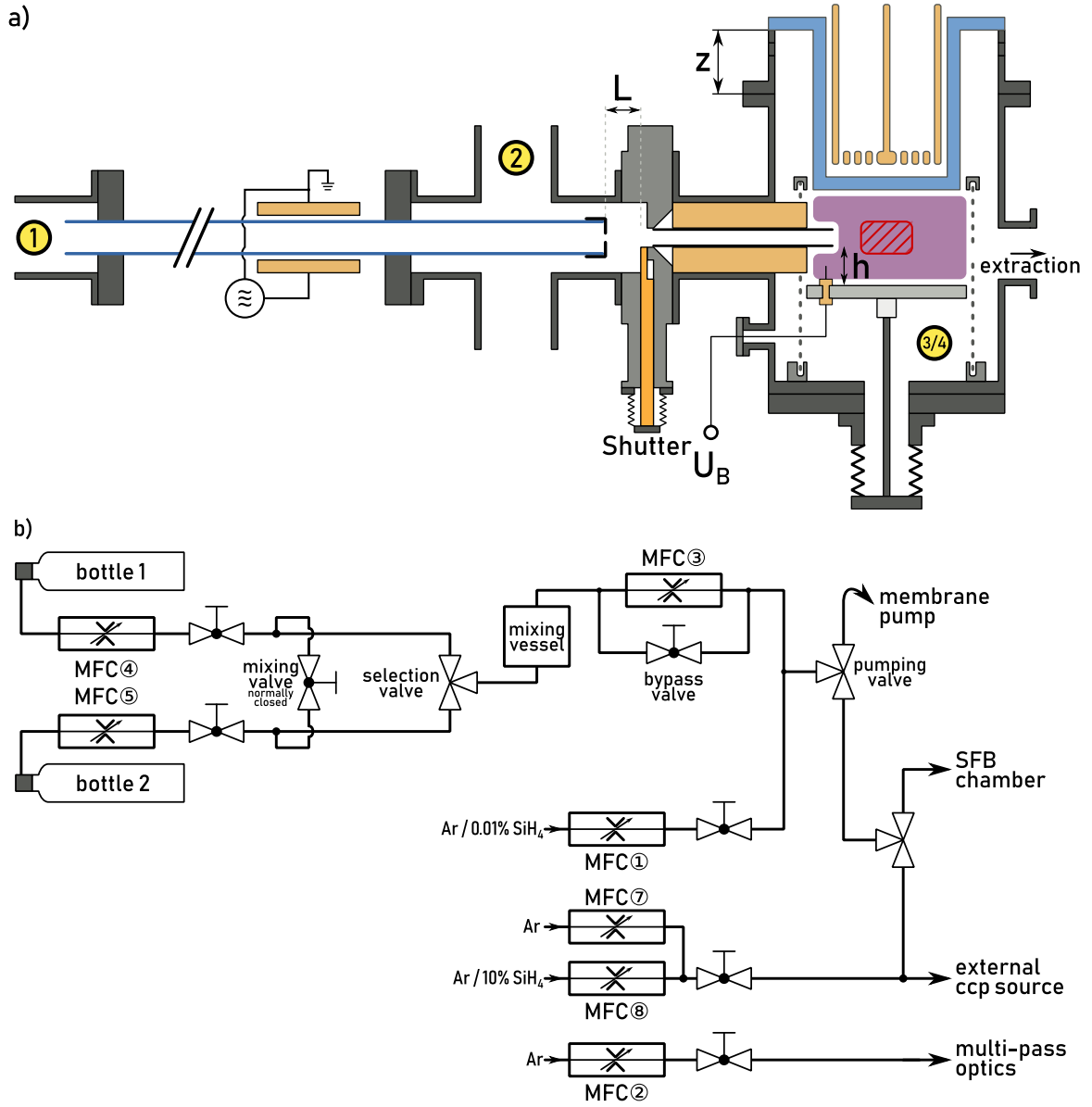

Figure 3.11: a) Cross-sectional side view schematics of the experimental setup using an external CCP particle source. Yellow circles indicate different pressure measurement points. The distance L between glass tube and shutter was typically kept at 10 mm. By using spacers, the distance z can be chosen between 0–50 mm. The height h indicates the distance between the injection tube and the bottom electrode. A bias voltage U_B can be applied to an isolated vertical rod in the bottom electrode. Particles are extracted through a hole in the cage using an electrostatic extractor setup. b) Schematics of the gas setup. Numbers at the MFCs indicate the RS485 address of the controller.

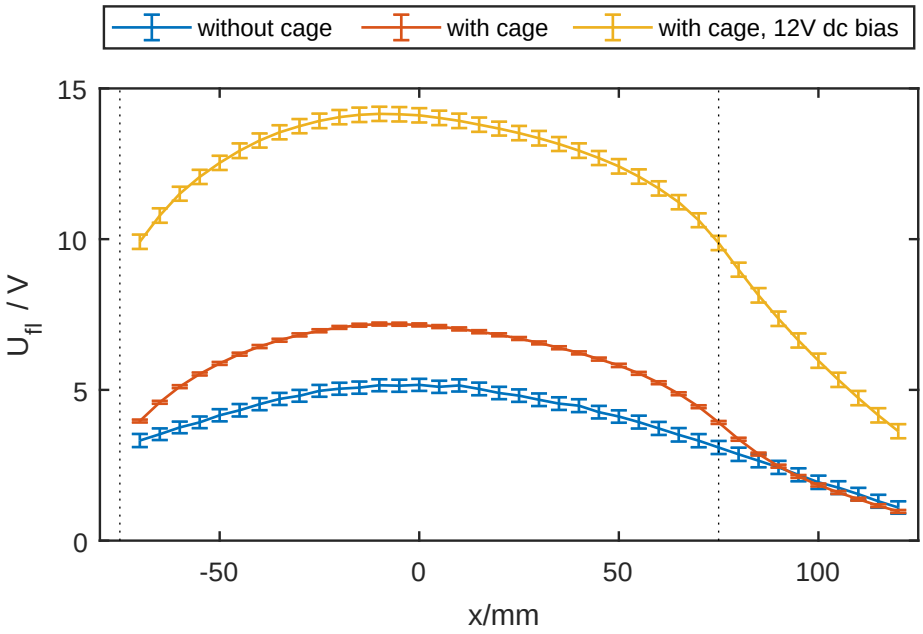

Figure 3.12: Floating potential measurement using a Langmuir probe mounted on a one-dimensional stage. The measurement was taken in the mid-plane between lower and upper electrode and $x = 0$ denotes the centre of the electrode. The stainless steel mesh is located at $x = \pm 75$ mm (shown with dotted lines). The measurement was performed in an argon plasma at a power of 70 W in the H-mode at a pressure of 6.2 Pa. For the third measurement, a DC bias of 12 V was applied to the metal pin in the bottom electrode.

height of 90 mm measured from the bottom of the chamber to the top surface of the electrode, resulting in a distance between bottom electrode and glass cylinder of 43.2 mm.

Initially, particles could only be detected during their fly-through through the beam path with no confinement at all. To improve the confinement properties, the volume between upper and lower electrode was encased in a cylindrical stainless steel mesh cage. The cage sits in a groove on a grounded connector piece mounted on the bottom CF160 flange of the chamber. Later experiments showed that an increased gas pressure of about 50 Pa in the secondary plasma slowed down injected nanoparticles enough to enable confinement as well. Yet, the cage still improved the confinement of particles further and experiments described in this work were performed exclusively using the cage. Measurements without the cage performed in the course of the master's thesis of Arthur Fabritz showed that about 20 % of particles are lost in half an hour of confinement, whereas next to no losses are seen over an hour of confinement with the cage.

The stainless steel mesh has a wire diameter of 0.1 mm and openings of a width of 0.3 mm. The top of the cage is held in its shape by a circular stainless steel part. Four holes are cut out of the mesh, two on opposite sides to allow the beam of the multi-pass cell to pass through, one for the external particle injection and one for particle extractions. One-dimensional Langmuir measurements were performed to verify the improved electric fields for particle confinement. The

floating potential was measured as an indicator of the electric field and showed a significant increase of the electric field around the mesh location (see fig. 3.12). While applying a DC bias to the plasma increases the confining field even further, this step was not needed to confine particles and was not used during the experiments.

An external capacitively coupled plasma (CCP) source is used for the creation of silicon nanoparticles that are injected into the SFB chamber for further controlled treatment. It was built following the work of Müller et al. [38] and Galář et al. [39] from the collaborating Group Silicon Nanophotonics at the Czech Academy of Sciences, describing a flow-through non-thermal plasma reactor for Si and SiC nanoparticles used in photoluminescence experiments. The source consists of a 750 mm long glass tube with an inner diameter of 7 mm and an outer diameter of 10 mm. Two 90 mm × 50 mm copper plates are mounted as electrodes outside the tube for a CCP with one driven and one grounded electrode operated at typical discharge powers between 70–150 W at 13.56 MHz using a Coaxial Power RFG 300-13 with a MMN 300-13 matching network. The electrodes are surrounded by a cage made from two perforated stainless steel sheets to limit electromagnetic radiation with an opening for a large cooling fan to keep the electrode temperature below 70 °C. The tube is mounted via two O-ring sealed glass tube connectors: upstream to the gas inlet and a capacitive pressure gauge Pfeiffer MKS 127AAX with 100 mbar range, downstream over a membrane bellow to a differential pumping stage. Attached on the end of the glass tube is an aperture made from anodised aluminium foil with a central hole of 2 mm diameter. This constricts the gas flow and creates a focused nanoparticle beam. The glass tube is mounted in a system of two x-y and two z-stages with in combination with the membrane bellow allows for precisely adjusting the position and alignment of the particle beam onto the injection aperture of the SFB chamber.

The differential pumping stage is used to independently set the gas pressures in the SFB chamber and the external ccp source. It consists of a cross piece that makes it possible to connect the pump over two flanges on its top and bottom to create a symmetrical gas flow to keep the particle beam straight. A roots pump Edwards EH250 with a rotary vane pre pump E2M40 is connected to the stage and can be throttled via a butterfly valve to set the resulting pressure independently from the chosen gas flows. A capacitive pressure gauge Pfeiffer CMR263 with 10 mbar range is connected at a fifth flange and used for monitoring the gas pressure. Typical pressures were around 500 Pa at the start of the glass tube, 100 Pa at the differential pumping stage and at least 40 Pa inside the SFB chamber during injection to create enough friction with the neutral gas to slow down particles and facilitate confinement.

Hydrogen plays a crucial role in the creation of silicon nanoparticles. It is produced naturally through the dissociation of silane, but can also be additionally admixed to slow down nucleation and achieve higher crystallinity [40, 41]. To check the effect of hydrogen etching on the inside walls of the glass tube of the

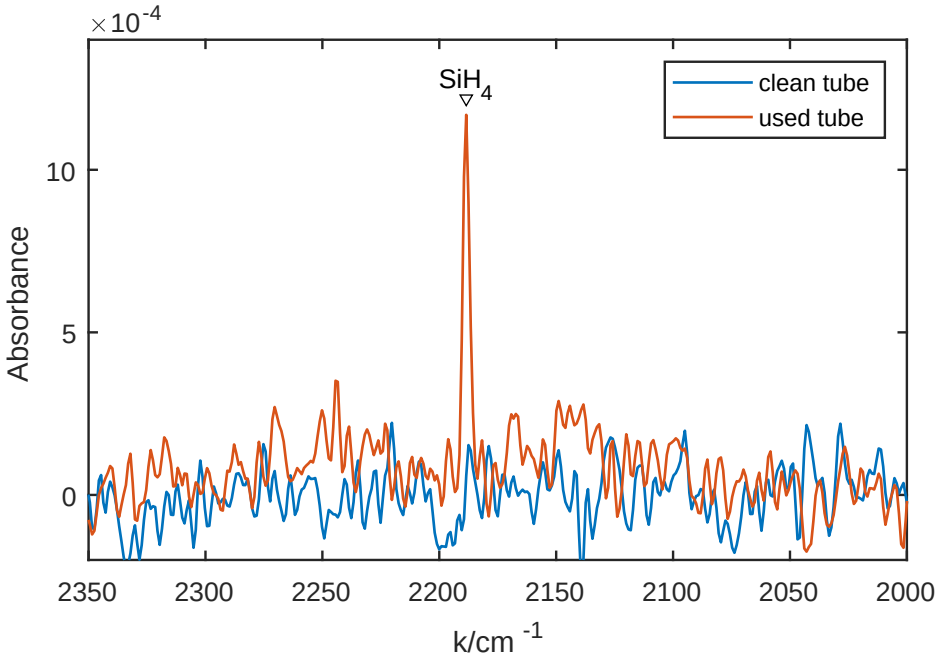

Figure 3.13: Comparison between a used and a clean glass tube of the external ccp source. A flow of 50 sccm H_2 and 90 sccm Ar was used to create a discharge at a pressure of 550 Pa in the external ccp at a power of 150 W. The differential pumping stage was used to pump a large part of the exhaust, leaving a partial pressure of 23 Pa that was injected into the SFB chamber for FTIR analysis.

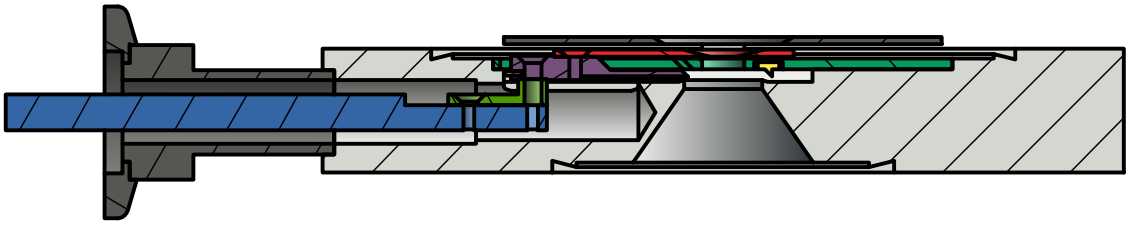

Figure 3.14: Cross-sectional side view sketch of the particle shutter. The mechanism has multiple layers to avoid particle deposition on the sealing surfaces. When the shutter is pushed in, first the cover (red) moves over the aperture, shutting off the particle flow. Then, the plug (violet) pushes against the stop (yellow) and is pressed down on the sealing surface.

external ccp source, comparative measurements between a used and a clean tube were performed. While no difference could be seen on the particles produced in a clean vs a used tube, a small silane signal can be seen in the exhaust of a pure hydrogen discharge in the external ccp (see fig. 3.13).

A shutter connects the differential pumping stage to the SFB chamber (see fig. 3.14). It was built into a standard CF100-CF40 adapter flange with a 6 mm aperture in its centre that can be sealed off with a sliding mechanism. Coming from the opened state, the slider first brings in a cover that protects the sealing surfaces from nanoparticle contamination to then bring in the Viton seal, which is then pressed onto the sealing surface. It is operated using a membrane bellow for

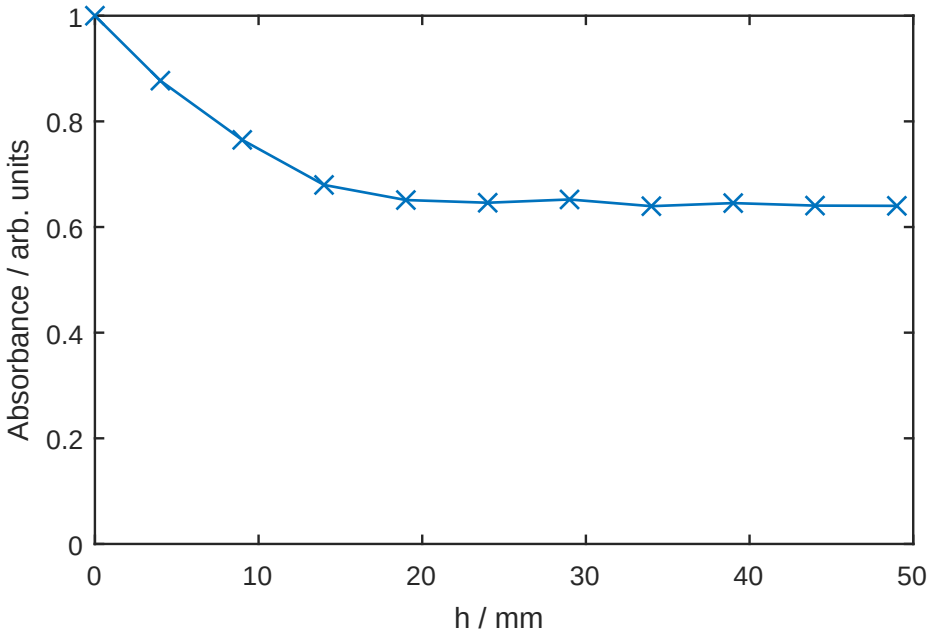

Figure 3.15: Measured integrated absorbance between 950–1300 cm^{-1} of a silicon cloud under variation of the bottom electrode height. The measurement was performed over a period of 10 min starting from $h = 0$ mm. Returning to the initial height after the variation resulted in the same absorbance, confirming that the cloud was confined well throughout the experiment.

linear movement with 3d printed parts for holding the shutter in the fully opened or fully closed position. With the shutter in the closed position, the differential pumping stage can be vented with atmospheric pressure creating only a slight increase of pressure in the SFB chamber under continuous pumping. When the shutter is closed during an experiment, pumping via the differential pumping stage is continued to minimise leaks of ambient air into the SFB chamber.

Three gas inlets bring the necessary process gasses into the system (see fig. 3.11b): one for the external ccp source, one for the protective argon shielding of the multi-pass optics, and one positioned at port 13 of the SFB chamber for the additional gasses. The external ccp source was operated following the procedures given by Müller et al. [38] at a flow of 90 sccm Ar/SiH_4 at a concentration of 1 %. For the protective argon shielding a typical flow of at least 10 sccm of Ar was used. A mixing setup is connected via a switching valve to either the SFB chamber or the external ccp source with two exchangeable gas bottles for Ar, H_2, D_2, O_2, and CH_4. The setup further contains a mixing vessel for preparing very low concentration mixtures of the bottled gasses that can then be used via a separate MFC. When dilution is not needed, a bypass valve allows direct access to the bottled gasses. To avoid the settling period when switching gas flows via MFCs, during experiments, the gas flow was set constant on the respective MFCs with the pumping valve directing the flow towards a separate membrane pump. After settling on a constant flow, the pumping valve was then switched to direct the reactive gasses into the reaction chamber without a drop in flow rate.

The bottom electrode is mounted on a linear movement stage to allow adjusting the electrode height during the experiment. Moving the bottom electrode up increases the absorption measured with FTIR, reaching its maximum when the bottom electrode touches the injection nozzle at $h = 0\,\mathrm{mm}$ (see fig. 3.15). During measurements a height of $h = 35\,\mathrm{mm}$ is used, which places the injection nozzle and multi-pass beam path in the mid-plane of the bottom electrode and the bottom plate of the glass cylinder of the upper coil as shown in fig. 3.11a. While this beam positioning includes the void which can change its size during a measurement, it avoids artefacts from the lower edge of the cloud which can shift in reaction to plasma parameter changes.

As the chamber walls and especially the confinement mesh regularly get coated during treatments, they need to be considered as part of the entire plasma system. Proper conditioning of the chamber is therefore vital for reproducibility of results. One main coating process of the chamber walls and mesh occurs during H_2 and D_2 treatments, where etching of the particles creates SiH_4 which then redeposits silicon layers on the walls. These layers can introduce a contamination to the treatment plasma as Si_xH_y precursors can be re-emitted from the coating layer through ion bombardment [42]. Even further, the silicon layer can oxidise passively after venting with ambient air [43] or actively through small leaks in the system during plasma operation [44], introducing a source of oxygen-containing Si precursors.

A cleaning procedure is done regularly before treatments to control the influence of the walls in the holding chamber. It consists of hydrogen etching followed by in situ particle generation using silane. The hydrogen etching is done using 40 sccm of Ar and 5 sccm of H_2 with the plasma operated in H-mode at 100 W for at least half an hour to etch contaminants off of the electrodes and the confinement mesh. It is followed by injecting 20 sccm of $Ar/SiH_4(2\,\%)$ directly into the holding chamber operated at 60 W in E-mode for at least 15 min, creating and trapping a silicon nanoparticle cloud. These particles act as a sort of getter pump capturing oxygen contaminations in the system. The plasma also deposits a new layer of silicon on the walls, sealing off remaining contaminants. Figure 3.16 shows the absorption spectra of injected particles in a chamber contaminated with D_2 or ambient air in comparison to a chamber after the cleaning procedure.

3.5 Silver-silica experiments: SFB chamber with external GAS

Core-shell particles of organic and inorganic compounds are widely used in biomedicine, catalysis, electronics, drug delivery, and many more fields. They are typically created using a wide variety of physical and chemical methods [45–48]. More recently, non-thermal plasma-based approaches have been explored, as they can yield excellent results at much faster processing times and without the need

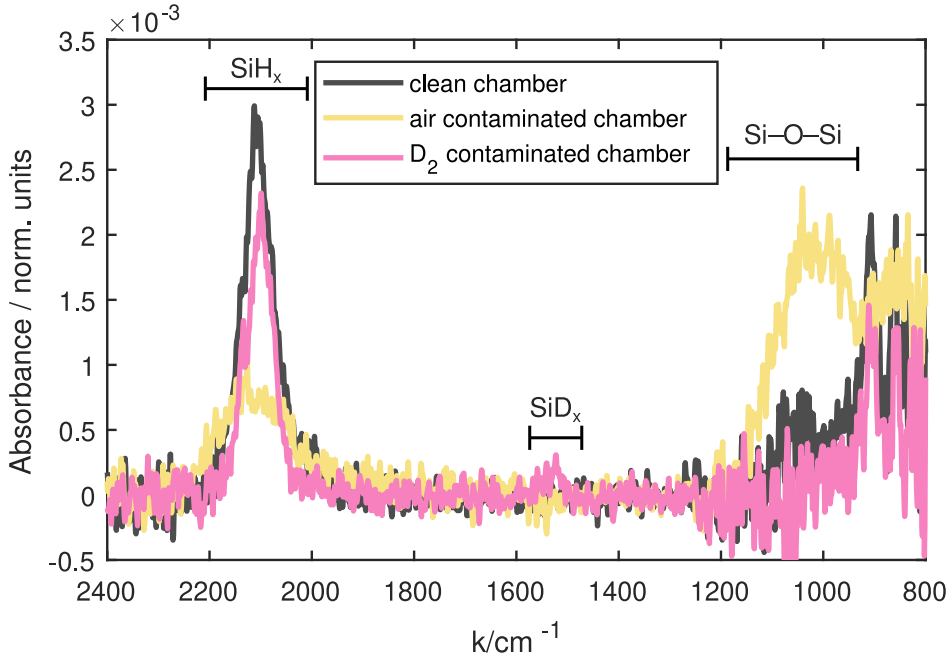

Figure 3.16: Comparison of absorption spectra of silicon nanoparticles injected into a chamber after the cleaning procedure and into contaminated chambers after D_2 and ambient air exposure. All measurements are taken 2 min after particle injection. Absorption lines from SiD and Si−O−Si bonds appear in the contaminated chamber without addition of reactive gasses. Slight oxidation still occurs in the clean chamber but at a significantly lower rate than for the air contaminated chamber.

for any additional chemicals like solvents [49].

For these particles, the setup described in the previous section was converted, replacing the external ccp source with a Haberland-type GAS. This source was extensively characterised and used by Jonas Drewes during his PhD thesis [50–54] prior to the measurements in this work. It consists of a 2-inch height-adjustable water-cooled DC magnetron (IX2U-9A327-02 by Thin Films Consulting) that is powered by an MDX 500 power supply by Advanced Energy. The aggregation length was kept constant throughout the experiments at setting 5. The magnetron discharge was operated in power regulation mode at a power of 100 W. The particles are guided by a feed pipe leading from the aperture of the GAS to 10 mm in front of the 6 mm aperture of the shutter to the SFB chamber. The buffer gas is pumped away in the differential pumping stage while minimising nanoparticle losses over the short distance.

The SFB chamber is prepared with the same preconditioning procedure described in the previous section. Afterwards, it is first pumped using the turbomolecular pump down to a pressure of 10^{-5} Pa to then switch to the rotary valve pump for operation with nanoparticles. During generation, a flow of 160 sccm of Ar was set using a MFC resulting in a pressure of about 170 Pa inside the GAS. Similar to the silicon experiments in the previous chapter, the differential pumping stage allowed controlling the pressure inside the SFB chamber separately.

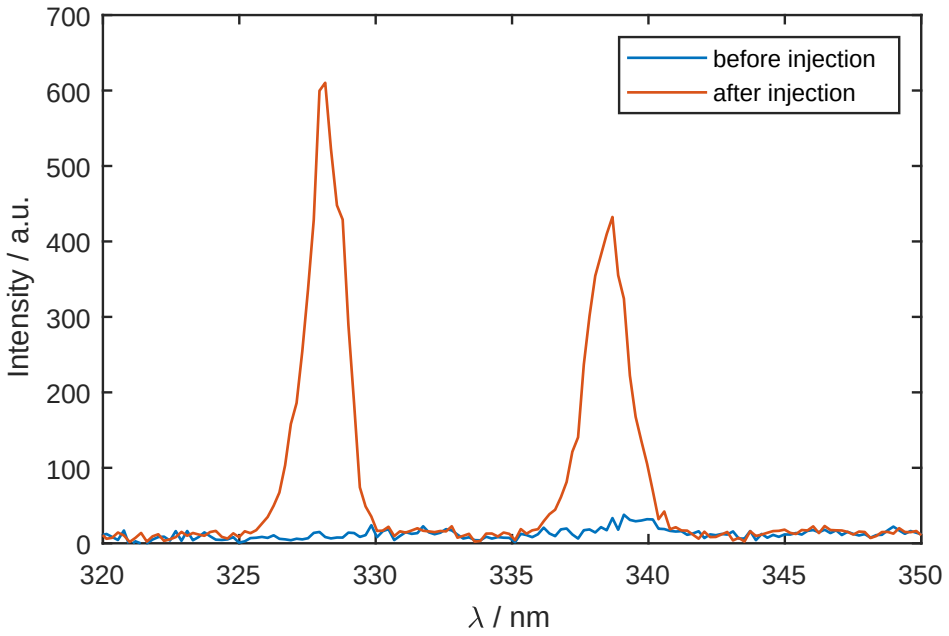

Figure 3.17: Optical emission spectrum of the ICP discharge in H-mode before and after injection of silver nanoparticles from the GAS. Immediately after injection, emission lines of neutral silver appear. The ICP discharge in the SFB chamber was operated at 20 W power.

Particles were confined in the SFB chamber at a pressure of 11 Pa using an Ar flow of 30 sccm. During the creation of a SiO_2-shell, the Ar flow was reduced to 10 sccm with an additional flow of 20 sccm of 0.01 % SiH_4 diluted in Ar. It is important to keep a small Ar flow as it provides the protective gas sheet in front of the multi-pass optics, while the reactive Ar/SiH_4 mixture enters through a different inlet.

The discharge in the SFB chamber is operated at a power of 100 W keeping the plasma in E-mode. While the system was designed for operation in H-mode and it can easily be achieved by adjusting the matching of the system, this leads to an immediate dissociation of the nanoparticles seen through optical emission lines of neutral silver shown in fig. 3.17. A similar experiment injecting silane into the discharge shows no infrared absorption signal as long as the plasma is in H-mode. These findings indicate that energy densities in the ICP discharge are too high for nanoparticles to persist. To avoid the deposition of any further contaminations on the multi-pass optics, no further experiments were performed.

References

[1]J. Bai and J.-P. Wang, "High-magnetic-moment core-shell-type FeCo–Au/Ag nanoparticles", Applied Physics Letters **87**, 152502 (2005).

[2]J. Hanuš, M. Vaidulych, O. Kylián, A. Choukourov, J. Kousal, I. Khalakhan, M. Cieslar, P. Solař, and H. Biederman, "Fabrication of Ni@Ti core–shell nanoparticles by modified gas aggregation source", Journal of Physics D: Applied Physics **50**, 475307 (2017).

[3]O. Polonskyi, A. M. Ahadi, T. Peter, K. Fujioka, J. W. Abraham, E. Vasiliauskaite, A. Hinz, T. Strunskus, S. Wolf, M. Bonitz, H. Kersten, and F. Faupel, "Plasma based formation and deposition of metal and metal oxide nanoparticles using a gas aggregation source", The European Physical Journal D **72**, 10.1140/epjd/e2017-80419-8 (2018).

[4]T. Kretková, J. Hanuš, O. Kylián, P. Solař, M. Dopita, M. Cieslar, I. Khalakhan, A. Choukourov, and H. Biederman, "In-flight modification of Ni nanoparticles by tubular magnetron sputtering", Journal of Physics D: Applied Physics **52**, 205302 (2019).

[5]P. Solař, O. Polonskyi, A. Olbricht, A. Hinz, A. Shelemin, O. Kylián, A. Choukourov, F. Faupel, and H. Biederman, "Single-step generation of metal-plasma polymer multicore@shell nanoparticles from the gas phase", Scientific Reports **7**, 10.1038/s41598-017-08274-6 (2017).

[6]H. Libenská, J. Hanuš, T. Košutová, M. Dopita, O. Kylián, M. Cieslar, A. Choukourov, and H. Biederman, "Plasma-based synthesis of iron carbide nanoparticles", Plasma Processes and Polymers **17**, 2000105 (2020).

[7]O. Asnaz, *FTIR Suite Git repository*, (2020) https://cau-git.rz.uni-kiel.de/ieap/plasma/exp/members/asnaz_oguz_han/ftir (visited on 2023-07-07).

[8]J. Robertson, "Diamond-like amorphous carbon", Materials Science and Engineering: R: Reports **37**, 129–281, ISSN: 0927-796X (2002).

[9]B. Dischler, A. Bubenzer, and P. Koidl, "Bonding in hydrogenated hard carbon studied by optical spectroscopy", Solid State Communications **48**, 105–108 (1983).

[10]A. S. Wexler, "Integrated Intensities of Absorption Bands in Infrared Spectroscopy", Applied Spectroscopy Reviews **1**, 29–98, ISSN: 0570-4928 (1967).

[11]G. Socrates, *Infrared and Raman Characteristic Group Frequencies, Tables and Charts*, 3rd ed. (Wiley, Chichester, 2001), ISBN: 978-0-470-09307-8.

[12]M. L. Theye, V. Paret, and A. Sadki, "Relations between the deposition conditions, the microstructure and the defects in PECVD hydrogenated amorphous carbon films; influence on the electronic density of states", Diamond and Related Materials **10**, 182–190, ISSN: 0925-9635 (2001).

[13]NIST Mass Spectrometry Data Center and William E. Wallace, director, "Infrared Spectra", in *NIST Chemistry WebBook, NIST Standard Reference Database Number 69*, edited by P. J. Linstrom and W. G. Mallard (2023).

[14]A. S. Wexler, "Infrared determination of structural units in organic compounds by integrated intensity measurements: Alkanes, alkenes and monosubstituted alkyl benzenes", Spectrochimica Acta **21**, 1725–1742, ISSN: 0371-1951 (1965).

[15]J. Ristein, R. T. Stief, L. Ley, and W. Beyer, "A comparative analysis of a-C:H by infrared spectroscopy and mass selected thermal effusion", Journal of Applied Physics **84**, 3836–3847, ISSN: 0021-8979 (1998).

[16]W. Jacob and W. Möller, "On the structure of thin hydrocarbon films", Applied Physics Letters **63**, 1771–1773, ISSN: 0003-6951 (1993).

[17]A. Grill and V. Patel, "Characterization of diamondlike carbon by infrared spectroscopy?", Applied Physics Letters **60**, 2089–2091, ISSN: 0003-6951 (1992).

[18]G. D. Ventura, F. Radica, F. Bellatreccia, A. Cavallo, F. Capitelli, and S. Harley, "Quantitative analysis of H2O and CO2 in cordierite using polarized FTIR spectroscopy", Contributions to Mineralogy and Petrology **164**, 881–894 (2012).

[19]M. Buback, J. Schweer, and H. Tups, "Infrared Spectrum of Pure Fluid Carbon Monoxide", Zeitschrift für Naturforschung A **42**, 267–271 (1987).

[20]S. Agarwal, A. Takano, M. C. M. van de Sanden, D. Maroudas, and E. S. Aydil, "Abstraction of atomic hydrogen by atomic deuterium from an amorphous hydrogenated silicon surface", The Journal of Chemical Physics **117**, 10805–10816 (2002).

[21]C. T. Kirk, "Quantitative analysis of the effect of disorder-induced mode coupling on infrared absorption in silica", Physical Review B **38**, 1255–1273 (1988).

[22]A. Fidalgo and L. M. Ilharco, "The defect structure of sol-gel-derived silica / polytetrahydrofuran hybrid films by FTIR", Journal of Non-Crystalline Solids **283**, 144–154, ISSN: 0022-3093 (2001).

[23]W. M. M. Kessels, D. C. Marra, M. C. M. van de Sanden, and E. S. Aydil, "In situ probing of surface hydrides on hydrogenated amorphous silicon using attenuated total reflection infrared spectroscopy", Journal of Vacuum Science & Technology A: Vacuum, Surfaces, and Films **20**, 781–789, ISSN: 0734-2101 (2002).

[24]M. H. Brodsky, M. Cardona, and J. J. Cuomo, "Infrared and Raman spectra of the silicon-hydrogen bonds in amorphous silicon prepared by glow discharge and sputtering", Physical Review B **16**, 3556–3571, ISSN: 0163-1829 (1977).

[25]H. Shanks, C. J. Fang, L. Ley, M. Cardona, F. J. Demond, and S. Kalbitzer, "Infrared Spectrum and Structure of Hydrogenated Amorphous Silicon", physica status solidi (b) **100**, 43–56 (1980).

[26]A. O. Zamchiy, E. A. Baranov, I. E. Merkulova, S. Y. Khmel, and E. A. Maximovskiy, "Determination of the oxygen content in amorphous SiOx thin films", Journal of Non-Crystalline Solids **518**, 43–50, ISSN: 0022-3093 (2019).

[27]S. Groth, F. Greiner, B. Tadsen, and A. Piel, "Kinetic Mie ellipsometry to determine the time-resolved particle growth in nanodusty plasmas", Journal of Physics D: Applied Physics **48**, 465203, ISSN: 0022-3727 (2015).

[28]C. Godde, J. Berndt, E. Kovacevic, I. Stefanovic, J. Winter, and L. Boufendi, "Controlled Sampling of Nanoparticles in Reactive Plasmas", IEEE Transactions on Plasma Science **39**, 2766–2767 (2011).

[29]A. M. Hinz, E. von Wahl, F. Faupel, T. Strunskus, and H. Kersten, "Versatile particle collection concept for correlation of particle growth and discharge parameters in dusty plasmas", Journal of Physics D: Applied Physics **48**, 055203 (2015).

[30]Z. Marvi, E. von Wahl, T. Trottenberg, and H. Kersten, "Spatiotemporal sampling of growing nanoparticles in an acetylene plasma", Journal of Applied Physics **127**, 10.1063/5.0002951 (2020).

[31]M. Dworschak, "Minimalinvasive Extraktion zur Ex-situ-Analyse von Nanopartikeln aus reaktiven Plasmen", MA thesis (Christian-Albrechts-Universität zu Kiel, 2020).

[32]M. Dworschak, O. Asnaz, and F. Greiner, "A minimally invasive electrostatic particle extractor for nanodusty plasmas and its application for the verification of in situ Mie polarimetry", Plasma Sources Science and Technology **30**, 035011, ISSN: 0963-0252 (2021).

[33]F. Ziegler, "In-Flight Trapping of Metal Nanoparticles and Formation of Core-Shell Nanoparticles", MA thesis (Kiel University, 2022).

[34]G. H. P. M. Swinkels, E. Stoffels, W. W. Stoffels, N. Simons, G. M. W. Kroesen, and F. J. de Hoog, "Treatment of dust particles in an RF plasma monitored by Mie scattering rotating compensator ellipsometry", Pure and Applied Chemistry **70**, 1151–1156, ISSN: 1365-3075 (1998).

[35]J. Carstensen, H. Jung, F. Greiner, and A. Piel, "Mass changes of microparticles in a plasma observed by a phase-resolved resonance method", Physics of Plasmas **18**, 033701, ISSN: 1070-664X (2011).

[36]J. Carstensen, F. Haase, H. Jung, B. Tadsen, S. Groth, F. Greiner, and A. Piel, "Probing the Plasma Sheath by the Continuous Mass Loss of Microparticles", IEEE Transactions on Plasma Science **41**, 764–768, ISSN: 0093-3813 (2013).

[37]O. Asnaz, H. Jung, F. Greiner, and A. Piel, "Size and density evolution of a single microparticle embedded in a plasma", Physics of Plasmas **24**, 083701, ISSN: 1070-664X (2017).

[38]M. Müller, P. Galář, J. Stuchlík, J. Kočka, J. Kupka, and K. Kůsová, "Synthesis and surface modification of light emitting silicon nanoparticles using nonthermal plasma techniques", The European Physical Journal Applied Physics **89**, 20401 (2020).

[39]P. Galář, J. Stuchlík, M. Müller, J. Kočka, and K. Kůsová, "Highly spherical SiC nanoparticles grown in nonthermal plasma", Plasma Processes and Polymers **19**, 2100127 (2021).

[40]G. Dingemans, M. N. van den Donker, D. Hrunski, A. Gordijn, W. M. M. Kessels, and M. C. M. van de Sanden, "The atomic hydrogen flux to silicon growth flux ratio during microcrystalline silicon solar cell deposition", Applied Physics Letters **93**, 111914 (2008).

[41]O. Yasar-Inceoglu, T. Lopez, E. Farshihagro, and L. Mangolini, "Silicon nanocrystal production through non-thermal plasma synthesis: a comparative study between silicon tetrachloride and silane precursors", Nanotechnology **23**, 255604 (2012).

[42]M. Mikikian, S. Labidi, E. von Wahl, J. F. Lagrange, T. Lecas, V. Massereau-Guilbaud, I. Géraud-Grenier, E. Kovacevic, J. Berndt, H. Kersten, and T. Gibert, "Optical diagnostics of dusty plasmas during nanoparticle growth", Plasma Physics and Controlled Fusion **59**, 014034 (2016).

[43]C. H. Choi, D.-J. Liu, J. W. Evans, and M. S. Gordon, "Passive and Active Oxidation of Si(100) by Atomic Oxygen: A Theoretical Study of Possible Reaction Mechanisms", Journal of the American Chemical Society **124**, 8730–8740, ISSN: 0002-7863 (2002).

[44]S. Taylor, J. F. Zhang, and W. Eccleston, "A review of the plasma oxidation of silicon and its applications", Semiconductor Science and Technology **8**, 1426–1433, ISSN: 0268-1242 (1993).

[45]R. G. Chaudhuri and S. Paria, "Core/Shell Nanoparticles: Classes, Properties, Synthesis Mechanisms, Characterization, and Applications", Chemical Reviews **112**, 2373–2433 (2011).

[46]M. B. Gawande, A. Goswami, T. Asefa, H. Guo, A. V. Biradar, D.-L. Peng, R. Zboril, and R. S. Varma, "Core–shell nanoparticles: synthesis and applications in catalysis and electrocatalysis", Chemical Society Reviews **44**, 7540–7590 (2015).

[47]V. Chiozzi and F. Rossi, "Inorganic–organic core/shell nanoparticles: progress and applications", Nanoscale Advances **2**, 5090–5105 (2020).

[48]Z. Mahdavi, H. Rezvani, and M. K. Moraveji, "Core–shell nanoparticles used in drug delivery-microfluidics: a review", RSC Advances **10**, 18280–18295 (2020).

[49]O. Yasar-Inceoglu, L. Zhong, and L. Mangolini, "Core/shell silicon/polyaniline particles via in-flight plasma-induced polymerization", Journal of Physics D: Applied Physics **48**, 314009 (2015).

[50]D. Nikitin, J. Hanuš, S. Ali-Ogly, O. Polonskyi, J. Drewes, F. Faupel, H. Biederman, and A. Choukourov, “The evolution of Ag nanoparticles inside a gas aggregation cluster source”, Plasma Processes and Polymers **16**, 1900079 (2019).

[51]A. Shelemin, P. Pleskunov, J. Kousal, J. Drewes, J. Hanuš, S. Ali-Ogly, D. Nikitin, P. Solař, J. Kratochvíl, M. Vaidulych, M. Schwartzkopf, O. Kylián, O. Polonskyi, T. Strunskus, F. Faupel, S. V. Roth, H. Biederman, and A. Choukourov, “Nucleation and Growth of Magnetron-Sputtered Ag Nanoparticles as Witnessed by Time-Resolved Small Angle X-Ray Scattering”, Particle & Particle Systems Characterization **37**, 1900436 (2019).

[52]J. Drewes, A. Vahl, N. Carstens, T. Strunskus, O. Polonskyi, and F. Faupel, “Enhancing composition control of alloy nanoparticles from gas aggregation source by in operando optical emission spectroscopy”, Plasma Processes and Polymers **18**, 2000208 (2020).

[53]J. Drewes, S. Ali-Ogly, T. Strunskus, O. Polonskyi, H. Biederman, F. Faupel, and A. Vahl, “Impact of argon flow and pressure on the trapping behavior of nanoparticles inside a gas aggregation source”, Plasma Processes and Polymers **19**, 2100125 (2021).

[54]J. Drewes, S. Rehders, T. Strunskus, H. Kersten, F. Faupel, and A. Vahl, “In Situ Laser Light Scattering for Temporally and Locally Resolved Studies on Nanoparticle Trapping in a Gas Aggregation Source”, Particle & Particle Systems Characterization **39**, 2200112 (2022).

4

Synthesis and treatment of nanoparticles

In this section, the results from three experiments are described, where different synthesis setups are used to create carbon and silicon nanoparticles, as well as core-shell silver-silica nanoparticles. All experiments have in common that a holding plasma is being used to confine particles using the electrostatic forces acting on them in the plasma environment (see section 2.2.2). This allows for very long confinement durations in the order of hours, during which treatments can be performed and monitored using, e.g. infrared absorption spectroscopy with a time resolution in the range of several measurements per minute.

In the carbon nanoparticle experiments, the generation happens in situ in the holding plasma, as is common for the type of dusty plasma laboratory experiment that is being investigated. The second set of experiments are performed using an external capacitively coupled plasma (CCP) setup to generate silicon nanoparticles that are then injected into the holding plasma for further treatment and monitoring. Finally, in the third experiment, a similar approach is used but replacing the CCP with a magnetron-based gas aggregation source (GAS). This source is capable of creating noble metal particles, in this case silver, which are then coated with SiO_2 in a secondary step in the holding plasma.

4.1 Carbon nanoparticles

Carbon nanoparticles in dusty plasmas have been a powerful test bed for a wide range of basic research topics investigating growth processes [1–4], wave phenomena [5–7] or the influence of magnetic fields [8, 9]. As the precision of measurement methods increased, the stability of particles during plasma exposure was put in question. Previous works on both microparticles [10–13] and nanoparticles [14] report a loss of particle mass over time. One possible cause of this was theorised to be reactive sputtering through small oxygen leaks [12], as the experiments are rarely performed under ultra-high vacuum conditions and often have a considerable amount of oxygen still present in the system. Another possibility are impinging ions from the discharge, leading to melting-like processes on the particle surface [13, 15]. The goal in this section is to determine the source of changes to carbon nanoparticles confined in a plasma under typical laboratory conditions. The experiments are performed in the Suleika chamber described in

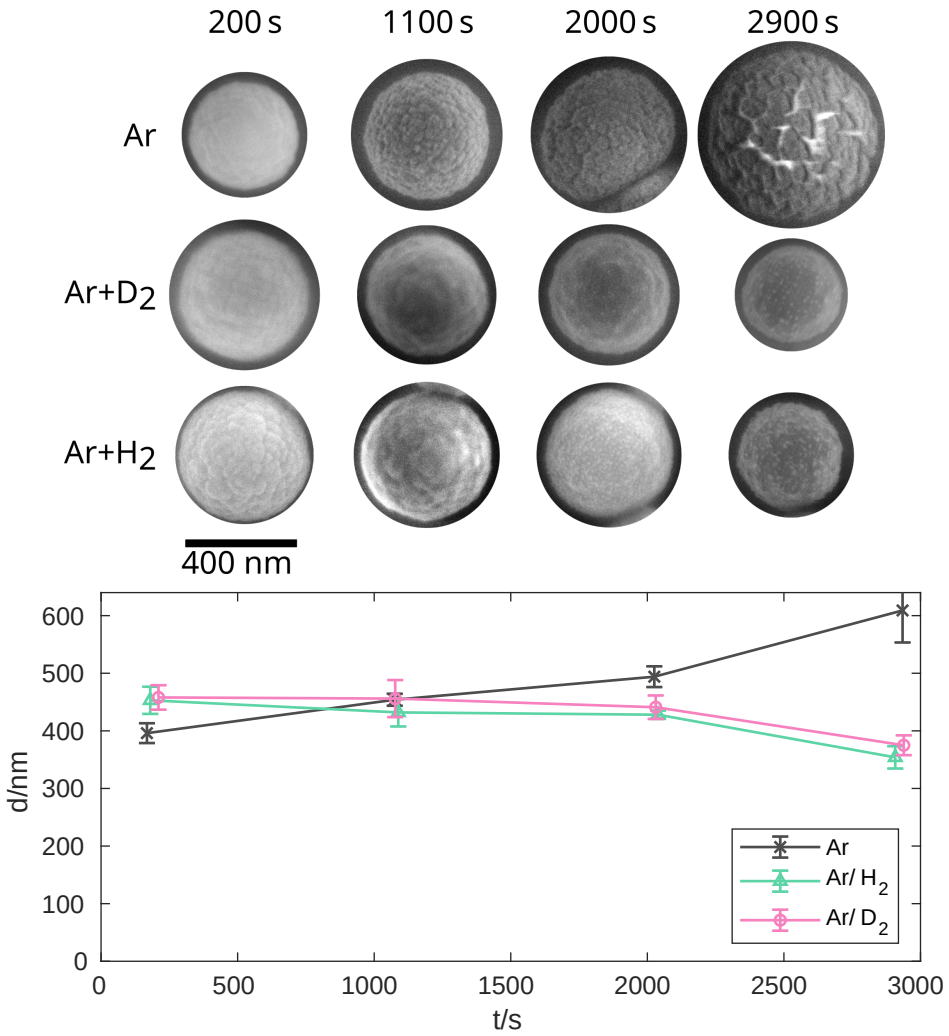

Figure 4.1: SEM images of the extracted particle samples and resulting size evolution for Ar, Ar/H_2, and Ar/D_2 treatments. The treatment was started at $t = 0$ s. Error bars are calculated from measuring particle radii on overview SEM images of 20–80 particles. Published in [17].

section 3.3 and follow procedures described by Tadsen et al. [16].

The long-term effects of different particle treatments are investigated by creating and trapping amorphous hydrogenated carbon (a-C:H) nanoparticles in the chamber and then comparing the effects of pure argon treatment to treatments with admixtures of hydrogen, deuterium, and oxygen. Particles are generated by injecting 8 sccm of a mixture of 20 % acetylene (C_2H_2) diluted in argon into the chamber for 90 s, resulting in a gas pressure of 22 Pa during particle synthesis. After injection, the system rests for 2 min to let any remaining precursors fully react, leading to a final pressure of 18 Pa before the start of the treatment. Samples are extracted every 15 min using the electrostatic particle extractor (EPEX) (see section 3.2) for ex situ scanning electron microscopy (SEM) imaging (see fig. 4.1). Fourier-transform infrared spectroscopy (FTIR) spectra are taken for continuous monitoring averaging over 64 scans at a resolution of 2 cm^{-1} every 6 s during particle growth and over 512 scans every 50 s during the subsequent confinement

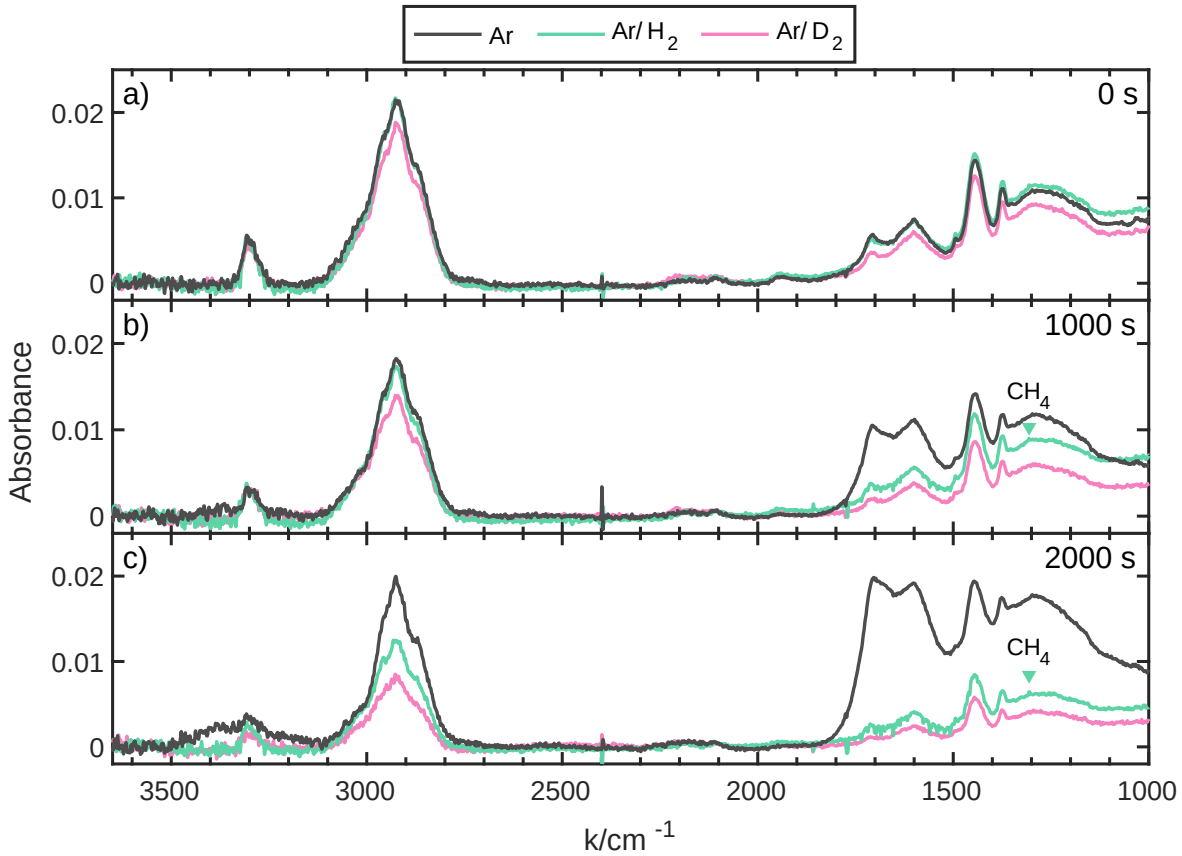

Figure 4.2: Infrared absorption spectra adjusted for background absorption from Rayleigh-Mie scattering. Spectra shown after 0, 1000, and 2000 s of treatment for Ar, Ar/H_2, and Ar/D_2 treatment. The position of the CH_4 fundamental bending mode was marked. Published in [17].

and treatment (see fig. 4.2).

4.1.1 Argon treatment

Whereas previous publications reported a decrease in particle mass due to argon plasma exposure for both microparticles [12] and nanoparticles [14], here, an increase in particle diameter is observed instead, indicating a corresponding increase in particle mass. SEM images in fig. 4.1 show an increase in diameter from about 400 nm to 600 nm over 45 min together with larger scale surface features appearing compared to the typical cauliflower-like structure of untreated particles.

Differentiating between sp^2 and sp^3-hybridised CH bonds in the infrared spectra provides further insight into the processes at work. As explained in greater detail in section 3.1.2.1, no statements can be made about the overall hybridisation state of carbon atoms, but rather only for the portion of hydrogenated CH sites. In fig. 4.3a, in the initial 500 s of treatment, all signals show a decrease likely due to reorganisation of the particle cloud after the initial particle formation. Afterwards, the sp^3 CH_x bonds generally stay constant with only sp^3 CH_3

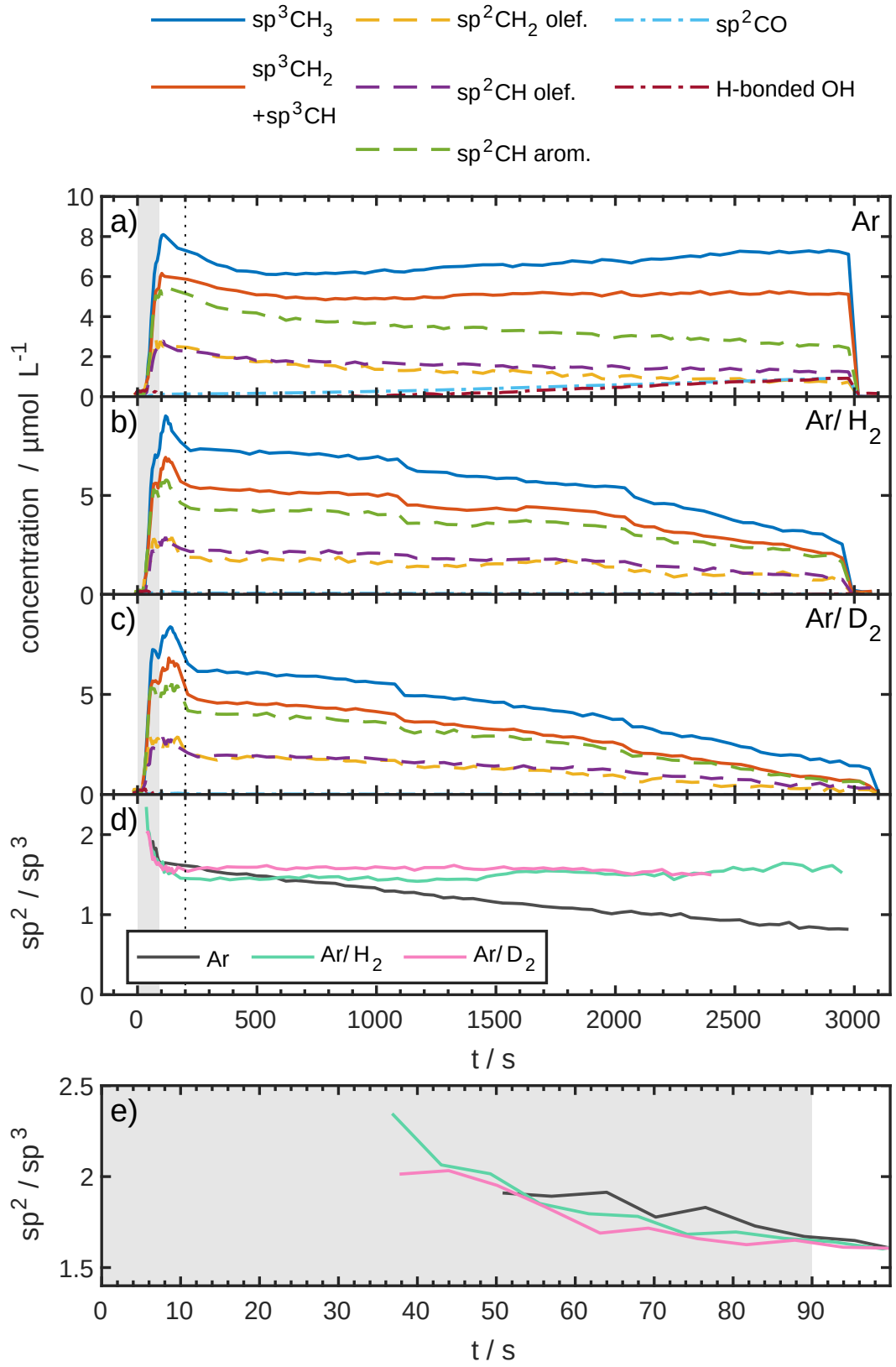

Figure 4.3: a,b,c) Time evolution of CH bond concentrations determined by decomposition of the stretching vibrations in infrared spectra for Ar, Ar/H_2, and Ar/D_2 treatments shown in fig. 4.2. Absorption line intensities were converted using calibration factors described by Ristein et al. [18]. The particle growth period is marked in grey and the start of treatment is marked with a dotted line. d,e) The ratio of sp^2 to sp^3 CH groups for different treatments with an enlarged version of the first 100 s. Published in [17].

bonds showing a slight increase over time. However, sp^2-hybridised bonds show a decrease over the treatment duration together with a comparable increase in sp^2 CO and OH bonds.

This suggests that oxygen is incorporated into the particle material rather than etching and removing material from the particle. Furthermore, the decrease in sp^2 bonds indicates that oxygen attachment primarily happens at sp^2-hybridised CH bonds, where the C=O and C−OH groups are then formed. The formation of C=O leads to the detachment of hydrogen, which itself can also attach at sp^2 C sites, leading to the observed increase in sp^3 CH_x bonds, or stay trapped in unbound forms that cannot be measured via infrared spectroscopy.

During the particle generation process, the sp^2 to sp^3 ratio provides further insight into the properties of the particles. Around 40 s after the start of acetylene injection, CH_x stretching vibrations start to become measurable (see fig. 4.3e). Here, the sp^2 to sp^3 ratio starts at around 2 to 2.3 before dropping to about 1.7 towards the end of the particle synthesis. Kovačević et al. [19] describe sp^2-poor material being formed during the surface growth phase around an sp^2-rich core. As described in section 2.4.2 the transition to surface growth happens at a particle size of about 10 nm. From previous measurements performed by Groth et al. [14] under experimental conditions similar to ours, at 40 s a particle diameter of around 200 nm would be expected, significantly larger than this transition point described by Kovačević et al. [19].

One possible explanation for the initially high sp^2 content measured in our experiments could be annealing processes through surface heating of nanoparticles, which are more efficient at smaller particle sizes (see section 2.3.3). Over the duration of particle growth, this would lead to a decreasing sp^2 content as the particle size becomes larger and selective heating does not reach the annealing temperature any more, leading to a decrease in the measured volume-averaged sp^2 to sp^3 ratio.

A rough estimation for the involved oxygen flux can be obtained by looking at the increase of particle volume. Assuming a constant material density for both unoxidised and oxidised a-C:H material of $1\,\mathrm{g\,cm^{-3}}$, which is a typical value for polymer-like a-C:H films [20], the volume change of the particle can be converted into a mass change. Further assuming that this mass increase exclusively comes from oxygen atoms incorporated into the particle material and a particle number density of $5 \cdot 10^{13}\,\mathrm{m^{-3}}$ measured by Tadsen et al. [21], the flux of oxygen atoms can be estimated to be $1 \cdot 10^6$ O atoms/particle/s. This is in good agreement with the measured concentrations of sp^2 CO and H-bonded O−H groups, which gives a flux of $1.3 \cdot 10^5$ O atoms/particle/s.

If this flux was entirely realised as collisions of neutral gas impurities with the particles, the necessary partial pressure of impurities would be at a level of approximately $4 \cdot 10^{-4}$ Pa at room temperature, which is far below the base pressure of the reactor of around 10^{-2} Pa. This difference can be partially explained as the impurities likely stem from ambient air, which only consists to about a fifth

of oxygen and additionally the reaction probability of each collision is lower than 100 %.

Another source of oxygen are impurities that are ionised by the plasma, such as O_2^+, O^+, H_2O^+ and others. As the particle charge is limited by strong electron depletion due to the Havnes effect, the particles obtain about 20 elementary charges instead of the 1600 according to the orbital motion limited (OML) model (see section 2.2.1). Based on their Coulomb interaction, the collision rate of particles with a diameter of 500 nm with ionised plasma impurities leads to an estimation of the particle number density of $6 \cdot 10^{12}\,\mathrm{m}^{-3}$ (compared to the plasma density in the order of $10^{15}\,\mathrm{m}^{-3}$). It would therefore necessitate that both neutral and ionised impurities contribute to the particle oxidation to explain the measured oxidation rates.

4.1.2 Oxygen treatment

Infrared spectroscopy cannot distinguish between carbon bonded at the surface versus in the bulk of the particle. The observed effects in the previous section could both be explained by the growth of an oxide layer on the particle surface or the diffusion of oxygen into the particle bulk. To differentiate between the two effects, an oxygen etching treatment will be performed analysing the composition of the particle in different depths.

The argon treatment experiment was repeated with an oxygen treatment after 10 min of confinement in an Ar plasma. The oxygen flow was set to 0.8 sccm resulting in a partial pressure of about 2.1 Pa of oxygen. At these admixtures significantly higher than the impurity level, oxygen does show a strong etching effect. Immediately, absorption bands from CO_2 and CO in the gas phase appear together with a strong decrease of CH_x absorption (see fig. 4.4). The particles disappear completely after only 10 min of treatment, whereas CO_2 absorption continues afterwards. This is likely due to the oxygen plasma reacting with carbon material on the chamber walls to continue forming CO_2.

Furthermore, taking a closer look at the evolution of C=O bonds reveals a very quick drop in concentration compared to CH_x bonds in the initial 20 s. Afterwards, the concentration decreases at a slower rate than the CH_x curve. This indicates that the incorporated oxygen is located primarily on the particle's surface and is removed quickly during oxygen treatment. Once that oxide layer is removed, the remaining C=O bond signal likely stems from an intermediate product being formed on the surface during the etching process. For a quantitative analysis, a closer investigation of the competing processes $C + O \longrightarrow C{=}O$ and subsequently $C{=}O + O \longrightarrow CO_2$ would be necessary, combining the FTIR findings with a chemical reaction model.

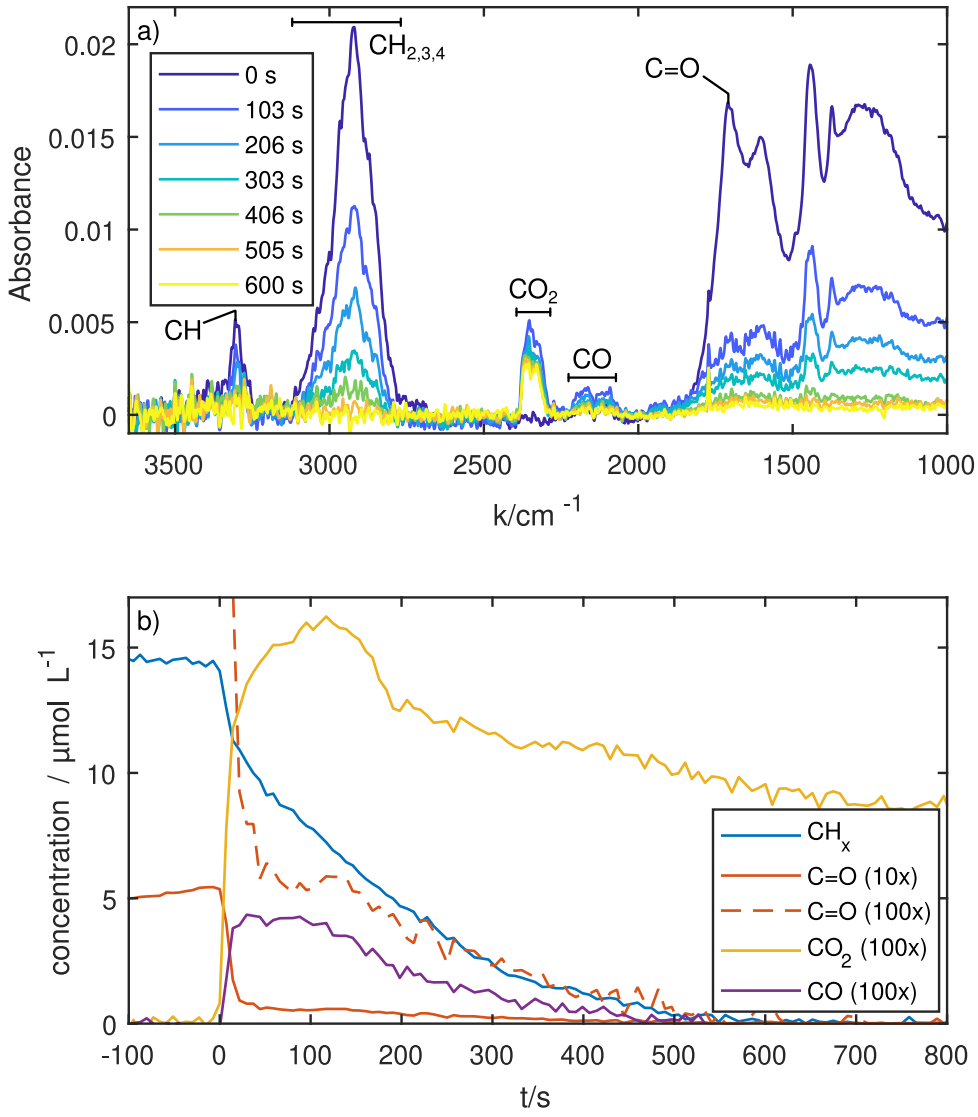

Figure 4.4: a) Infrared absorption spectra during the oxygen treatment of a-C:H particles. Treatment starts at $t = 0\,\mathrm{s}$. Regions of the stretching vibrations of different bonds and compounds are labelled. b) Concentrations of CH_x and C=O bonds determined by decomposition of stretching vibrations in the absorbance spectrum and gaseous CO_2 and CO determined by integration over the entire vibration bands. The concentration of C=O is shown twice, once scaled by a factor of 10 and once by a factor of 100. Concentrations of CO_2 and CO are scaled by a factor of 100.

4.1.3 Hydrogen and deuterium treatment

Treating the particles with hydrogen shows two separate effects. Firstly, the oxidation of the particles as described above for the argon treatment with an increase of sp^2 CO and C−OH groups is not observed any more. Instead, absorption from water increases over the course of the treatment (see figs. 4.2b and 4.2c), indicating that the oxygen impurities which were previously incorporated in the particle now react with the hydrogen gas inside the plasma instead.

Secondly, absorption from CH_x groups decreases significantly over the treatment duration. A useful measure for the particle composition is the ratio of sp^2- versus sp^3-hybridised CH_x groups. While one needs to be careful with this analysis, as infrared spectroscopy cannot detect unhydrogenated carbon atoms in either hybridisation state (see section 3.1.2.1), this ratio still provides a useful tool to observe the effects of hydrogen treatment. Insertion of hydrogen atoms into the structure would generally increase the fraction of sp^3 hybridisation. Contrarily, the measurements in fig. 4.3d show that the ratio of sp^2 to sp^3 CH_x groups stays constant during the hydrogen treatment.

Another possible process would be the abstraction and subsequent reattachment of hydrogen. To be capable of measuring this effect, the treatment is repeated using deuterium as a tracer gas. As the stretching vibration of CD_x bonds shows absorption at a different region around $2100\,cm^{-1}$, the substitution of hydrogen by deuterium would be visible in the infrared spectrum. Yet, no such absorption was visible during the deuterium treatment, suggesting that no deuterium is attached to the particle.

This leads to the conclusion that the primary process during hydrogen treatment is likely the etching of carbon groups from the particle surface by atomic hydrogen and hydrogen ions (H^+, H_2^+, H_3^+). Typical etch products of hydrogen plasma treated a-C:H films would be CH_4 and C_2H_4 molecules [22]. While no C_2H_4 signal was measured, for the hydrogen treatments a very weak peak around $1306\,cm^{-1}$ (see figs. 4.3b and 4.3c) is identified as the ν_4 fundamental bending mode of the CH_4 molecule [23]. As the chamber is continuously pumped during the treatment process, any etching products are likely quickly removed from the observed volume explaining the low signal intensity.

4.2 Silicon nanoparticles

After analysing the in situ synthesis of a-C:H nanoparticles, the focus now shifts towards externally generated particles that are then held and treated in a secondary discharge. By separating particle generation and treatment into two discharges, the conditions for each can be chosen freely and adjusted for the particular application as described in detail in section 3.4.

The goal of these experiments is the confinement and controlled treatment of particles using hydrogen and deuterium as reactive gasses. Selective heating

processes during hydrogen treatment can lead to recrystallisation of particles [24, 25] and serves as a proof of principle experiment for future treatments using a variety of organic and organometallic precursor gasses. Both hydrogen and deuterium show similar behaviour and reaction cross sections, but deuterium exhibits a shift in stretching vibration frequencies of a factor of $1/\sqrt{2}$ due to the 1:2 mass ratio of H_2 and D_2. This makes it a suitable tracer for separating attachment and detachment processes of groups on the particle surface.

As described in section 2.3, hydrogen has multiple pathways of interacting with silicon nanoparticles. In small concentrations, H_2 treatment can lead to abstraction of hydrogen from the amorphous hydrogenated silicon (a-Si:H) surface through various mechanisms [26]. In higher concentrations, sequential insertion of hydrogen into the Si−Si bonds leads to formation of higher silicon hydrides. Once SiH_4 is formed, the connection to the rest of the network is severed and we observe etching.

FTIR spectroscopy is used to monitor the evolution of the SiH and SiD bonds in the various possible hydride and deuteride groups. Calibration factors are necessary to convert these integrated absorption intensities into bond concentrations, as described in section 3.1.2.2. Note that the term concentration can be misleading here, as it is referring to the concentration of bonds in an averaged volume along the line of sight of the infrared beam rather than in the volume of particle material. If the particle number density were to increase due to plasma effects, the measured concentrations would increase as well even if the particle's properties did not change.

The measurements shown in figs. 4.5 to 4.7 were performed using 70 sccm of argon resulting in a pressure of 26 Pa in the holding chamber. The particles are generated using a flow of 90 sccm of Ar/SiH_4(1 %) at a pressure of about 500 Pa at the start of the glass tube and 60 Pa measured in the differential pumping stage. The treatment gasses were pre-mixed using a system described in detail in section 3.4. This setup was reworked between the H_2 and D_2 treatment measurements to provide a more homogeneous mixing. While a mixture of Ar/H_2(1 %) was attempted, the actual concentration is more likely to have been around 10 %. The deuterium measurements performed after the rework have used better-defined mixture of Ar/D_2(10 %). Both treatments used 0.1 sccm of the pre-mixed gas. Typical signal-to-noise ratios $A/\Delta A$ for the absorption spectra were around 10–30 for the various bulk hydride peaks and about 7 for the mainly visible 2-bonded hydride surface peak. For deuterides, the bulk peaks range between $A/\Delta A = 5$–13 and around 6 for the main 2-bonded surface deuteride peak.

Despite the preconditioning procedure for the chamber, the different experiments show small differences before the injection of the treatment gasses. A variation of the silicon hydride concentration in the bulk material of around 20 % can be seen in fig. 4.6a after particle injection. The composition of the particles also differs slightly between experiments, as can be seen in fig. 4.5, where especially SiH and SiH_4 content of the particles differs significantly before the

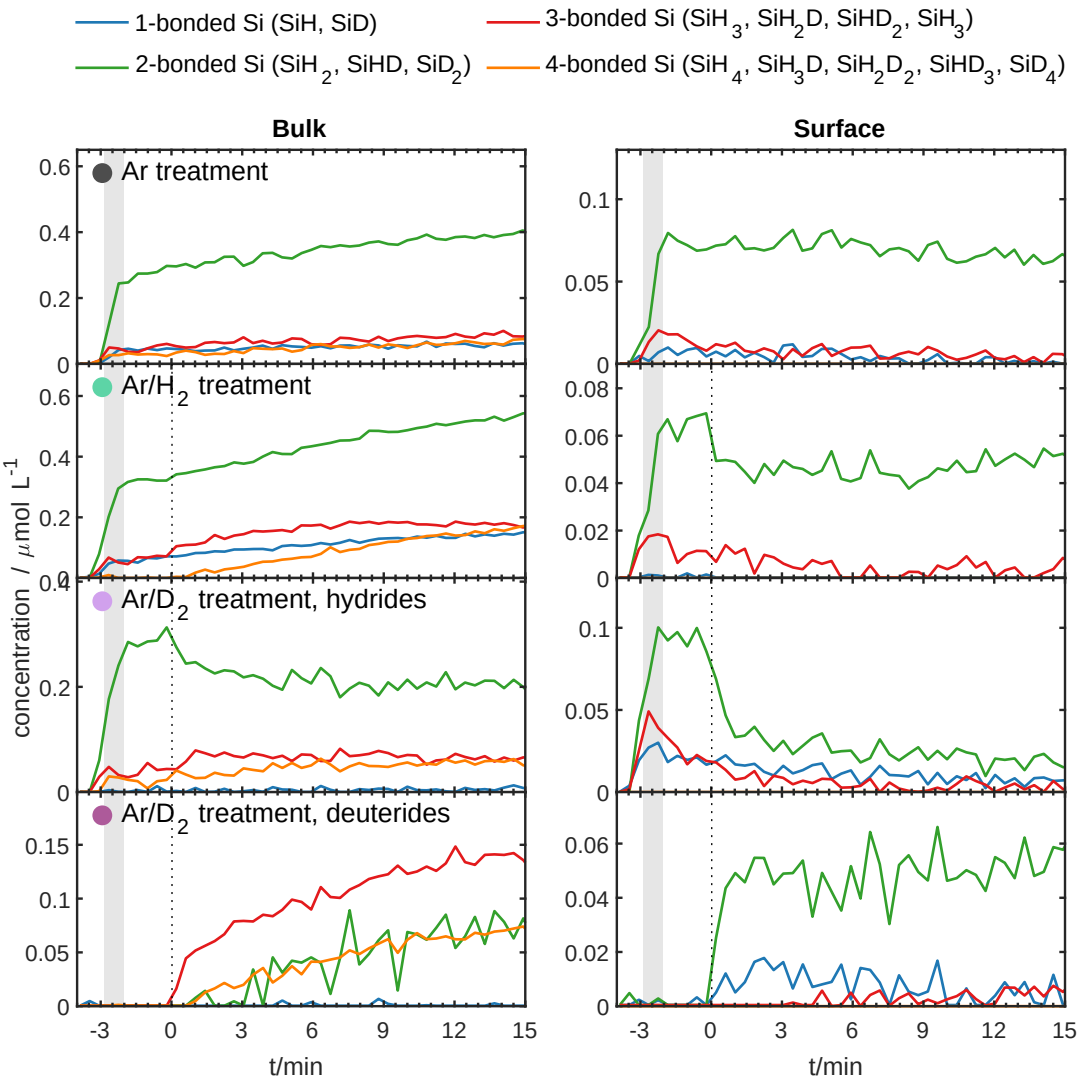

Figure 4.5: Bond concentrations for different hydrides and deuterides treated with pure argon plasma, with Ar/H_2, and with Ar/D_2 (coloured dots in reference to figs. 4.6 and 4.7). For the deuterium treatment, hydrides and deuterides are separated. Particles were injected during the period highlighted in grey. Treatment is started at $t = 0\,\mathrm{s}$ indicated by the dotted vertical line.

start of treatment. Yet, the overall repeatability of the experimental conditions is sufficient to be able to compare the impact of different treatment gasses.

Without additional treatment gas, a slow increase of 40 % in bulk Si sites is seen over 15 min (cf. fig. 4.6a). Surface growth due to precursors created by plasma interactions at the chamber walls could explain this increase in Si sites. Another explanation would be the incorporation of hydrogen into the particle material.

The evolution of surface bonds is helpful to differentiate between these two explanations, as a size increase of the particle through surface growth should result in an increase of its surface area. As any impinging precursors that could facilitate surface growth are likely to contain hydrogen, they would be visible in the infrared spectrum and lead to an increase of surface hydrates in the infrared signal. If the particle was to display growth from a size r_1 to a larger r_2, the

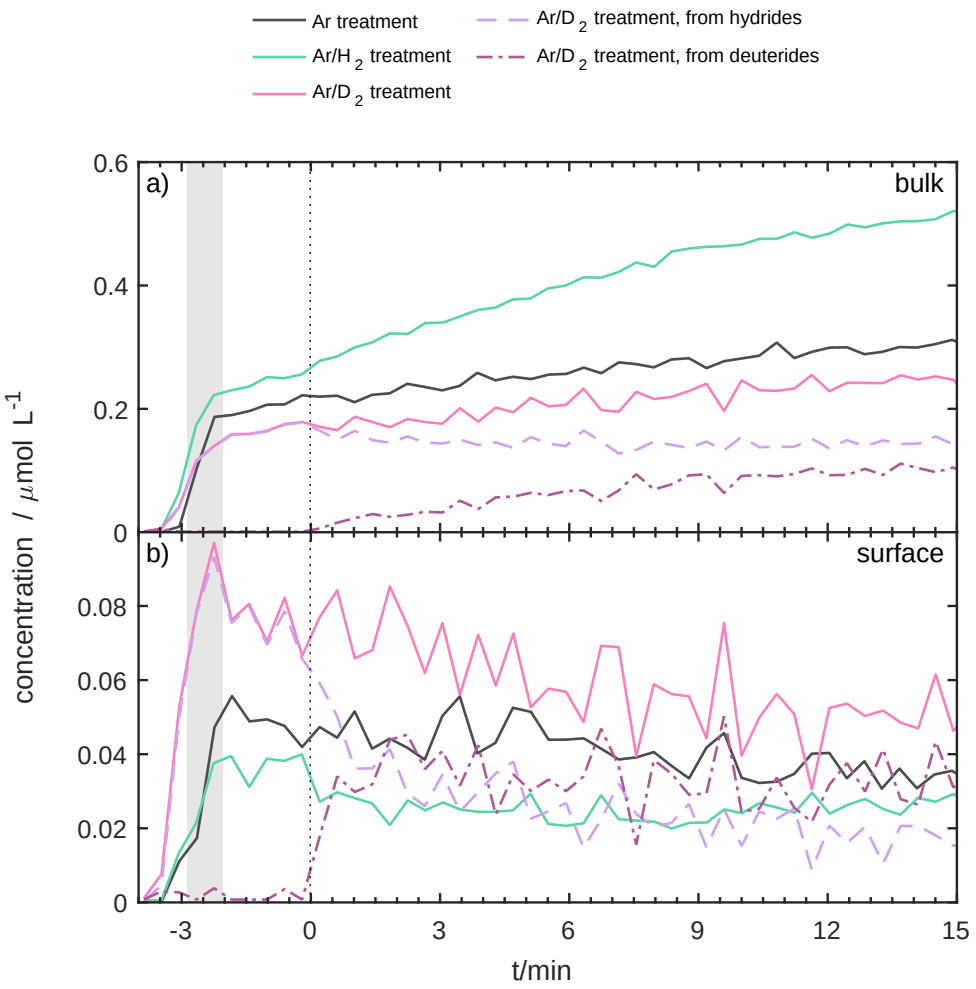

Figure 4.6: Overall concentrations of hydrogenated (or deuterated) silicon sites for particles treated with a pure argon plasma, with Ar/H_2, and with Ar/D_2. Sites are differentiated between a) the particle bulk and b) its surface. For the deuterium treatment, measured concentrations are split into their hydride and deuterate fractions. Particles were injected during the period highlighted in grey. Treatment is started at $t = 0$ s indicated by the dotted vertical line.

change in volume $\Delta V/V$ can be expressed as:

$$\begin{aligned} \Delta V &= \frac{3}{4}\pi\left(r_2^3 - r_1^3\right), \\ \Rightarrow 1 + \frac{\Delta V}{V} &= \frac{r_2^3}{r_1^3}, \\ \Rightarrow \qquad r_2 &= r_1\left(1 + \frac{\Delta V}{V}\right)^{\frac{1}{3}}. \end{aligned} \tag{4.1}$$

Similarly, we can express the change $\Delta A/A$ in surface area in relation to $\Delta V/V$ as:

$$\begin{aligned} \Delta A &= 4\pi\left(r_2^2 - r_1^2\right), \\ \Rightarrow 1 + \frac{\Delta A}{A} &= \frac{r_2^2}{r_1^2}, \\ &= \left(1 + \frac{\Delta V}{V}\right)^{\frac{2}{3}}. \end{aligned} \tag{4.2}$$

If the measured increase in Si sites was fully created by surface growth of new material, we would expect a volume increase of $\Delta V/V = 0.5$, leading to an increase of surface area of $\Delta A/A = 0.31$. This, in turn, should lead to a proportional increase in Si sites on the surface, which we do not observe (cf. fig. 4.6b).

For H_2 treatment, an even larger increase of 100 % in bulk Si sites is seen over 15 min, while the surface concentration even drops by almost 25 % in the first 2 min to then remain mainly constant. Therefore, surface growth can be ruled out and incorporation of hydrogen into the particle is the likely explanation. This can be seen especially in the comparison between argon and hydrogen treatments. In the argon case, all hydrides increase in conjunction, whereas for hydrogen treatment, 3- and 4-bonded silicon increases strongly after the start of the treatment. This indicates that hydrogen is incorporated into existing bonds as well as creating further SiH bonds from previously unhydrogenated silicon. It is unclear, why only 2- to 4-bonded sites are showing a sudden jump when treatment starts while SiH rises continuously.

4.2.1 Differentiation into n-bonded hydrides and deuterides

The decomposition into the different hydrides and deuterides can be used to determine the average number of hydrogen (and/or deuterium) atoms per hydrogenated (or deuterated) silicon atom. Note that silicon that is exclusively bonded to other silicon atoms does not absorb in the infrared and cannot be measured in this analysis. Therefore, fig. 4.7 only averages over at least 1-bonded silicon sites and does not take into account the unknown concentration of 0-bonded sites. Using

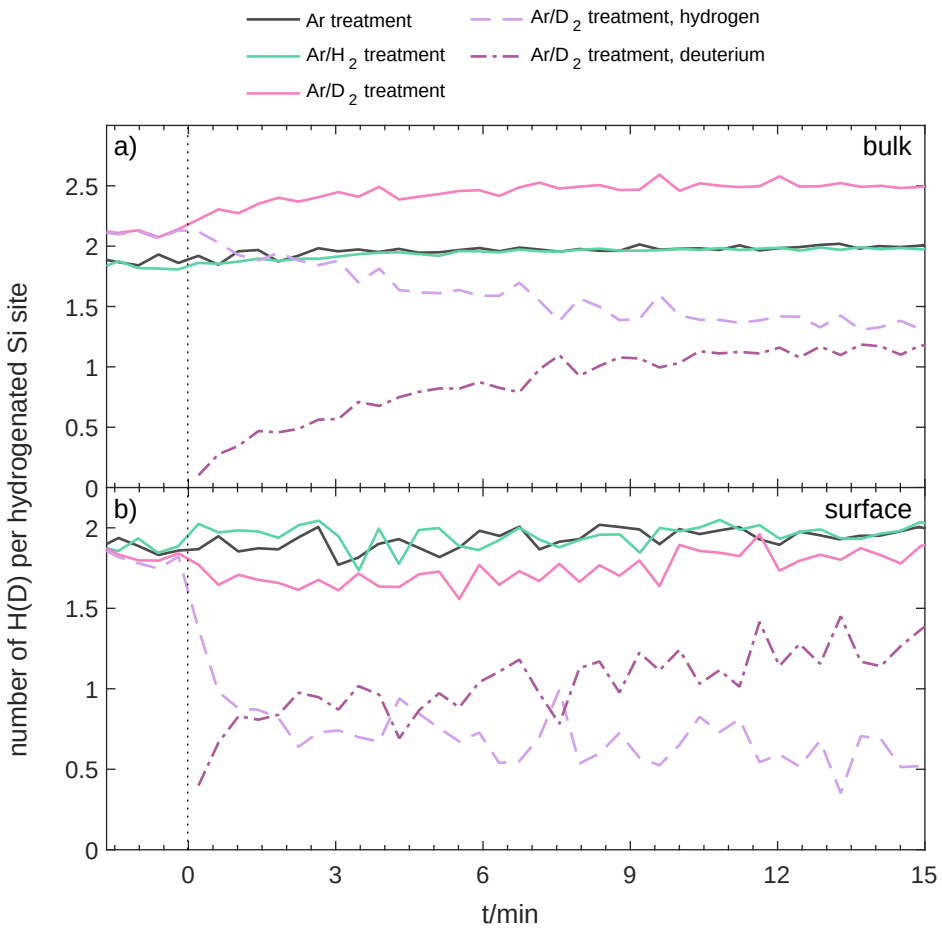

Figure 4.7: Average number of H(or D) atoms per hydrogenated (or deuterated) silicon site shown over the duration of the treatment for a) bulk and b) surface sites. Note that unhydrogenated sites cannot be measured in infrared spectroscopy. This is therefore not a measurement of the absolute hydrogen content of the a-Si:H material.

this measure, there is no significant change over the duration of the hydrogen treatment. The average number x of hydrogen (and/or deuterium) atoms per hydrogenated (or deuterated) silicon site is almost constant starting at $x = 1.8$ and ending at $x = 2.0$. Newly created 3- and 4-bonded silicon sites are counterbalanced by the generation of 1- and 2-bonded sites.

Finally, looking at the deuterium treatment results provides further insights into the treatment process. First note that the measurement of Si sites shown in fig. 4.6 can be misleading for partial deuteration. For example for a SiH_3 group, the measured SiH bond concentration is divided by 3 to result in the Si site concentration. If that group gets partially deuterated into a SiH_2D group, the division by 3 will result in a seemingly lower Si site concentration, as one-thirds of that concentration are now attributed to deuterides instead. Only the sum of concentrations from hydrogenated and deuterated sites will give the true 3-bonded Si site concentration.

The concentrations in fig. 4.6 show a strong initial decrease by 30 nmol L^{-1} in hydride concentration in the first 90 s coinciding with an increase by the same amount in deuterides. In the remaining treatment period, the hydride concentration stays constant while the deuteride concentration increases further, leading to the overall silicon concentration resembling the curve of pure argon treatment. The average number of hydrogen (and/or deuterium) atoms per hydrogenated (or deuterated) Si site in the particle bulk increases by 0.4 compared to 0.2 in the case of pure argon and Ar/H_2 treatment. The deuterium treatment mainly creates new 3- and 4-bonded deuterides in the particle bulk. Given that before the treatment, SiH_2 was the dominant species in the bulk material, it seems likely that deuterium is preferentially inserted at these sites to create SiH_2D. After about 1 min, 4-bonded silicon species concentrations (likely SiH_2D_2 and SiH_3D) appear, similar to the case of hydrogen treatment. These are likely to be interstitially trapped molecules inside the bulk material.

On the particle surface, different interactions are seen. Here, the average number x stays constant at around $x \approx 1.8$. The dominant surface deuteride is 2-bonded silicon, i.e. SiHD or SiD_2, followed by SiD. This indicates that on the surface, hydrogen preferably is substituted for deuterium, whereas it preferably is inserted in the bulk material instead.

4.2.2 Estimation of total silicon site concentration

While pure Si−Si_4 sites cannot be measured in the infrared, the expected initial hydride concentration can be used to estimate an initial pure silicon site concentration. The atomic concentration of hydrogen can be calculated from the individual SiH_k signals measured with infrared spectroscopy, as each Si−H bond absorbs separately:

$$c_\mathrm{H} = \sum_{k=1}^{4} c_{\mathrm{SiH_k}} \,. \tag{4.3}$$

A similar calculation can be performed for the atomic concentration of silicon, taking into account the number of hydrogen present at each n-bonded hydride:

$$c_\mathrm{Si} = c_{\mathrm{Si},0} + \sum_{k=1}^{4} \frac{c_{\mathrm{SiH_k}}}{k} \,, \tag{4.4}$$

where $c_{\mathrm{Si},0}$ is the initial unhydrogenated silicon concentration. This concentration can be calculated by assuming an initial hydrogen fraction f of the particle:

$$\begin{aligned} f &= \frac{c_\mathrm{H}}{c_\mathrm{H} + c_\mathrm{Si}} = \frac{\sum_{k=1}^{4} c_{\mathrm{SiH_k}}}{\sum_{k=1}^{4} \left(1 + \frac{1}{k}\right) c_{\mathrm{SiH_k}} + c_{\mathrm{Si},0}} \,, \\ \Rightarrow c_{\mathrm{Si},0} &= \sum_{k=1}^{4} c_{\mathrm{SiH_k}} \left(\frac{1}{f} - 1 - \frac{1}{k}\right) \,. \end{aligned} \tag{4.5}$$

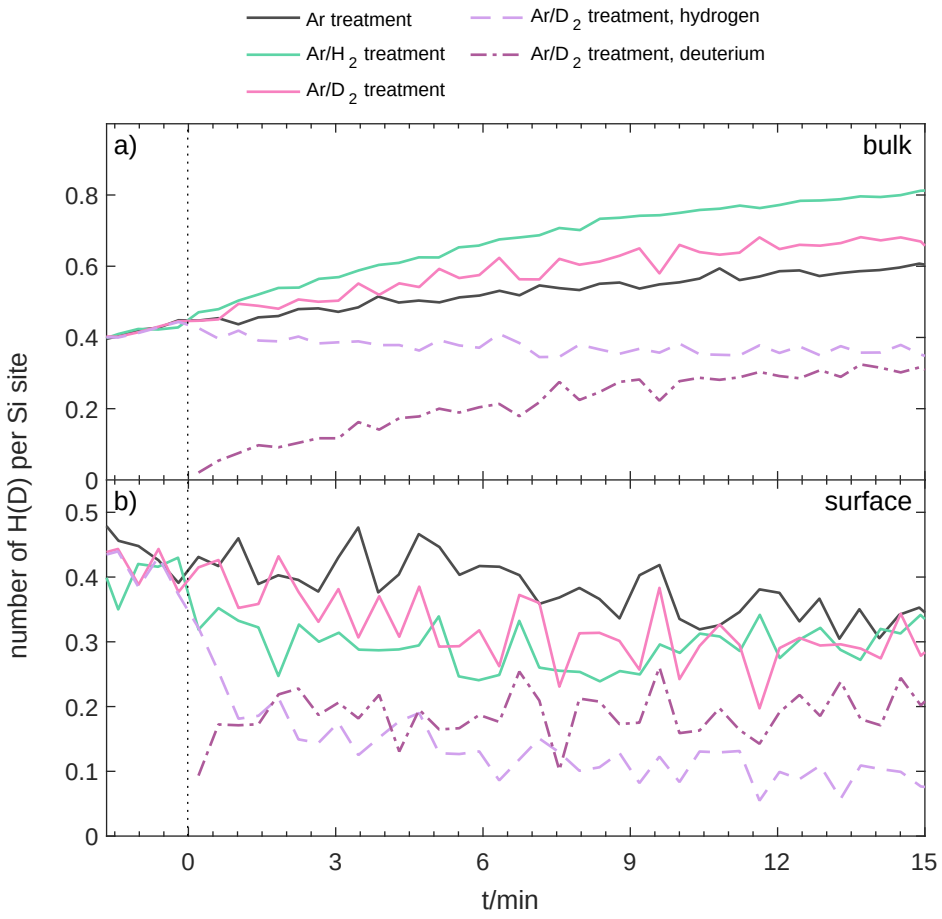

Figure 4.8: Average number of H(D) atoms per silicon site shown over the duration of the treatment for a) bulk and b) surface species. Unhydrogenated sites were estimated with an initial hydrogen fraction of $f = 30\,\%$ at $t = -45\,\mathrm{s}$.

As we have ruled out particle growth during the treatment period, any newly appearing SiH must come from hydrogenation of previously pure $\mathrm{Si{-}Si_4}$ sites. Therefore, we can – as a first approximation – assume the concentration of silicon atoms to decrease through generation of new SiH bonds, i.e. $c_{\mathrm{Si}} = c_{\mathrm{Si},0} - (c_{\mathrm{SiH}} - c_{\mathrm{SiH},0})$, where $c_{\mathrm{SiH},0}$ is the initial SiH concentration. This ignores any hydrogenation (or deuteration) of already present SiH bonds and therefore overestimates the silicon concentration.

Using this correction and assuming an initial hydrogen fraction of 30 % at $t = -45\,\mathrm{s}$, we obtain fig. 4.8. While the argon and $\mathrm{Ar/H_2}$ treatments seemingly resulted in the same curves in fig. 4.7, applying the correction there is a clear separation between them. The argon treatment still shows an increase in average bulk hydrogen atoms per silicon atom, but both $\mathrm{Ar/H_2}$ and $\mathrm{Ar/D_2}$ treatments lead to a significantly steeper increase.

4.3 Silver-silica core-shell nanoparticles

The central piece of the project is a collaboration with the Chair for Multicomponent Materials of Prof. Faupel at the Faculty of Engineering. The goal is to combine their knowledge about gas aggregation source (GAS) for the generation of noble metal – in particular silver – nanoparticles and their measurement using localised surface plasmon resonance (LSPR) with our expertise in the treatment of particles and monitoring using infrared spectroscopy to create core-shell Ag@SiO_2 nanoparticles in a precisely controlled process. The collaboration has yielded a very promising first step towards self-organised three-dimensional networks of isolated silver nanoparticles which have highly relevant applications for neuromorphic computing [27–31].

Networks of silver particles in an insulating matrix can show memristive behaviour, as a network at the percolating threshold form enough bridging connection to lead to a drastic increase in conductivity [31]. The core-shell nanoparticles created in this work present the opportunity to include the insulating matrix directly with the nanoparticles themselves and allow for significantly higher particle densities as well as highly three-dimensional network structures. The silica shells isolate the particles to create a non-conductive network at first. By applying a voltage, the network can display memristive behaviour as the mobile silver atoms form reversible filaments in the network structure.

This section presents the results achieved with a setup combining the SFB chamber as a treatment plasma with the external generation of Ag nanoparticles in the GAS as described in section 3.5. First, the long-term confinement of Ag nanoparticles is demonstrated using LSPR. Then, in situ coating is performed to create Ag@SiO_2 core-shell nanoparticles monitored using both LSPR and infrared spectroscopy. The findings are confirmed using ex situ transmission electron microscopy (TEM) and energy-dispersive X-ray spectroscopy (EDX) analysis. Finally, the possibility of multi-step nanofabrication of tailored nanoparticles is demonstrated with an etching experiment using a hydrogen plasma.

4.3.1 Long-term confinement

Analysing the LSPR response provides insight into the changes especially on the particle surface, where it is particularly sensitive to changes in dielectric properties of the material surrounding the plasmonically active core. Figure 4.9 shows the results for long-term confinement of pure silver nanoparticles in an argon plasma. The particles exhibit an initial redshift of the main resonance peak of about 9 nm in the first 10 min, staying constant afterwards for the remaining treatment duration. A redshift can be caused by an increase in size of the particles or a change of their surrounding dielectric. As there are no sources of silver in the holding plasma, a size increase of the cores would come from agglomeration. Particles in the holding plasma are charged by the plasma environment and

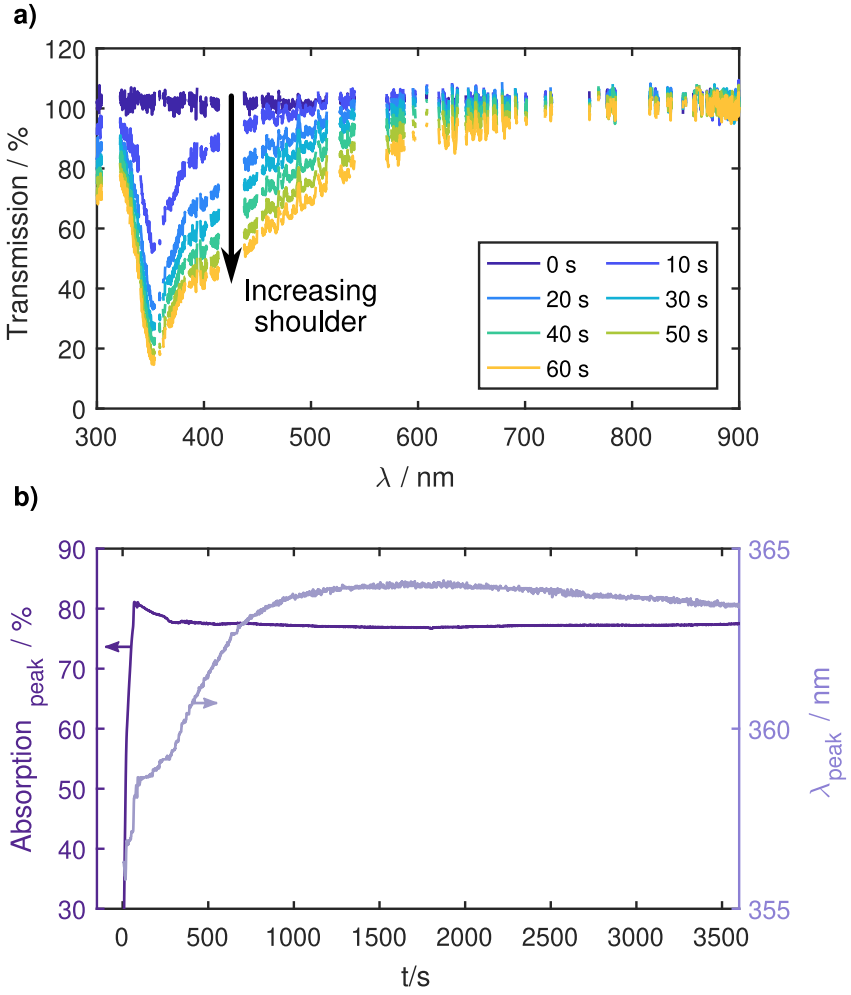

Figure 4.9: LSPR measurements of silver nanoparticles injected at $t = 0$ s for 60 s followed by 1 h of confinement in a pure argon plasma at 11 Pa and 100 W CCP power. a) In situ ultraviolet-visible (UV-Vis) absorption spectra for 7 different times during the particle injection. Plasma emission lines are removed from the spectra. b) Result of the analysis of absorption spectra during the entire experiment duration. The left axis shows the absolute height of the main absorption peak, while the right axis shows its position. Published in [32].

repulse each other, making agglomeration less likely. Further investigation of the possibility of agglomeration will be presented in section 4.3.3 with results from TEM imaging.

It is more likely that trace amounts of oxygen in the treatment plasma lead to oxidation of the particle surface, creating a new surrounding dielectric with a permittivity $\epsilon_r > 1$ inducing a redshift and a slight size reduction of the plasmonically active cores, which would generally result in a blueshift. Yet, for particles smaller than 20 nm, the plasmonic resonance frequency does only depend very weakly on particle size [33].

The maximum absorption intensity of the main peak increases significantly to 80 % of the total incident light during the injection period, indicating a very high particle density in the holding plasma compared to previously performed in-flight

measurements at the GAS by Drewes et al. [34]. It is followed by a small decrease of about 5 % in the first 4 min staying constant afterwards for the remaining treatment duration. This indicates a very good confinement of the particles in the holding plasma with no significant losses over the 1 h confinement period.

Finally, the shape of the absorption peak shown in fig. 4.9a exhibits a shoulder towards higher wavelengths. It becomes more pronounced with longer injection time and likely stems from an increase of plasmonic coupling between particles. Assuming an average particle size of 20 nm and the resulting LSPR cross section for silver particles [33] of $\sigma_{\mathrm{LSPR}} = 2 \cdot 10^3\,\mathrm{nm}^2$, the UV-Vis absorption strength can be used to estimate the particle number density to be $n_\mathrm{d} \approx 10^{15}\,\mathrm{m}^{-3}$. This value is in the same order of magnitude as the typical plasma densities in the used laboratory plasmas, indicating that we are in a regime of strong electron depletion. As described in section 2.2.1, particles are not charging up to their theoretical capacitive limit determined by OML theory, but can only achieve a few elementary charges that are subject to stochastic fluctuations. This means that while the average inter-particle spacing at those particle densities according to the Wigner-Seitz radius $r_\mathrm{WS} = (n_\mathrm{d} \cdot 4\pi/3)^{-1/3}$ is about 10 µm, the weak repulsive forces lead to a much wider spacing distribution, where particles could come close enough for plasmonic coupling to occur. The following experiments were performed at a reduced injection time of 10 s aiming for lower particle densities and largely avoiding plasmonic coupling.

4.3.2 In situ coating and diagnostics

One goal of this joint project with the Faculty of Engineering was to create core-shell nanoparticles for memristive applications. Ag@SiO_2 particles were chosen as a prime candidate for a proof of concept that could later be expanded upon. The process uses the holding plasma to coat the silver particles by injecting silane. This is done in a very low concentration of 20 sccm of Ar/SiH_4(0.01 %) to not induce independent silicon particle growth, but rather have surface growth of a silicon layer on top of the silver particles. Given the leaks present in the system mainly through the rudimentary load lock system, oxygen is available in large enough quantities to create a SiO_2 coating.

Figures 4.10a and 4.10b show the results of such a coating treatment. Four experiments were performed with treatment durations of 1, 3, 5, and 10 min aiming to control the coating thickness. The main LSPR peak shows an overall increase in absorption intensity from 35 % to 52 % as well as a redshift from 355 nm to 385 nm over 10 min. Both of these effects are in good agreement with literature [35–37].

The time evolution of the main LSPR peak position shows a very reproducible behaviour, where each experiment lies on the same curve, only differentiated by the end of treatment duration after which the peak position stays constant. The resonance exhibits a strong redshift in comparison to the untreated case, which is

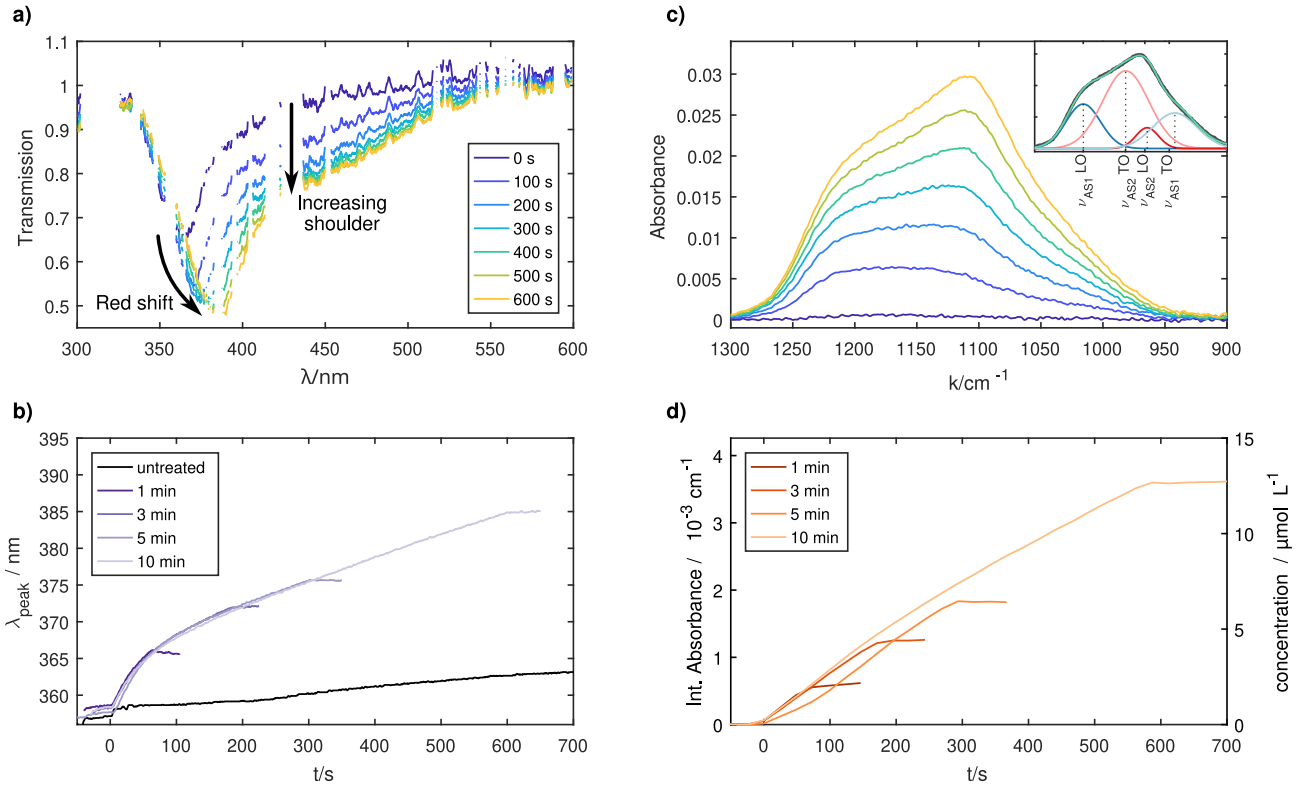

Figure 4.10: Results of coating treatment with silane starting at $t = 0$ s. a) UV-Vis absorption spectra over 10 min of coating. Plasma emission lines were removed. b) Time evolution of the LSPR peak position for four different treatment durations. c) FTIR absorption spectra over 10 min of coating. Inset shows the decomposition into the four constituting Si−O−Si asymmetric stretching modes and their sum of fits. d) Time evolution of the integrated absorption intensity on the left axis, and the resulting Si−O−Si concentration in the plasma volume on the right axis. Published in [32].

in agreement with the growth of a dielectric coating on the particle surface. The redshift is stronger in the beginning of the treatment as the LSPR is especially sensitive to changes on the surface of the plasmonically active core. Since the local electromagnetic field only extends a limited distance from the silver core to the surrounding coating, the dependence of the redshift on the coating thickness is non-linear and further modelling work would be necessary to describe this effect in more detail.

Over the treatment duration, a shoulder appears again as a result of plasmonic coupling as described in the previous section. One explanation could be that the addition of silane as an electronegative gas lowers the free electron density in the dusty plasma even further [38]. This would lead to a further decrease in average particle charge and allow for more coupling to occur.

Infrared spectroscopy provides further insight into the mechanics of the surface growth (see figs. 4.10c and 4.10d). Using the total integrated absorption intensity of the Si−O−Si asymmetric stretching vibration in the region between 950–1300 cm^{-1}, the concentration of Si−O−Si bonds can be determined [39, 40].

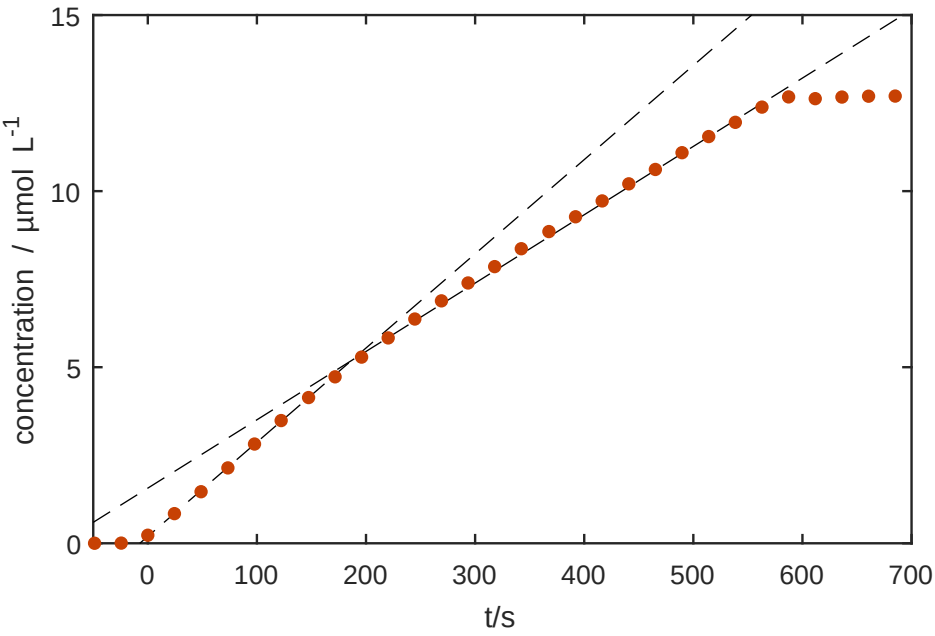

Figure 4.11: Total concentration of Si−O−Si bonds in the plasma volume determined through the decomposition of infrared spectra. Two separate linear functions were fitted to the data between 0–150 s and the remainder of the treatment duration, giving growth rates of 0.23 and 0.17 µmol L^{-1} s^{-1}. Published in [32].

The reproducibility of results is similarly good as in the experiments using UV-Vis spectroscopy. Only the first performed experiment with a coating duration of 5 min shows a delayed onset of coating. This is likely due to the chamber being cleaned using an Ar/O_2 plasma prior to the first experiments, leaving the walls of the chamber conditioned differently than in the following coatings (see preconditioning of the chamber described in section 3.4).

While the curves of Si−O−Si concentration look linear at first glance, a closer look at the results from the 10 min coating treatment shown in fig. 4.11 reveals two growth rates. In the initial 150 s, a rate of 0.23 µmol L^{-1} s^{-1} is measured, followed by a slightly slower phase with a rate of 0.17 µmol L^{-1} s^{-1} for the remainder of the coating process. This is an indication of inhomogeneous growth that will also be seen in TEM images in the next section.

Finally, the long-term effects of plasma exposure on coated particles are investigated by applying 90 s of coating, followed by an hour of argon plasma exposure at 100 W (see fig. 4.12). After coating, the Si−O−Si concentration slowly increases in the first 500 s of treatment, indicating some further growth likely due to residual precursors being used up. Afterwards, the concentration remains constant for the remainder of the hour-long treatment. Ex situ TEM images described in the next section confirm that no changes to the coating can be seen (see fig. 4.15).

4.3.3 Ex situ analysis

Particles from the coating experiments were analysed using transmission electron microscopy (TEM) and energy-dispersive X-ray spectroscopy (EDX) on samples

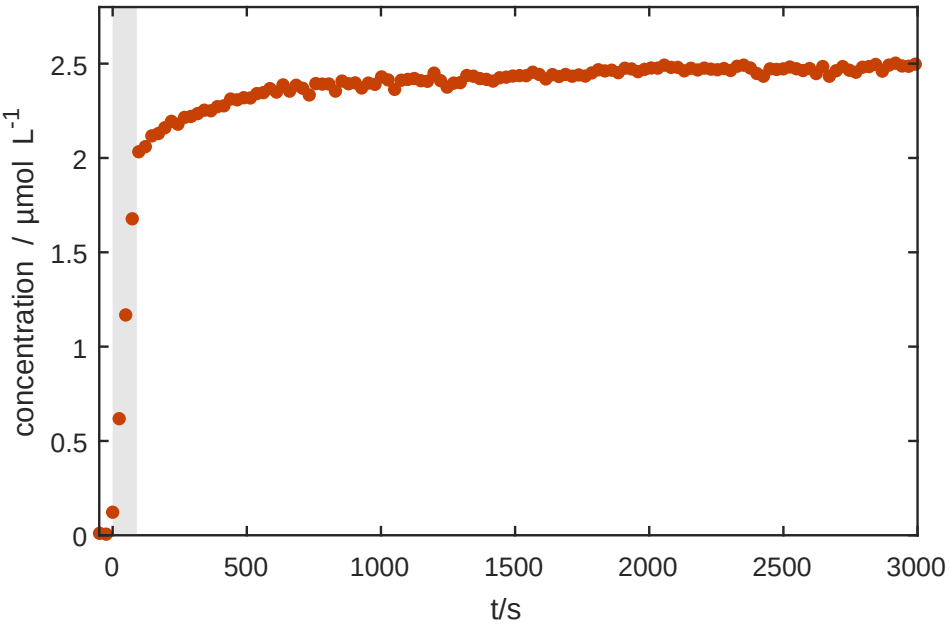

Figure 4.12: Total concentration of Si−O−Si bonds in the plasma volume during long-term argon treatment of SiO_2-coated silver particles. The particles were generated in the GAS and then coated using silane in the first 90 s marked in grey. Published in [32].

extracted using the electrostatic extractor described in section 3.2 with the aim to provide a ground truth for the results from in situ analysis. Figures 4.13a to 4.13d show TEM micrographs of the extracted samples for different coating durations. Coatings up to 5 min do not appear to be homogeneous, but rather display island growth with single segregated regions of SiO_2 on the particle surface. At 1 min, many particles are uncoated with the rest displaying islands of coating. The samples at 3 and 5 min show some particles with complete coatings mixed with others with inhomogeneous patches of coating. After 10 min, all particles are homogeneously coated with a coating thickness of around 6 nm. This growth behaviour is shown schematically in figs. 4.13e to 4.13h.

These observations support the findings from infrared spectroscopy, where the initial 150 s display a higher growth rate than the remainder of the treatment duration. It is likely that the mechanisms of initial island growth differ from surface growth later and the change in growth rate indicates the closure of the previously inhomogeneous coating. There are several possible explanations for the initial inhomogeneity. One option would be different reaction cross sections for the primary attachment of SiO_2 on the Ag surface and the surface growth on top of a Si layer. This would lead to different growth mechanisms becoming energetically favourable at different stages of coating and cause the initial inhomogeneous growth.

As the setup is capable of very long confinement times, well-defined homogeneous coatings are possible through extending the treatment duration and lowering silane concentrations. Further investigations into changing plasma

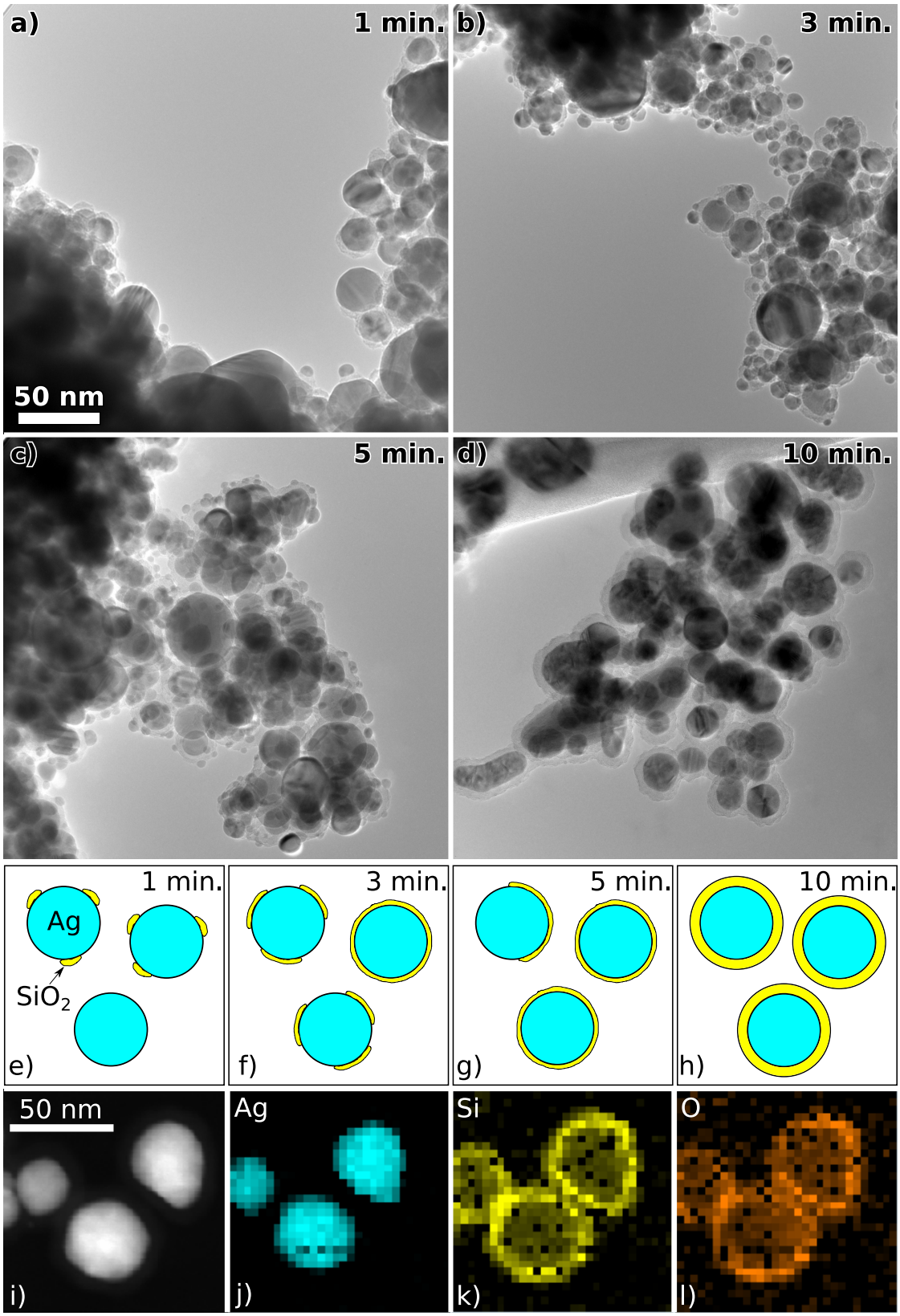

Figure 4.13: High-angle annular dark-field (HAADF) scanning transmission electron microscopy (STEM) micrographs for samples of silver particles coated with SiO_2 for different durations. It can be seen that the particles are not homogeneously coated for 1 to 5 min (a-c). After 10 min the coating is homogeneous (d). The growth process of the SiO_2 coating is shown schematically (e-h). Additionally, EDX maps were recorded for a sample with a coating time of 10 min, which show that particles have an Ag core with an SiO_x shell (i-l). Published in [32].

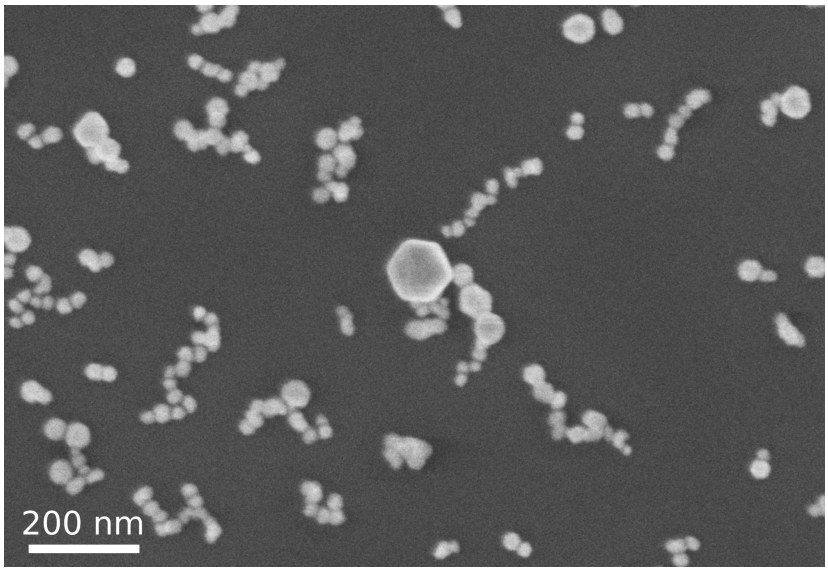

Figure 4.14: SEM image of Ag particles coated for 3 min with silane and extracted onto a silicon wafer. Particles appear to be agglomerated. It is unclear, whether agglomeration happens during the extraction process or already during confinement in the holding plasma. Published in [32].

parameters – the plasma power in particular – seem fruitful, as lower energy densities also can lead to more homogeneous growth. First experiments performed in the course of the master's thesis of Florian Ziegler [41] showed that powers of 40 and 60 W lead to more homogeneous coverings even at short coating durations.

While the particles on the TEM micrographs are agglomerated, it is unclear whether this happened during the confinement in the plasma, during the extraction process, or while scratching off the particles off of the silicon wafer onto TEM grids. Especially the latter procedure is known to create particle agglomerates, yet agglomerates were also seen in SEM images taken before scratching off shown in fig. 4.14. Together with the increasing shoulder towards higher wavelengths in the LSPR measurements this suggests that agglomeration might already occur in the holding plasma. Yet, further investigations are necessary to determine the exact cause. In case agglomeration happens in the holding plasma, reducing the number of injected particles or increasing the plasma density might lead to stronger charged particles, thereby limiting particle collisions and inhibiting agglomeration.

To investigate the effects of plasma exposure, a further sample is taken of the silver particles coated for 90 s with silane and then treated with argon for 1 h that were described in the previous section and shown in fig. 4.12. No significant damage or changes to the particles or coating can be seen comparing the two TEM micrographs shown in fig. 4.15. This shows that the plasma can be used for confinement without inducing further changes to the particles.

Finally, EDX measurements were performed to determine the composition of the coating material. Figures 4.13i to 4.13l shows a STEM HAADF micrograph and corresponding elemental EDX maps. The silver core and surrounding shell

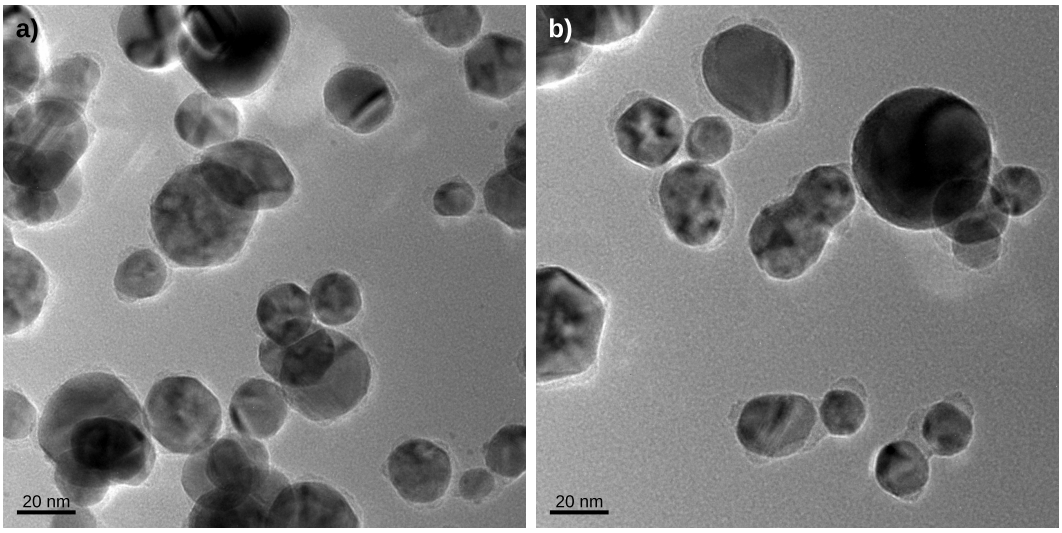

Figure 4.15: TEM images of particles with 90 s of silicon coating using silane. a) Extracted immediately after coating. b) Extracted after an hour of argon plasma treatment after coating. No significant effect of the treatment can be seen. Published in [32].

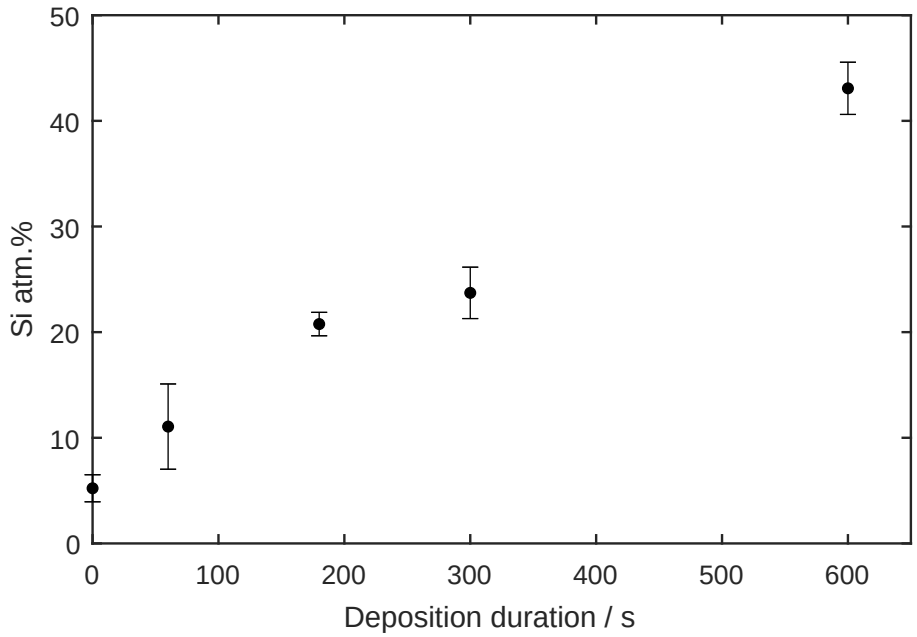

Figure 4.16: Atomic concentration of silicon measured with EDX during TEM imaging for extracted particles with different coating durations. Ten different areas of the TEM grid were used for statistical analysis. Only silver and silicon was taken into account to minimise the influence of further oxidation after extraction as well as the background carbon support of the TEM grid. Published in [32].

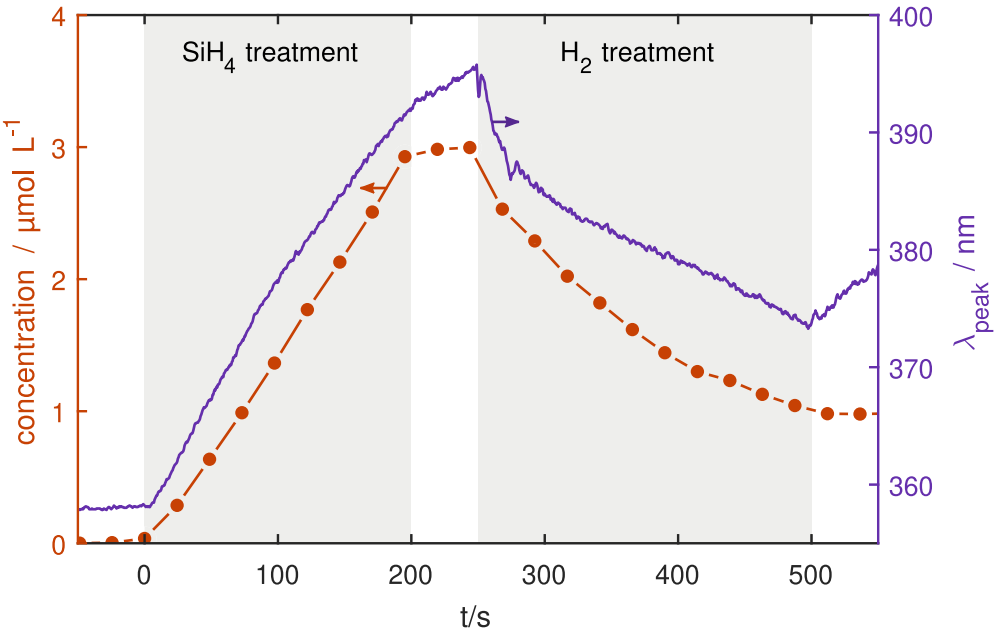

Figure 4.17: Combined coating and etching experiment with SiO_2-coated Ag particles. Particles were injected into the holding plasma, coated for 200 s using silane, and subsequently etched adding H_2 to the Ar plasma (both treatments marked in grey). This procedure was measured both using UV-Vis spectroscopy (main peak position marked on right axis) and infrared spectroscopy (Si−O−Si concentration marked on left axis). Published in [32].

consisting of silicon and oxygen are well visible and no further atoms were found in the EDX signal. The exact stoichiometry of the SiO_x coating could not be determined, as the particles were subjected to ambient air during transport to the TEM and are likely to be fully oxidised. Therefore only atomic concentrations of Ag and Si were determined as shown in fig. 4.16. The concentration of silicon increases stronger between 0 and 3 min of coating in comparison to the period between 3 and 10 min once again in agreement with findings from FTIR described above, where two different growth rates were found.

4.3.4 In situ monitored etching experiment

Finally, as a proof of concept of the versatility of the setup, an etching experiment has been performed where particles are first injected and coated with a SiO_2 layer for 200 s, to then in a second step be etched using an Ar/H_2 plasma. The experiment is performed twice, once monitored using UV-Vis and once using infrared spectroscopy. A significant redshift can be seen in the position of the main LSPR peak during the coating treatment with 20 sccm of SiH_4 (0.01 % in Ar) as described previously. Similarly, the infrared absorption shows a linear increase of Si−O−Si bonds during the coating indicating the linear growth of a SiO_2 coating on the particle surface.

When the silane flow is stopped at $t = 200$ s, the measured concentration via

infrared absorption stays mostly constant, while the LSPR peak shows a continuing redshift albeit at a slower rate than before. It is unclear, why this is the case. One possible explanation would be the H_2-continuous emission background in the region in the range of 160–500 nm. The silane treatment introduces hydrogen to the holding plasma, which is then slowly removed through pumping after the end of treatment. As the analysis only tracks the position of maximal absorption of the LSPR peak, the tail of the H_2-continuum towards longer wavelengths would appear to blueshift the LSPR peak due to the addition of both features. This would lead the peak position to be slightly underestimated during the coating treatment and then slowly return to its actual position after its end, affecting the analysis as an apparent redshift.

At $t = 250\,\mathrm{s}$ hydrogen is added to the holding plasma with a flow of 1 sccm (compared to the $2 \cdot 10^{-3}$ sccm partial flow of silane during coating). This induces strong etching seen in both a strong blueshift of the LSPR peak and a decrease of Si−O−Si concentration in the infrared spectrum. The etching rate as measured by both methods is decreasing in rate over time, likely indicating a shrinking surface area of etchable material.

After turning off the hydrogen flow at $t = 500\,\mathrm{s}$, the Si−O−Si concentration stays constant, while the LSPR peak once again shows a redshift. The redshift is pronounced more strongly here compared to the end of silane treatment. This reinforces the explanation of a decreasing H_2-continuum as the hydrogen amount in the system is much higher during hydrogen treatment, creating a stronger continuum background.

Other possible factors explaining the LSPR redshift are its dependency on various particle properties. Whereas the infrared absorption solely measures the amount of Si−O−Si bonds present in the volume, the LSPR is also influenced by the particle's charge [42] and temperature [43]. A change in gas composition especially with electronegative gasses such as SiH_4 or H_2 can significantly affect the electron density and temperature in the plasma which determines particle charge. Furthermore, it also affects processes such as selective heating through recombination of ions or hydrogen atoms on the particle surface [44]. Additional plasma diagnostics would be necessary to monitor these effects to be able to analyse the LSPR spectrum in further detail through modelling of the particle and its coating.

References

[1]F. M. J. H. van de Wetering, S. Nijdam, and J. Beckers, "Conclusive evidence of abrupt coagulation inside the void during cyclic nanoparticle formation in reactive plasma", Applied Physics Letters **109**, 043105, ISSN: 0003-6951 (2016).

[2]C. Killer, F. Greiner, S. Groth, B. Tadsen, and A. Melzer, "Long-term spatio-temporal evolution of the dust distribution in dusty argon rf plasmas", Plasma Sources Science and Technology **25**, 055004, ISSN: 1361-6595 (2016).

[3]A. Hinz, E. von Wahl, F. Faupel, T. Strunskus, and H. Kersten, "Nanoparticle forming reactive plasmas: a multidiagnostic approach", The European Physical Journal D **72**, 10.1140/epjd/e2017-80372-6 (2018).

[4]S. Groth, F. Greiner, and A. Piel, "Spatio-temporally resolved investigations of layered particle growth in a reactive argon-acetylene plasma", Plasma Sources Science and Technology **28**, 115016, ISSN: 1361-6595 (2019).

[5]N. Rao, P. Shukla, and M. Yu, "Dust-acoustic waves in dusty plasmas", Planetary and Space Science **38**, 543–546 (1990).

[6]A. A. Mamun and P. K. Shukla, "Discoveries of waves in dusty plasmas", Journal of Plasma Physics **77**, 437–455 (2010).

[7]P. Bandyopadhyay and A. Sen, "Driven nonlinear structures in flowing dusty plasmas", Reviews of Modern Plasma Physics **6**, 10.1007/s41614-022-00091-3 (2022).

[8]M. Schulze, D. O'Connell, T. Gans, P. Awakowicz, and A. von Keudell, "Rotation of a nanoparticle cloud in an inductively coupled plasma induced by weak static magnetic fields", Plasma Sources Science and Technology **16**, 774–784 (2007).

[9]B. Tadsen, F. Greiner, and A. Piel, "Probing a dusty magnetized plasma with self-excited dust-density waves", Physical Review E **97**, 033203, ISSN: 2470-0045 (2018).

[10]G. H. P. M. Swinkels, E. Stoffels, W. W. Stoffels, N. Simons, G. M. W. Kroesen, and F. J. de Hoog, "Treatment of dust particles in an RF plasma monitored by Mie scattering rotating compensator ellipsometry", Pure and Applied Chemistry **70**, 1151–1156, ISSN: 1365-3075 (1998).

[11]J. Carstensen, H. Jung, F. Greiner, and A. Piel, "Mass changes of microparticles in a plasma observed by a phase-resolved resonance method", Physics of Plasmas **18**, 033701, ISSN: 1070-664X (2011).

[12]J. Carstensen, F. Haase, H. Jung, B. Tadsen, S. Groth, F. Greiner, and A. Piel, "Probing the Plasma Sheath by the Continuous Mass Loss of Microparticles", IEEE Transactions on Plasma Science **41**, 764–768, ISSN: 0093-3813 (2013).

[13]O. Asnaz, H. Jung, F. Greiner, and A. Piel, "Size and density evolution of a single microparticle embedded in a plasma", Physics of Plasmas **24**, 083701, ISSN: 1070-664X (2017).

[14]S. Groth, F. Greiner, B. Tadsen, and A. Piel, "Kinetic Mie ellipsometry to determine the time-resolved particle growth in nanodusty plasmas", Journal of Physics D: Applied Physics **48**, 465203, ISSN: 0022-3727 (2015).

[15]M. C. Coen, R. Lehmann, P. Groening, and L. Schlapbach, "Modification of the micro- and nanotopography of several polymers by plasma treatments", Applied Surface Science **207**, 276–286, ISSN: 0169-4332 (2003).

[16]B. Tadsen, F. Greiner, and A. Piel, "On the amplitude of dust-density waves in inhomogeneous dusty plasmas", Physics of Plasmas **24**, 033704, ISSN: 1070-664X (2017).

[17]O. Asnaz, N. Kohlmann, H. Folger, F. Greiner, and J. Benedikt, "Growth and treatment of hydrogenated amorphous carbon nanoparticles in a low-pressure plasma", Plasma Processes and Polymers **19**, 2100190 (2022).

[18]J. Ristein, R. T. Stief, L. Ley, and W. Beyer, "A comparative analysis of a-C:H by infrared spectroscopy and mass selected thermal effusion", Journal of Applied Physics **84**, 3836–3847, ISSN: 0021-8979 (1998).

[19]E. Kovačević, J. Berndt, T. Strunskus, and L. Boufendi, "Size dependent characteristics of plasma synthesized carbonaceous nanoparticles", Journal of Applied Physics **112**, 013303, ISSN: 0021-8979 (2012).

[20]T. Schwarz-Selinger, A. von Keudell, and W. Jacob, "Plasma chemical vapor deposition of hydrocarbon films: The influence of hydrocarbon source gas on the film properties", Journal of Applied Physics **86**, 3988–3996, ISSN: 0021-8979 (1999).

[21]B. Tadsen, F. Greiner, S. Groth, and A. Piel, "Self-excited dust-acoustic waves in an electron-depleted nanodusty plasma", Physics of Plasmas **22**, 113701, ISSN: 1070-664X (2015).

[22]J. Benedikt, "Plasma-chemical reactions: low pressure acetylene plasmas", Journal of Physics D: Applied Physics **43**, 043001, ISSN: 0022-3727 (2010).

[23]NIST Mass Spectrometry Data Center and William E. Wallace, director, "Infrared Spectra", in *NIST Chemistry WebBook, NIST Standard Reference Database Number 69*, edited by P. J. Linstrom and W. G. Mallard (2023).

[24]M. Hirasawa, T. Orii, and T. Seto, "Size-dependent crystallization of Si nanoparticles", Applied Physics Letters **88**, 093119, ISSN: 0003-6951 (2006).

[25]H. R. Maurer and H. Kersten, "On the heating of nano- and microparticles in process plasmas", Journal of Physics D: Applied Physics **44**, 174029 (2011).

[26]S. Agarwal, A. Takano, M. C. M. van de Sanden, D. Maroudas, and E. S. Aydil, "Abstraction of atomic hydrogen by atomic deuterium from an amorphous hydrogenated silicon surface", The Journal of Chemical Physics **117**, 10805–10816 (2002).

[27]S. K. Bose, J. B. Mallinson, R. M. Gazoni, and S. A. Brown, "Stable Self-Assembled Atomic-Switch Networks for Neuromorphic Applications", IEEE Transactions on Electron Devices **64**, 5194–5201 (2017).

[28]M. A. Zidan, J. P. Strachan, and W. D. Lu, "The future of electronics based on memristive systems", Nature Electronics **1**, 22–29 (2018).

[29]J.-H. Cha, S. Y. Yang, J. Oh, S. Choi, S. Park, B. C. Jang, W. Ahn, and S.-Y. Choi, "Conductive-bridging random-access memories for emerging neuromorphic computing", Nanoscale **12**, 14339–14368 (2020).

[30]Z. Kuncic and T. Nakayama, "Neuromorphic nanowire networks: principles, progress and future prospects for neuro-inspired information processing", Advances in Physics: X **6**, 10.1080/23746149.2021.1894234 (2021).

[31]N. Carstens, B. Adejube, T. Strunskus, F. Faupel, S. Brown, and A. Vahl, "Brain-like critical dynamics and long-range temporal correlations in percolating networks of silver nanoparticles and functionality preservation after integration of insulating matrix", Nanoscale Advances **4**, 3149–3160 (2022).

[32]O. Asnaz, J. Drewes, M. Elis, T. Strunskus, F. Greiner, O. Polonskyi, F. Faupel, L. Kienle, A. Vahl, and J. Benedikt, "A novel method for the synthesis of core–shell nanoparticles for functional applications based on long-term confinement in a radio frequency plasma", Nanoscale Advances **5**, 1115–1123 (2023).

[33]S. J. Oldenburg, "Light scattering from gold nanoshells.", PhD thesis (Rice Univ., Houston, TX, USA, 2000), p. 98.

[34]J. Drewes, S. Ali-Ogly, T. Strunskus, O. Polonskyi, H. Biederman, F. Faupel, and A. Vahl, "Impact of argon flow and pressure on the trapping behavior of nanoparticles inside a gas aggregation source", Plasma Processes and Polymers **19**, 2100125 (2021).

[35]N. G. Bastús, J. Piella, and V. Puntes, "Quantifying the Sensitivity of Multipolar (Dipolar, Quadrupolar, and Octapolar) Surface Plasmon Resonances in Silver Nanoparticles: The Effect of Size, Composition, and Surface Coating", Langmuir **32**, 290–300, ISSN: 1520-5827 (2015).

[36]H. Shen, G. Lu, T. Zhang, J. Liu, Y. Gu, P. Perriat, M. Martini, O. Tillement, and Q. Gong, "Shape effect on a single-nanoparticle-based plasmonic nanosensor", Nanotechnology **24**, 285502, ISSN: 0957-4484 (2013).

[37]D. D. Evanoff, R. L. White, and G. Chumanov, "Measuring the Distance Dependence of the Local Electromagnetic Field from Silver Nanoparticles", The Journal of Physical Chemistry B **108**, 1522–1524, ISSN: 1520-6106 (2004).

[38]C. B. Fleddermann, J. H. Beberman, and J. T. Verdeyen, "Measurement of the electron density and the attachment rate coefficient in silane/helium discharges", Journal of Applied Physics **58**, 1344–1348 (1985).

[39]A. Fidalgo and L. M. Ilharco, "The defect structure of sol-gel-derived silica / polytetrahydrofuran hybrid films by FTIR", Journal of Non-Crystalline Solids **283**, 144–154, ISSN: 0022-3093 (2001).

[40]C. T. Kirk, "Quantitative analysis of the effect of disorder-induced mode coupling on infrared absorption in silica", Physical Review B **38**, 1255–1273 (1988).

[41]F. Ziegler, "In-Flight Trapping of Metal Nanoparticles and Formation of Core-Shell Nanoparticles", MA thesis (Kiel University, 2022).

[42]M. Zapata Herrera, J. Aizpurua, A. K. Kazansky, and A. G. Borisov, "Plasmon Response and Electron Dynamics in Charged Metallic Nanoparticles", Langmuir **32**, 2829–2840, ISSN: 1520-5827 (2016).

[43]O. A. Yeshchenko, I. M. Dmitruk, A. A. Alexeenko, A. V. Kotko, J. Verdal, and A. O. Pinchuk, "Size and Temperature Effects on the Surface Plasmon Resonance in Silver Nanoparticles", Plasmonics **7**, 685–694, ISSN: 1557-1955 (2012).

[44]L. Mangolini and U. Kortshagen, "Selective nanoparticle heating: Another form of nonequilibrium in dusty plasmas", Physical Review E **79**, 026405, ISSN: 1539-3755 (2009).

5

Summary and conclusions

This work has presented various methods of using plasma systems to synthesise, confine, and manipulate nanoparticles with precise control and continuous monitoring with in situ diagnostics using Fourier-transform infrared spectroscopy (FTIR) and localised surface plasmon resonance (LSPR). In contrast to classic in-flight treatments [1–3], where particles are slowed down to achieve residence times in the order of seconds, it was demonstrated how using a secondary plasma enables confinement durations of up to an hour without any significant losses of nanoparticles. These time scales allow for a precisely controlled treatment of the particles, which makes it possible to create specifically tailored nanoparticles in complex processes.

First, the Suleika Nano plasma system typically used in dusty plasma experiments was investigated to determine the cause of changes to the particle mass during confinement. The amorphous hydrogenated carbon (a-C:H) particles with diameters of around 500 nm were found to exhibit a growth in size in the used configuration without the addition of any reactive gasses. This was traced back to small leaks in the system, which is only capable of fine to high vacuum conditions. Under argon plasma treatment, traces of oxygen were incorporated into the material, leading to the observed size increase. Admixing oxygen in high amounts lead to the expected etching of the particles instead. Experiments with hydrogen and deuterium showed only etching processes without chemical changes to the material.

Furthermore, amorphous hydrogenated silicon (a-Si:H) nanoparticles were synthesised in an external capacitively coupled plasma (CCP) source with a secondary plasma for confinement and treatment. Contrary to the experiments with carbon nanoparticles, hydrogen treatment of silicon nanoparticles has shown addition and substitution reactions to occur. This was shown via the use of deuterium as a tracer. An investigation using FTIR has shown incorporation of deuterium into both surface and bulk material. While deuterium mainly attached to existing bonds in the bulk material, a substitution of hydrogen for deuterium was seen on the surface.

Finally, in collaboration with the Chair for Multicomponent Materials of Prof. Faupel at the Faculty of Engineering, a combined setup of a Haberland-type gas aggregation source (GAS) with our secondary treatment plasma was used to generate silver-silica core-shell nanoparticles. The produced nanoparticles showed a homogeneous shell with a thickness of up to 6 nm, which is beyond the

capabilities of typical in-flight treatment setups. These core-shell nanoparticles show very promising properties for applications in neuromorphic computing [4–8]. Furthermore, as a proof of principle of multi-step processes a silver nanoparticle was first coated with silica to then etch part of the coating by admixing hydrogen. This demonstrated the wide range of possibilities for fabricating nanoparticles with several shell layers, surface functionalisations, or even gradual changes in composition.

Conclusions

The combination of a GAS and a secondary treatment plasma discharge opens the door for the fabrication of specifically tailored nanoparticles with complex composition.

The separation of particle synthesis and particle treatment into two separate systems allows for very flexible fabrication processes. This was demonstrated in the combination of a GAS for the generation of metal nanoparticles and a secondary inductively coupled plasma (ICP) discharge operated in E-mode for subsequent treatment. Acting as a proof of concept, Ag@SiO_2 core-shell nanoparticles were generated with shell thicknesses of up to 6 nm beyond the capabilities of in-flight treatment setups. As an outlook, an etching experiment was performed demonstrating of the possibilities of multi-step processes. Particles with multiple shells or even gradual changes in shell composition by changing the reactive gasses during the coating treatment are achievable as a result of this work.

In situ FTIR allows precise monitoring of treatment processes of nanoparticles.

FTIR was used to monitor the plasma treatment process. The concentration of specific chemical bonds was measured with a time resolution of one measurement every 6–30 s. For silicon nanoparticles, distinguishing between surface and bulk bonds was possible and gave insight into the reaction pathways of hydrogen with carbon and silicon nanoparticles.

FTIR and LSPR are complementary in situ diagnostics for monitoring the treatment of metallic nanoparticles.

Pure silver does not absorb infrared radiation and most silver compounds absorb in the far-infrared region below 600 cm^{-1} inaccessible to our setup. This makes the LSPR a strong tool for detecting small changes on the particle surface. It is particularly sensitive for the immediate surrounding of the plasmonically active silver core and can detect the initial changes during a coating treatment. For thicker coatings of tens of nanometres, infrared spectroscopy becomes advantageous as the plasmonic excitation cannot penetrate deeper in to the coating.

The mass changes of a-C:H micro- and nanoparticles in typical dusty plasma experiments can be traced back to oxygen impurities.

The Suleika Nano chamber, as a prototypical dusty plasma experiment setup, is only capable of reaching a final pressure of 10^{-1} Pa in the fine to high vacuum regime due to small leaks of ambient air. This oxygen from ambient air was determined as the key reactive species leading to an increase in particle size for the investigated parameters. Addition of hydrogen captures free oxygen in the system and inhibits attachment, but in turn leads to etching of the particles.

The treatment of a-C:H nanoparticles with hydrogen is solely an etching reaction without substitution.

Experiments comparing hydrogen and deuterium treatment both showed a decrease in particle size. Infrared spectroscopy of the deuterium treatment only showed an overall decrease in CH_x bonds without the creation of new CD bonds at any point. This indicates that the hydrogen treatment solely leads to etching of the particle material without the addition of hydrogen into its structure.

The treatment of a-Si:H nanoparticles with hydrogen shows addition in the bulk material and substitution on the surface.

Similar experiments performed for silicon nanoparticles showed an incorporation of deuterium into the particle material. The bulk material showed the addition of deuterium into the existing bonds, e.g. leading from SiH_2 to the formation of SiH_2D. On the surface, deuterium replaced existing hydrogen bonds instead lowering the overall hydrogen content. Preferential formation of the 2-bonded deuterides SiHD and SiD_2 was seen.

The operation of an ICP discharge in H-mode creates conditions that disintegrate nanoparticles.

Experiments performed both with silver and with silicon nanoparticles showed that no absorption signal was seen when switching the ICP discharge into H-mode. For silver particles, optical emission lines from atomic silver were seen. It is likely that the thermal conditions created by the increased plasma density lead to the disintegration of the nanoparticles.

The implementation of a stainless steel cage around the plasma volume improves the confinement properties.

To improve the confinement of nanoparticles, the plasma volume was surrounded by a stainless steel cage. This increased the electric fields responsible for particle confinement and improved the slow down of injected nanoparticles. Later experiments showed that without the implementation of the cage, about 20 % of particles are lost over 30 min of confinement.

References

[1]J. Bai and J.-P. Wang, "High-magnetic-moment core-shell-type FeCo–Au/Ag nanoparticles", Applied Physics Letters **87**, 152502 (2005).

[2]J. Hanuš, M. Vaidulych, O. Kylián, A. Choukourov, J. Kousal, I. Khalakhan, M. Cieslar, P. Solař, and H. Biederman, "Fabrication of Ni@Ti core–shell nanoparticles by modified gas aggregation source", Journal of Physics D: Applied Physics **50**, 475307 (2017).

[3]T. Kretková, J. Hanuš, O. Kylián, P. Solař, M. Dopita, M. Cieslar, I. Khalakhan, A. Choukourov, and H. Biederman, "In-flight modification of Ni nanoparticles by tubular magnetron sputtering", Journal of Physics D: Applied Physics **52**, 205302 (2019).

[4]S. K. Bose, J. B. Mallinson, R. M. Gazoni, and S. A. Brown, "Stable Self-Assembled Atomic-Switch Networks for Neuromorphic Applications", IEEE Transactions on Electron Devices **64**, 5194–5201 (2017).

[5]M. A. Zidan, J. P. Strachan, and W. D. Lu, "The future of electronics based on memristive systems", Nature Electronics **1**, 22–29 (2018).

[6]J.-H. Cha, S. Y. Yang, J. Oh, S. Choi, S. Park, B. C. Jang, W. Ahn, and S.-Y. Choi, "Conductive-bridging random-access memories for emerging neuromorphic computing", Nanoscale **12**, 14339–14368 (2020).

[7]Z. Kuncic and T. Nakayama, "Neuromorphic nanowire networks: principles, progress and future prospects for neuro-inspired information processing", Advances in Physics: X **6**, 10.1080/23746149.2021.1894234 (2021).

[8]N. Carstens, B. Adejube, T. Strunskus, F. Faupel, S. Brown, and A. Vahl, "Brain-like critical dynamics and long-range temporal correlations in percolating networks of silver nanoparticles and functionality preservation after integration of insulating matrix", Nanoscale Advances **4**, 3149–3160 (2022).

A

List of own publications

The publications are presented in chronological order. Equally contributing first authors are indicated with an asterisk.

Parts of this thesis published in peer-reviewed journals

[1] **O. Asnaz**, N. Kohlmann, H. Folger, F. Greiner, and J. Benedikt, "Growth and treatment of hydrogenated amorphous carbon nanoparticles in a low-pressure plasma", Plasma Processes and Polymers **19**, 2100190 (2022).

[2] **O. Asnaz***, J. Drewes*, M. Elis, T. Strunskus, F. Greiner, O. Polonskyi, F. Faupel, L. Kienle, A. Vahl, and J. Benedikt, "A novel method for the synthesis of core–shell nanoparticles for functional applications based on long-term confinement in a radio frequency plasma", Nanoscale Advances **5**, 1115–1123 (2023).

Further publications in peer-reviewed journals

[3] H. Jung, F. Greiner, **O. Asnaz**, J. Carstensen, and A. Piel, "Exploring the wake of a dust particle by a continuously approaching test grain", Physics of Plasmas **22**, 10.1063/1.4920968, ISSN: 1089-7674 (2015).

[4] H. Jung, F. Greiner, **O. Asnaz**, J. Carstensen, and A. Piel, "Resonance methods for the characterization of dust particles in plasmas", Journal of Plasma Physics **82**, 1–14, ISSN: 1469-7807 (2016).

[5] **O. Asnaz**, H. Jung, F. Greiner, and A. Piel, "Size and density evolution of a single microparticle embedded in a plasma", Physics of Plasmas **24**, 083701, ISSN: 1070-664X (2017).

[6] **O. Asnaz**, H. Jung, F. Greiner, and A. Piel, "Charging of an irregularly shaped particle in the sheath of an rf plasma", Physics of Plasmas **25**, 10.1063/1.5038183, ISSN: 1089-7674 (2018).

[7] N. Kohlmann, F. Wieben, **O. Asnaz**, D. Block, and F. Greiner, "High-precision in-situ size measurements of single microparticles in an RF plasma", Physics of Plasmas **26**, 053701, ISSN: 1070-664X (2019).

[8] M. Dworschak, **O. Asnaz**, and F. Greiner, "A minimally invasive electrostatic particle extractor for nanodusty plasmas and its application for the verification of in situ Mie polarimetry", Plasma Sources Science and Technology **30**, 035011, ISSN: 0963-0252 (2021).

[9]A. Petersen, **O. Asnaz**, B. Tadsen, and F. Greiner, "Decoupling of dust cloud and embedding plasma for high electron depletion in nanodusty plasmas", Communications On Physics **5**, 308, ISSN: 2399-3650 (2022).

B

Assorted bits of know-how

"It's dangerous to go alone! Take this."
(Unnamed old man in The Legend of Zelda)

This section contains the bits and pieces of knowledge gathered over four years of work. It is mainly aimed to help the poor soul who will continue working on this monstrous machinery of ambition and despair that keeps growing two new ~~heads~~ Swagelok valves for each one you chop down.

Terminology

In FTIR spectroscopy, the mirror velocity is often given not in $\mathrm{cm\,s^{-1}}$ but rather kHz. This stems from the fact that the mirror speed is measured by sending a secondary laser beam through the two-beam interferometer and measuring the mirror travel by the sequence of constructive and destructive interference of the beam, measured in kHz.

In the literature, the term *deconvolution* is often found for describing the process of splitting the absorption curve into its constituting absorption peaks. One pit fall is the fact, that the corresponding verb is not *deconvolute* but rather *deconvolve* similar to revolution–revolve. The second and greater problem is that this is a misleading term and has nothing to do with the mathematical operation of a convolution. In my publications, I have therefore preferred the term *decomposition*, which more clearly and correctly describes the process.

Calibration

The red laser light that is visible as path of the infrared beam comes from an internal laser that is decoupled at a beam splitter after passing the Michelson interferometer. It measures the mirror speed by counting the number of passed intensity maxima of the monochromatic red beam and is measured using a 4-field detector for auto-correcting the beam path. The position of the red light in relationship to the infrared beam *is not constant* and moves whenever the FTIR automatically adjusts its focusing.

Do only use the red spot for coarse calibrations and then go over to the more tedious but precise calibration using the infrared beam itself, measuring it with

an infrared camera. If necessary, enter `LSR=0` into the direct command interface of the FTIR (accessible via the Internet Explorer / web interface of the FTIR) to turn off the red laser. Turn the laser back on using `LSR=1`. Make sure the long wave pass filter is not in, i.e. the filter option is set to "open", as the infrared camera can only measure in the near-infrared region. Setting the aperture to large diameters can help locate the beam with the camera, but shows significant divergence when looking at the focus point with the focal point increasing from a small spot of a few millimetres at an aperture of 0.25 mm to a large spot of about 2 cm diameter with an aperture of 1.5 mm.

OPUS Software

You need to know that the OPUS software has some annoying bugs. When loading settings, check:

- Sample and Reference: Right Exit
- Mirror Velocity: 200 kHz
- Opt. Filter: Filter 4
- Aperture: 1.5 mm
- Detector: LN-MCT (Default address)

When you start a measurement, these can actually be reset to what was set previously, even if you have explicitly reset them before the measurement. If they do, reselect all of these settings again and again until your amplitude is at what you expect (20 passes: ≈ 430).

NIST Database

Make sure to have a look at the original spectrum file for infrared spectra. Sometimes there are hand-written notes on the actual piece of paper the data was recorded on.

Silane laboratory

The sensors in the silane lab to detect leaks of silane can be tripped by methane as well, as the sensors have cross-sensibility. Opening the windows to create a draught is enough to prevent an alarm while changing methane bottles on the experiment.

C

Danksagung

An dieser Stelle möchte ich allen Menschen danken, die mich auf dieser langen Reise begleiteten und ohne die diese Arbeit nicht möglich gewesen wäre.

Ich danke natürlich Prof. Jan Benedikt, der mich quasi mit dem Kieler Inventar übernahm und mir als sein erster Kieler Doktorand diese Stelle anbot. Ich konnte mich jederzeit an ihn wenden und er hielt mir den Rücken frei sowohl in Themen der Bezahlung als auch in Fragen der Physik. Es war eine spannende und bereichernde Aufgabe, gemeinsam das Labor zu gestalten und den Aufbau auf die Beine zu stellen, um die Messungen dieser Arbeit durchzuführen.

Besonderer Dank gilt auch Dr. Jonas Drewes, meinem Mitstreiter vom gegenüberliegenden Teil der Förde. Es zeigte sich, dass, wenn man in den vorherigen Jahren alle Optionen für Misserfolg bereits durchexerziert hat, nichts mehr übrig bleibt, was schief gehen kann. Das Zusammenbringen beider Hälften des Projektes war eine der produktivsten und erfolgreichsten Phasen meiner ganzen Promotion und es hat großen Spaß bereitet, gemeinsam mit dir diese Arbeit zu bewältigen.

Weiterhin möchte ich mich bei Dr. Hendrik Jung und Prof. Judith Golda bedanken, die mir gerade zu Beginn der Promotion sowohl mit ihrer Erfahrung stets zur Seite standen als auch bei geselligen Abenden immer eine entspannte Atmosphäre schafften.

Dazu gehören natürlich auch all die anderen Doktoranden, die im Laufe der Jahre dazustießen. Kerstin Sgonina, die als Mitstreiterin der ersten Generation alle Höhen und Tiefen der Zeit mitgemacht hat. Ich danke dir für die vielen Gespräche über die Physik und die Welt und wünsche dir viel Erfolg bei deinem eigenen Endspurt.

Christian Schulze als weiterer Vertreter der alten Garde, mit dem ich gemeinsam hoffentlich bei den Projekttagen Physik und Technik einer Gruppe Schülerinnen die Freude der Fotographie nahebringen konnte. Ich danke auch Sören Wohlfahrt, dessen Arbeit als geistige Fortführung meiner Masterarbeit immer eine besondere Stelle in meinem Herzen hatte und dessen liebenswerte und humorvolle Art immer eine Bereicherung des Alltags war. Und nicht zu vergessen Andreas Petersen, dem einzigen Doktoranden neben mir, der ebenfalls inzwischen eine Inventarnummer verdient hätte.

Auch den späteren Doktoranden Tristan Winzer, Maren Dworschak, He Li, Armin Mengel und Natascha Blosczyk danke ich für die angenehme Zeit und

für die Doktorandenabende bei netter Gesellschaft und leckerem Essen. Transzendiert aus der Reihe niederer Doktoranden, danke ich auch unserem Post-doc Dr. Luka Hansen für die Unterstützung durch seine frischen Erfahrungen zum Promotionsverfahren und hilfreichen Tipps zum Schreiben dieser Arbeit.

Ich danke auch Dr. Franko Greiner für die gemeinsame Arbeit zu Beginn und die Unterstützung in der zweiten Hälfte meiner Promotion. Auf deine direkten und zielsicheren Ratschläge war immer Verlass.

Nicht vergessen sei die technische Unterstützung von Volker Rohwer, Frank Brach und Michael Poser. Ihr wart immer zur Stelle, wenn es Bedarf gab und ohne eure tatkräftige Unterstützung wäre im Labor heute nichts außer leises Grillenzirpen zu hören. Auch danke ich Stephanie Thiedemann für stete Hilfe bei bürokratischen Angelegenheiten aller Art.

Ganz besonders möchte ich meinen Eltern Ümit und Bahar Asnaz danken, die während des gesamten Studiums stärkend hinter mir standen und mich jederzeit unterstützten. Meiner Partnerin Simone Sonderegger danke ich für deine Offenheit, die mir die Ruhe und Sicherheit gibt, jeden Tag auf's Neue zu genießen.

Für das Korrekturlesen meiner unglücklichen Formulierungen bedanke ich mich sowohl bei meinen Freunden Anton Dorn und Ian Thorpe, als auch allen anderen bereits oben erwähnten Personen, die verschiedene Scheibchen dieser Arbeit zum Gegenlesen bekamen.

Abschließend möchte ich mich bei allen derzeitigen und auch allen ehemaligen Mitgliedern der Arbeitsgruppe bedanken für eine angenehme Arbeitsatmosphäre und zahlreichen Kaffeepausen, skalierend in Absurdität je nach aktuellem Wochentag. Es war eine wunderbare Zeit, an die ich stets mit großer Freude zurückdenken werde.